



Leibniz-Institut im Forschungsverbund Berlin e.V.

AnnualReport 2023

Table of Contents

Scientific Advisory Board	5
--	---

Highlights

Towards more efficient organic solar cells: a detailed study of loss pathway and its impact on overall device performance in low-offset organic solar cells	7
Strain states and plastic relaxation of α -(Al,Ga) ₂ O ₃ thin films on a-plane Al ₂ O ₃	11
GaN/ScN core/shell nanowires: A new platform for the epitaxy of twin-free transition metal nitrides	16

Brief Reports

I Nanofabrication

Phase-selective growth of κ - and β -Ga ₂ O ₃ by In-mediated metal exchange catalysis in plasma-assisted molecular beam epitaxy	21
In-situ etching of elemental layers in oxide MBE by O ₂ -assisted formation and evaporation of their volatile suboxide.....	25
Optical properties of ScN layers grown on Al ₂ O ₃ (0001) by plasma-assisted molecular beam epitaxy	29
Large-area epitaxial growth and characterization of 2D Fe _{5-x} GeTe ₂ /WSe ₂ ferromagnet/semiconductor van der Waals heterostructures	33
Optical phonon modes in LaInO ₃ : Lattice dynamics and complete polarization analysis of Raman-active modes	37

II Nanoanalytics

Depth-resolved and large area analysis of dislocation filter layer properties by STEM.....	41
Three-dimensional reconstruction of interface alloy disorder in Ge/GeSi asymmetrically coupled quantum wells using electron tomography	45
Atomic structures and interfacial engineering of ultrathin indium intercalated between graphene and SiC substrate	49
Creating quantum dots on the InAs(110) cleavage surface by atom manipulation.....	53
Excitonic and deep-level emission from N- and Al-polar homoepitaxial AlN layers grown by molecular beam epitaxy	57

III III-V Nanowires for Optoelectronics

Top-down (In,Ga)N nanowires fabricated from molecular beam epitaxial layers with high structural perfection	61
Diameter dependence of light absorption enhancement in GaAs nanowires evidenced by photoluminescence spectroscopy	65
Cathodoluminescence spectroscopy revealing the interplay of structural and point defects in GaN nanowires grown by molecular beam epitaxy	69

IV Control of Elementary Excitations by Acoustic Fields

Microcavity phonoritons – a coherent optical-to-microwave interface	73
Imaging acoustic fields on surfaces and metasurfaces.....	77
Quantification of magnetoacoustic waves in epitaxial Fe ₃ Si/GaAs hybrid structures	82

V Intersubband Emitters: GaAs-based Quantum Cascade Lasers

Towards terahertz quantum-cascade lasers with increased practical operating temperature..... 86

Facts and Figures..... 91

Scientific Advisory Board of Paul-Drude-Institute 2023

<p>Prof. Dr. Manfred Bayer Fakultät Physik Experimentelle Physik 2 Technische Universität Dortmund Deutschland 2016–2019 2020-2023</p>	<p>Dr. Martin Behringer OSRAM Opto Semiconductors GmbH OS CTO TLED R Regensburg Deutschland 2018–2021 2022–2025</p>
<p>Prof. Dr. Oscar Dubon University of California Berkeley, California U.S.A. 2017–2020 2021–2024</p>	<p>Prof. Nicolas Grandjean Ecole Polytechnique Federale de Lausanne EPFL SB IPHYS LASPE Switzerland 2018–2021 2022–2025</p>
<p>Dr. Michelle Johannes Center for Computational Materials Science Naval Research Laboratory Washington DC U.S.A. 2018–2021 2022–2025</p>	<p>Prof. Dr. Dagmar Gerthsen Karlsruher Institut für Technologie (KIT) Karlsruhe, Deutschland 2020-2023</p>
<p>Dr. Heike Riel IBM Research – Zurich Rüschlikon Schweiz 2017–2020 2021-2024</p>	<p>Prof. Dr. Werner Wegscheider Advanced Semiconductor Quantum Materials Laboratory for Solid State Physics ETH Zürich Schweiz 2017–2020 2021-2024</p>
<p>Prof. Dr. Ursula Wurstbauer Institut für Physik Westfälische Wilhelms Universität Münster Münster, Deutschland 2023 - 2026</p>	<p>Dr. Elke Arenholz Pacific Northwest National Laboratory, Richland, WA, USA 2023 - 2026</p>

Highlights

Strain states and plastic relaxation of α -(Al,Ga)₂O₃ thin films on a-plane Al₂O₃

A. Reis, M. Hanke, J.M.J. Lopes, A. Trampert

Ga₂O₃ in its thermodynamically stable monoclinic β -phase has attracted large scientific but also applicational interest due to its ultra-wide bandgap of 4.6 eV, optical transparency and potential to achieve n-type conductivity via extrinsic and intrinsic doping. However, lately also the further meta-stable modifications of Ga₂O₃ have come into focus. Among them the rhombohedral/trigonal α -phase has the largest bandgap of 5.3 eV. Furthermore α -Ga₂O₃ has been shown to exhibit n-type conductivity when Si or Sn are utilized as dopants. As α -Ga₂O₃ is isostructural to sapphire the α -(Al_xGa_{1-x})₂O₃ alloy can be epitaxially grown in the full compositional range on commercially available and cost-effective sapphire allowing for bandgap-engineering between 5.3 and 8.8 eV. The α -(Al_xGa_{1-x})₂O₃/Al₂O₃ heterojunction is suitable for a variety of devices and some of them have already been demonstrated. Among them are laser waveguides, highly rectifying Schottky barrier diodes and MOSFETs. Moreover the application as a barrier layer within (In,Ga)₂O₃/Ga₂O₃ heterostructures has been discussed. Rhombohedral α -(Al_xGa_{1-x})₂O₃ thin films can be deposited on any Al₂O₃ substrate orientation depending on the growth conditions. However it has been shown that binary α -Ga₂O₃ can be stabilized more effectively on the a-plane than on the frequently used c-plane presumably due to the specific arrangement of surface atoms.

In order to effectively design heterostructure devices detailed knowledge about strain states and mechanisms of plastic relaxation are of fundamental interest. Herein we investigate thin (11 – 14 nm) Ga₂O₃ and α -(Al_xGa_{1-x})₂O₃ films with $x = 0.29$ and 0.54 grown on a-plane Al₂O₃ (i.e., (11.0)-oriented) via plasma-assisted molecular beam epitaxy. [A.Reis *et al.*, Appl. Phys. Lett. (accepted, 2023)] Fig. 1(a) shows a schematic representation of the hexagonal unit cell in [11.0] orientation. The epitaxial a-plane is colored in grey and exhibits a two-fold symmetry with both [00.1] and [$\bar{1}$ 1.0] directions in-plane separated by an azimuthal angle of 90°. In addition basal c-, prismatic m- and pyramidal r-planes are depicted in green, cyan and blue. High-resolution X-ray diffraction measurements of the asymmetric (22.6) and (14.0) as well as symmetric (11.0) reflections were performed by use of a PANalytical X'pert PRO MRD laboratory diffractometer. Fig. 1(b) shows a stereographic projection. Since (22.6) lies in the same zone as (11.0) and (00.1), whereas (14.0) is situated within the same zone as (11.0) and ($\bar{1}$ 1.0) thereby information on lattice plane distances and strain states along three orthogonal crystal directions can be derived.

The resulting reciprocal space maps (RSMs) for different Al concentrations x are shown in Fig. 1(c), featuring a more intense and sharp peak originating from the substrate (S) and a less intense one from the epitaxial layer (L). The black arrow points

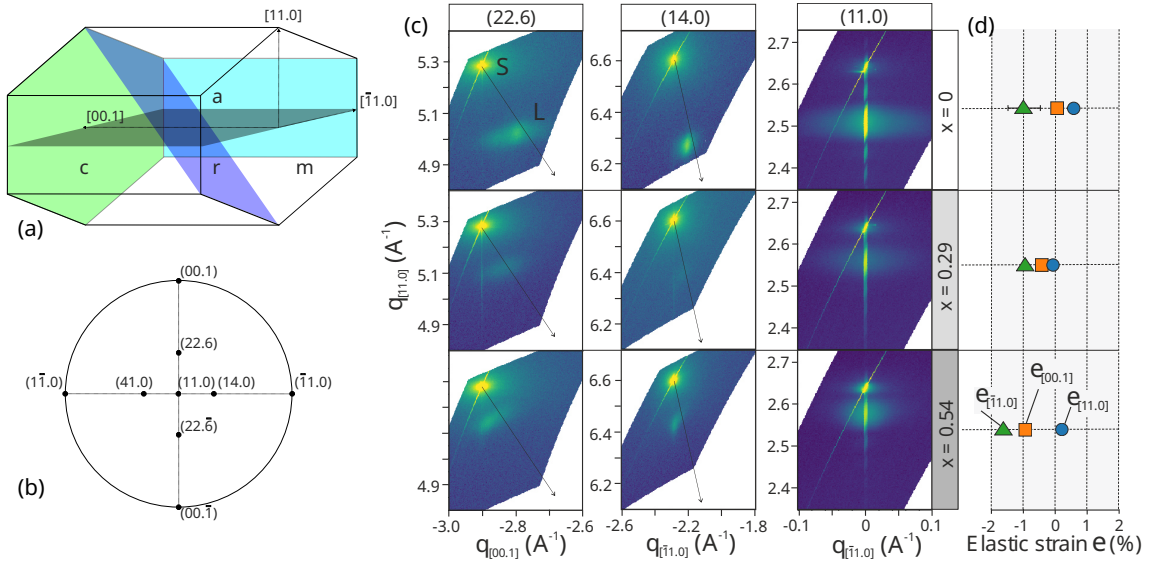


Fig. 1. (a) Schematic representation of the hexagonal unit cell in $[11.0]$ orientation. The epitaxial a plane is depicted in gray. Further crystallographic planes c, m and r are shown in green, cyan and blue. (b) Stereographic projection onto the a plane featuring (22.6) and (14.0) lattice planes separated by an azimuthal angle of 90° . (c) Reciprocal space maps of the asymmetric (22.6) and (14.0) reflections and symmetric (11.0) reflection of $\alpha\text{-}(\text{Al}_x\text{Ga}_{1-x})_2\text{O}_3$ thin films for different Al concentrations x containing substrate (S) and layer peak (L). The black arrow points towards the origin. (d) Elastic strains along 3 orthogonal crystal directions as derived from peak positions within the reciprocal space maps. In-plane compressive strain tends to build up rather across $[\bar{1}1.0]$ than along $[00.1]$.

towards the reciprocal origin of the coordinate system. Due to the small thickness of the epi-layer the resulting peak is comparatively broad and very weak ($I \sim 1$ cps) even though the thickness oscillations as visible in the (11.0) symmetric scan reveal a decent crystal quality. The peak position was determined by fit of a 2D Gaussian and the elastic strain was calculated from the equilibrium lattice constants as determined by Vegard's law. The resulting strains in two in-plane and out-of-plane directions are plotted in Fig. 1(d). As the $\alpha\text{-Ga}_2\text{O}_3$ unit cell is larger than the one of Al_2O_3 the epitaxial layer grows under in-plane compressive strain, which however shows to be unequally distributed among the two in-plane orthogonal directions. Binary Ga_2O_3 is fully relaxed along $[00.1]$, whereas for $x = 0.29$ and 0.54 the epitaxial layer grows partially pseudomorphic due to the reduced lattice mismatch. Across the $[\bar{1}1.0]$ direction the layers behave differently. In case of Ga_2O_3 the lattice is partially strained and for $x = 0.54$ it is even fully pseudomorphic (lattice mismatch is -1.6%). Hence elastic strain is systematically rather accumulated along $[\bar{1}1.0]$ than across $[00.1]$. In $[11.0]$ out-of-plane direction we observe tensile strain as the lattice responds by vertical expansion due to the Poisson effect.

Both asymmetric reflections were also probed in the complementary azimuth, rotated by 180° , i.e. (41.0) and $(22.\bar{6})$ though the resulting RSMs are not shown here. The measured q values deviate by less than 0.01 \AA^{-1} , which is smaller than the experimental error. Thus there is no indication for the presence of lattice tilt. As far as

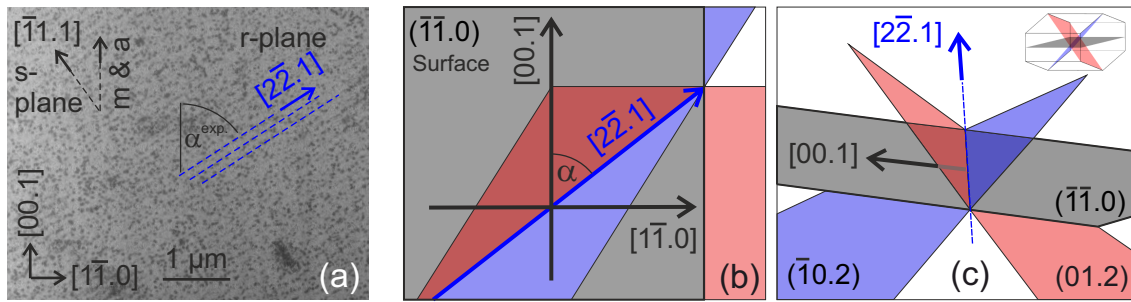


Fig. 2. (a) Scanning electron microscopy image of a 14 nm thick α -($\text{Al}_{0.54}\text{Ga}_{0.46}$) $_2\text{O}_3$ layer on a-plane Al_2O_3 . The surface morphology features equally spaced and oriented hills and valleys, which have been identified as a crosshatch pattern. The measured crossing angle towards the $[00.1]$ axis is $\alpha = 53^\circ$. The pattern is attributed to dislocation glide on the pyramidal r slip system. The relevant (01.2) and $(\bar{1}0.2)$ planes are shown in top view (b) and side view (c) with respect to the epitaxial plane. Both glide planes intersect the surface in the very same vector $[2\bar{2}.1]$, which cuts $[00.1]$ in an angle of $\alpha = 52.0^\circ$.

pseudomorphic layers are concerned this is consistent with strain theory of rhombohedral heterostructures. In a- and c-orientation all strain components are identical to the ones of higher symmetric hexagonal heterostructures, which also implies that the three shear strain components are zero. This is different for heteroepitaxial growth on the rhombohedral m- and r-planes [M. Grundmann, JAP **124**, 185302 (2018)].

Strain emerging at heteroepitaxial interfaces results in the formation of misfit and threading dislocations. Threading dislocations can move through the crystal allowing for further strain relaxation by plastic deformation. As described by Schmid's law the movement requires the activation of a slip system consisting of a set of glide planes and directions. When stress is applied in alumina along $[00.1]$ the activation of pyramidal slip is observed. Within the trigonal system (as opposed to the hexagonal one) there are two families of pyramidal planes being invariant to a $2\pi/3$ rotation, whereas one family of planes will be transformed into the other by rotation about $\pi/3$. Specifically those are the r- and r'-planes [i.e., $\{01.2\}$ and $\{10.2\}$], respectively the s- and s'-planes $\{10.1\}$ and $\{01.1\}$. Among those only the r- and s-families act as glide and cleaving planes while r' and s' do not.

Experimental evidence of the prevailing relaxation mechanism can be provided by surface morphology. In Fig. 2(a) a scanning electron microscopy (SEM) picture of a 14 nm thick $(\text{Al}_x\text{Ga}_{1-x})_2\text{O}_3$ layer with $x = 0.54$ is shown. The image features regularly spaced and equally oriented hills and valleys, which have been identified as a crosshatch pattern. Hence plastic relaxation is a result of dislocation glide, which implies that the terraces emerge at the intersection of the glide planes with the surface and are parallel to the dislocation lines within the crystal. The crossing angle α of the surface steps towards the $[00.1]$ axis was determined with help of a graphics program to 53° .

The crosshatch pattern is to be attributed to the pyramidal r-glide system, which is schematically depicted in Fig. 2(b) and (c) in top and side view on the epitaxial a-plane

drawn in gray. The (01.2) and ($\bar{1}0.2$) glide planes are shown in red and blue whereas the third ($1\bar{1}.2$) plane is not drawn because it is orthogonal to the surface and thus the resolved shear stress is zero. Both the (01.2) and ($\bar{1}0.2$) plane intersect the epitaxial plane in the very same vector, which is $[2\bar{2}.1]$. Hence dislocation glide on pyramidal planes does not lead to an actual crosshatch on the surface, but induces a pattern of all parallel surface steps. From the two components of $[2\bar{2}.1]$ along the $[00.1]$ and $[1\bar{1}.0]$ axes the crossing angle can be derived to $\alpha = \arctan(2\sqrt{3}\frac{a}{c}) = 52.0^\circ$ for $x = 0.54$. A contribution of the alternative s- glide system to the observed pattern can be ruled out. In this case we should detect a similar pattern of surface steps however parallel to the $[\bar{1}1.1]$ vector as shown in the top right hand corner of Fig. 2(a).

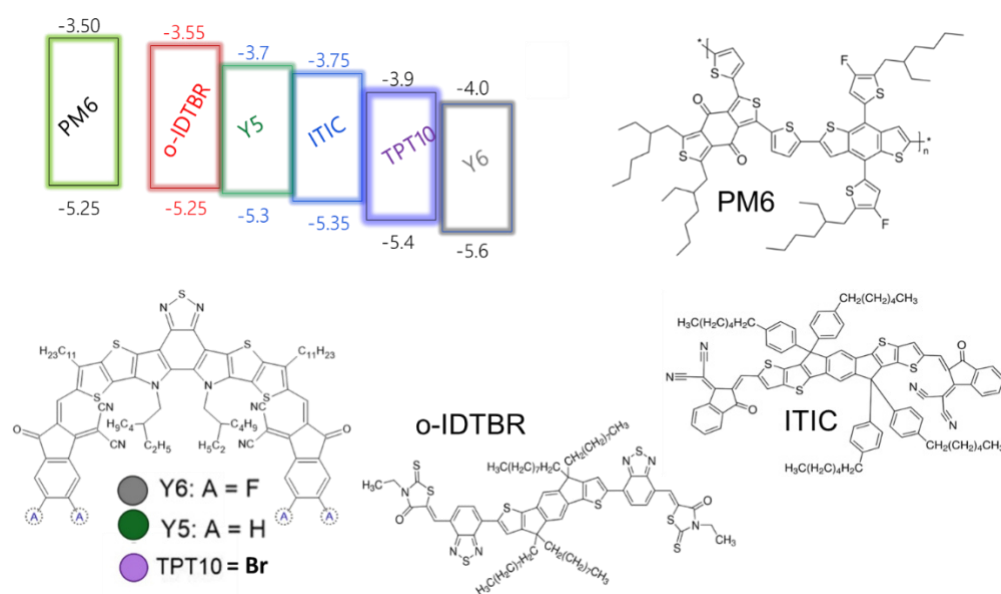
We have not observed regularly structured surfaces on α -($\text{Al}_x\text{Ga}_{1-x}$) $_2\text{O}_3$ layers for $x < 0.54$. In literature crosshatch patterns within the α -($\text{Al}_x\text{Ga}_{1-x}$) $_2\text{O}_3/\text{Al}_2\text{O}_3$ system have so far only been reported on the r-orientation for $0.47 < x < 0.88$, where they have been attributed to activation of the prismatic a plane slip system [M. Grundmann *et al.*, APL Mater. **8**, 021108 (2020); M. Grundmann *et al.*, APL **117**, 242102 (2020)]. This is further experimental evidence implying that the relative position of a- and r-planes is ideal for dislocation glide. However slip rather seems to take place at low to intermediate mismatch between layer and substrate. In case of a higher lattice mismatch other relaxation mechanisms should be dominant as for example the direct formation of misfit dislocations at the interface. Hence further investigations such as transmission electron microscopy measurements are necessary.

In conclusion we investigated strain states and mechanisms of plastic relaxation of 11 – 14 nm thick Ga_2O_3 and α -($\text{Al}_x\text{Ga}_{1-x}$) $_2\text{O}_3$ films with $x = 0.29$ and 0.54 on a-oriented Al_2O_3 substrates. HRXRD measurements reveal that for all Al contents x the epitaxial layers are anisotropically strained across two orthogonal in-plane directions as relaxation preferably occurs along $[00.1]$. Consistent with strain theory of pseudomorphic rhombohedral heterostructures the layers are free of tilt, which might be of advantage for subsequent semiconductor device fabrication. In case of intermediate lattice mismatch ($x = 0.54$) a crosshatch pattern visible on the surface gives experimental evidence of plastic relaxation through activation of dislocation glide on the pyramidal r-plane slip system. For a higher lattice mismatch ($x = 0, 0.29$) other relaxation mechanisms such as direct formation of misfit dislocations at the interface are expected to prevail.

Towards more efficient organic solar cells: a detailed study of loss pathway and its impact on overall device performance in low-offset organic solar cells

Safa Shoai

The organic semiconductor community has witnessed a rapid increase of the power conversion efficiency (PCE) of organic solar cells (OSCs), with state-of-the-art efficiencies above 19 %. This is largely due to the introduction of properly designed non-fullerene acceptors, NFAs, replacing formerly used soluble fullerene derivatives such as PCBM or ICBA. OSC based on NFAs nowadays match their inorganic competitors in terms of current production (internal quantum efficiency, IQE) owing to their large and complementary absorption, but lag behind with regards to their open circuit voltage (V_{OC}). Interestingly, NFA-based OSCs seem to require a smaller driving force for charge generation to work efficiently, with the benefit of a smaller open circuit voltage loss (the difference between the optical bandgap and the V_{OC} of device). This raises the question whether or not similar mechanisms as in fullerene-based solar cells dictate the efficiency of NFA-based devices and whether efficient OSCs with zero driving force may become feasible upon proper design of the NFA.



Scheme 1: Chemical structures and energy levels of different NFAs and PM6 as the donor material.

Free charge generation in fullerene-based solar cells was shown to comprise two steps (see Figure 1). The first is charge generation, where a photogenerated exciton in the donor or acceptor phase undergoes dissociation at the donor-acceptor interface forming an interfacial excited state (IFE). The term *local excitation* (LE) is used to refer to the relaxed exciton and the term *charge transfer* (CT) state is used to describe the interfacial excited state, recognizing that the IFE may exhibit a hybrid nature with only partial charge transfer as discussed below. Of crucial importance is the energy offset between the LE and the CT (the driving force for charge generation, $\Delta E_{LE,CT}$), which is related to the energy offset of the relevant frontier orbitals at the heterojunction through the binding energies of the LE and CT state. It is

generally accepted that $\Delta E_{LE,CT}$ should exceed a critical value to enable efficient dissociation of the singlet excitons into CT states. In the second step, namely charge separation, the interfacial CT state dissociates into a pair of free charges, the charge separated (CS) state. Because of the low dielectric constant of organic semiconductors, this dissociation is expected to be an endothermic process. Experimental and theoretical studies indicated a beneficial effect of a larger driving force for charge generation also on the efficiency of CT splitting, through the exact mechanism behind this process is still under debate. Regarding free charge recombination in fullerene-based OPV, there is conclusive evidence that it involves the (re-) formation of the interfacial CT state with its final decay to the ground state. The non-radiative V_{OC} loss $\Delta V_{OC,nrad}$ is related to the rapid depopulation of the CT state manifold through non-radiative vibronic coupling to the ground state. This means that the energetics and dynamics of the CT state determines the V_{OC} of organic heterojunction solar cells.

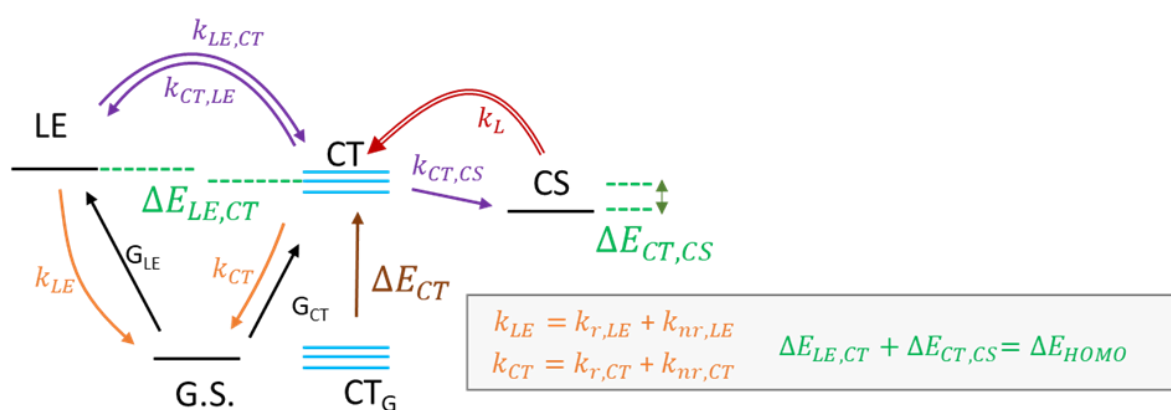


Figure 1: Photophysical processes involving interfacial CT states. Black arrows: generation pathways; single and double arrows refer to mono- and bimolecular population transfer, respectively. The box outlines radiative (r) and nonradiative (nr) contributions to the overall decay constants for LE and CT states, and the fact that the overall driving force equals the HOMO energy.

Contrary to fullerene-based devices, solar cells based on NFAs exhibit reasonably high photovoltaic performance even in the case of a small driving force, as pointed out earlier. There are indeed a few important features that set NFAs apart from fullerenes. First, state of the art NFAs have a planar conjugated backbone, allowing for the face to face pi-stacking with each other and the donor molecules. Density Function Theory (DFT) calculations predict significant electronic coupling between NFA and donor molecules. Large coupling is beneficial for the device performance: It raises the rate of the CT formation which competes with exciton recombination or trapping at defects. Several groups reported fast charge generation despite a small driving force. Another advantage of electronic coupling is that it increases the radiative efficiency of the CT recombination, thereby reducing the non-radiative voltage loss. Indeed, small nonradiative V_{OC} losses have been reported from some NFA-based blends, so it is not yet clear whether NFAs are generally beneficial in terms of a low $\Delta V_{OC,nrad}$. On the other hand, electronic coupling will increase the oscillator strength of the CT absorption and thereby reduce the radiative V_{OC} . It was proposed that the V_{OC} benefits from the strong electronic coupling mainly at low driving forces. Under these conditions, hybridization of the nominal CT state with the singlet LE on the NFA may, however, become important, leading to

the formation of a hybrid interfacial excitation. As those states exhibit only partial charge transfer, a higher binding energy relative to the CS was predicted. A second characteristic property of NFAs (differing them from fullerenes) is that they often exhibit large quadrupole moments. Such quadrupole moments will not only affect the electrostatics in the direct vicinity of the NFA molecule but more importantly, they may rather induce an overall band bending at donor-acceptor interfaces, assisting or suppressing charge separation.

Given this complex situation, the question arises whether a low energy offset limits the device efficiency predominately through a reduced rate and efficiency of CT generation, or via a stronger binding and less efficient separation of the CT state. There are conflicting answers to this question. Results from external quantum efficiency (EQE_{PV}) studies on NFA systems with different energy offset suggested that the efficiency of photocurrent generation correlates with the driving force for charge generation but not with the energy of the CT state relative to the CS state. Inefficient CT generation was proposed as the main reason for the poor performance at low driving force. This implies a direct link between the efficiency of singlet exciton dissociation (measured via transient and steady state PL measurements) and free charge generation (measured by the photovoltaic quantum efficiency EQE_{PV} or J_{SC} of the device). For this model to be correct, dissociation of the CT into the CS state cannot pose a severe limitation towards free charge generation. This, however, contradicts the view that electronic coupling causes hybridization of the interfacial states - in particular for low offset systems - increasing their binding energy. Another observation is that with decreasing driving force, not only the EQE_{PV} (and J_{SC}) decreases but also the photocurrent becomes more bias dependent. This would hint on inefficient CT dissociation as the limiting factor. However, recent studies on fullerene- or NFA-based blends provided evidence for a pronounced electric field dependence of the formation of the CT state in systems with a low (or even negative) energy offset at the heterojunction. Such scenario requires that an appreciable energetic barrier exists between the singlet LE and the CT state, which is indeed predicted by Marcus theory for the case of a small energy offset and a large reorganization energy. Electric field-induced barrier lowering would then be possible if the electric field reduces the CT state energy to a large extent; a scenario which requires the CT to carry a large electric dipole moment and/or to be highly polarizable. Significant charge delocalization of the CT state, as predicted recently for the prototypical NFA Y6, may assist such process. Evidently, detailed knowledge of the quantum characteristics of the IFS is urgently needed to reach a conclusive picture of charge formation and separation.

Furthermore, an important photovoltaic parameter, the fill factor (FF) of OSCs stands for the effectiveness of charge generation and collection, which plays a critical role in the power conversion efficiency. However, the FF value of the state-of-the-art devices still lie below their predicted limit. Similar FF values were reported for other high efficiency polymer:NFA blends and they were only achieved with thin (ca. 100 nm) active layers where charge extraction is fast. By definition, the FF summarizes all field dependent loss processes in an illuminated cell. In a donor-acceptor bulk heterojunction (BHJ) solar cell, photocurrent generation is believed to proceed through three fundamental steps: 1) the formation of an interfacial CT state through exciton diffusion and dissociation at the D/A heterojunction, competing with the decay of the exciton to the ground state; 2) dissociation of the CT state into spatially

separated independent charges competing with geminate recombination (GR) and 3) collection of the free charges at the electrodes competing with non-geminate recombination (NGR), k_2 .

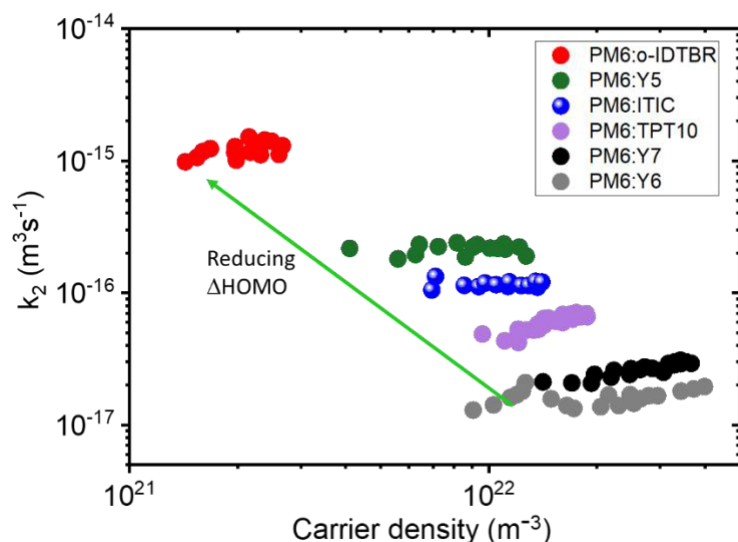


Figure 2: Bias-assisted charge extraction (BACE) measurements: recombination (k_2) as a function of carrier density (n).

We found that increasing disorder accelerates k_2 , which we attributed to increased CT recombination due to a larger density of low-lying CT states. However, we also observed that k_2 increases considerably when decreasing the S_1 -CT gap. While at first glance this could be interpreted as an increased recombination via reformation and decay of the S_1 state, our analysis shows that this pathway contributes no more than 10 % to recombination. This hints at an additional recombination channel which opens up for small offset systems. There is growing evidence that fast electron back transfer (BET) from the triplet CT to the local T_1 exciton dominates recombination for state-of-the-art NFA blends. This model is supported by the idea that BET outpaces the decay of the singlet CT state back to the ground state, simply due to the smaller energy offset between interfacial charge transfer state (CT_3) and the triplet (T_1) state which fosters vibronic coupling. As such, BET should be present and dominant in virtually all donor-acceptor blends as long as T_1 lies energetically below CT_3 . Notably, this scenario would predict that free charge generation and charge recombination proceed through different CT state manifolds, namely charge generation via the formation and splitting of CT_1 and charge recombination via the reformation and decay of CT_3 during recombination. This may explain why in many systems k_2 is fairly large, of the order of $10^{-11} \text{ cm}^3/\text{s}$, resulting in smaller than predicted FF.

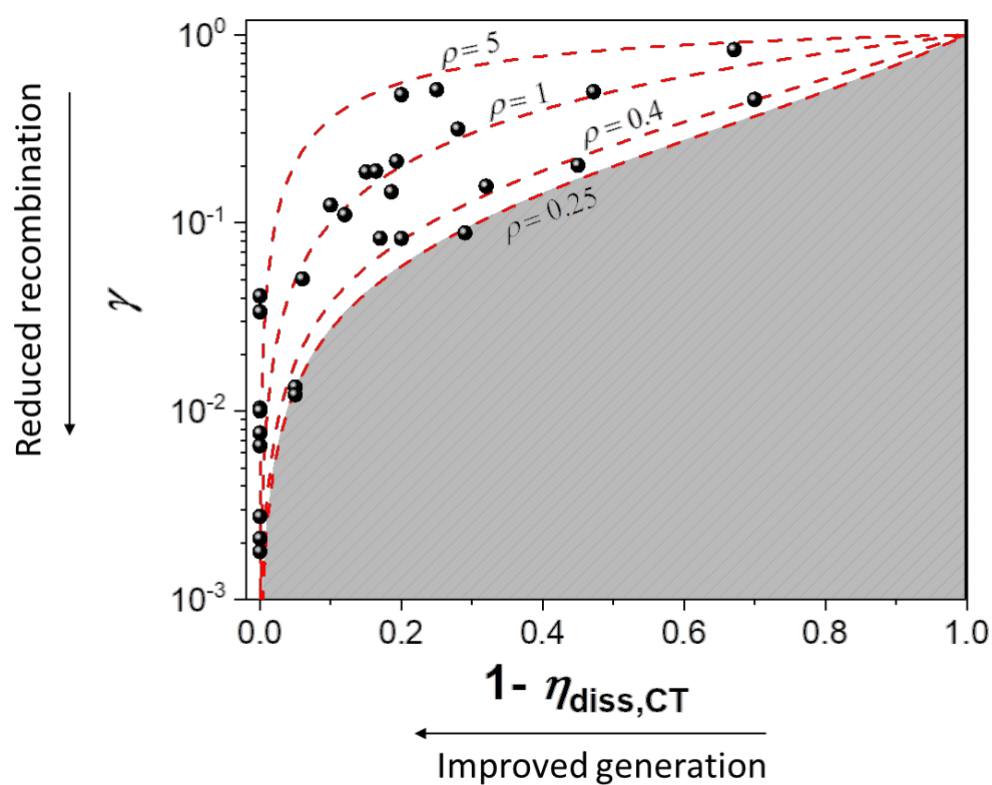


Figure 3: Correlation of data from Table 1 between γ (bimolecular recombination reduction factor) and the CT state dissociation efficiency, $\eta_{\text{diss,CT}}$ under operational conditions. The dashed lines represent different values of the spin-related factor ρ due to triplets.

GaN/ScN core/shell nanowires:

A new platform for the epitaxy of twin-free transition metal nitrides

P. John, D.V. Dinh, A. Trampert, L. Geelhaar, O. Brandt, T. Auzelle

To enhance the capabilities of conventional group III-nitride (III-N) devices that are based on the semiconductors AlN, GaN or InN, combinations with transition metal nitrides (TMNs) like NbN, ScN, ZrN or TiN are sought. These “new nitrides” bring in distinctive properties such as superconductivity, ferroelectricity, catalytic activity or plasmonic resonances in the visible spectrum. This opens up new prospects for enhancing the performance of current devices or creating innovative new ones. To fully realize this potential, successful heterostructuring of the TMNs with III-N compounds will necessitate epitaxial interfaces free from extended defects. However, while the hexagonal wurtzite phase is the most stable one for III-nitrides, cubic rock-salt is the common phase for TMNs. Due to the different crystal symmetry, rotational twins are inevitable for the growth of TMNs on the (0001) plane of GaN, SiC, or Al₂O₃ — the substrates most commonly used for III-N heterostructures and devices. Twin boundaries locally disrupt the crystal symmetry, with noticeable consequences for the optoelectronic properties of the layers. To achieve single-domain layers, we investigate here the epitaxy of GaN/ScN heterostructures on the GaN(1 $\bar{1}$ 00) surface, which has a lower symmetry than the conventional (0001) surface. Atomically smooth (1 $\bar{1}$ 00) facets can be found on the sidewalls of most GaN nanostructures prepared either top-down or bottom-up, making this surface practically relevant. We find that ScN grows free of twins on GaN(1 $\bar{1}$ 00) thanks to an unexpected epitaxial relationship.

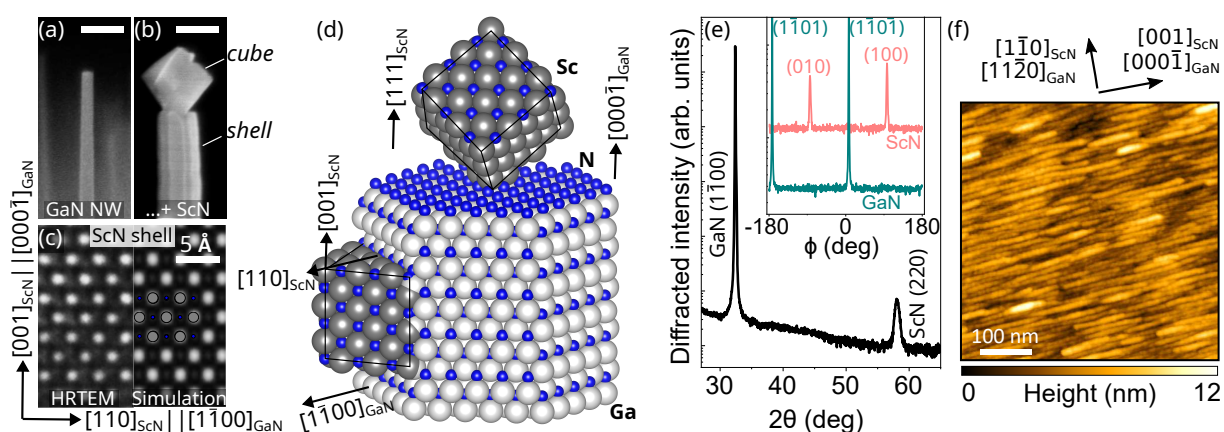


Fig. 1. Secondary electron micrograph of a GaN NW (a) before and (b) after ScN overgrowth. The length of the scale bar is 100 nm. (c) HRTEM (left) and simulation (right) of the ScN shell. The zone axis is parallel to the [1120] direction of the GaN NW core. (d) Schematic representation of the epitaxial relationships between the ScN shell and cube relative to the GaN NW core. (e) Symmetric XRD $2\theta/\omega$ scan of a 40 nm-thick ScN layer grown on GaN(1 $\bar{1}$ 00). The inset shows the XRD ϕ scan confirming the absence of twins. (f) Atomic force topograph of the ScN/GaN(1 $\bar{1}$ 00) layer.

ScN layers with a thickness between 10 and 100 nm are grown at 840 °C with a III/V ratio of 0.1 by plasma-assisted molecular beam epitaxy on self-assembled GaN

nanowires (NWs). A representative secondary electron micrograph of a GaN NW before and after ScN growth is shown in Figs. 1(a) and 1(b), respectively. The GaN NWs are grown on sputtered TiN films to obtain ensembles with a surface density lower than $10 \mu\text{m}^{-2}$ in order to expose the NW sidewalls to the incident atomic beam without shadowing from neighbouring NWs. ScN deposited on the (000 $\bar{1}$) NW top-facet forms a cubic crystallite, whereas ScN grown on the (1 $\bar{1}$ 00) NW sidewalls forms a relatively smooth layer. The ScN shell and the cube exhibit different crystallographic orientations, which are related to distinct epitaxial relationships with the underlying GaN facet. As schematized in Fig. 1(d), the ScN cube follows the same epitaxial relationship as for ScN on GaN(0001) substrates, namely ScN(111)[1 $\bar{1}$ 0]||GaN(0001)[11 $\bar{2}$ 0]. Twinning is observed between cubes located on different NWs or even within the same NW. In contrast, a very different epitaxial relationship is found for the ScN on the NW sidewalls. Figure 1(c) shows a high-resolution transmission electron micrograph (HRTEM) of the ScN shell taken with the zone axis parallel to the [11 $\bar{2}$ 0]_{GaN} direction. Comparison with the simulation confirms the orientation-relationship ScN(110)[001]||GaN(1 $\bar{1}$ 00)[0001].

To investigate this unexpected result more in detail, a 40 nm-thick ScN film is grown on a free-standing GaN(1 $\bar{1}$ 00) substrate at 740 °C. This substrate allows the formation of atomically smooth GaN surfaces that are essentially free of any imperfections. On such a reference surface, the same epitaxial relationship as for the NW shell is observed *in situ* by reflection high energy electron diffraction (RHEED) and *ex situ* by X-ray diffractometry (XRD) [Fig.1(e)]. The presence of chevrons in the ScN RHEED pattern (not shown) indicates that the layer is terminated by {100} facets. The nanofaceting of the ScN layer is confirmed by the atomic force topograph shown in Fig. 1(f), evidencing an anisotropic surface morphology consisting of periodic stripes, which are oriented along the [001]_{ScN} direction.

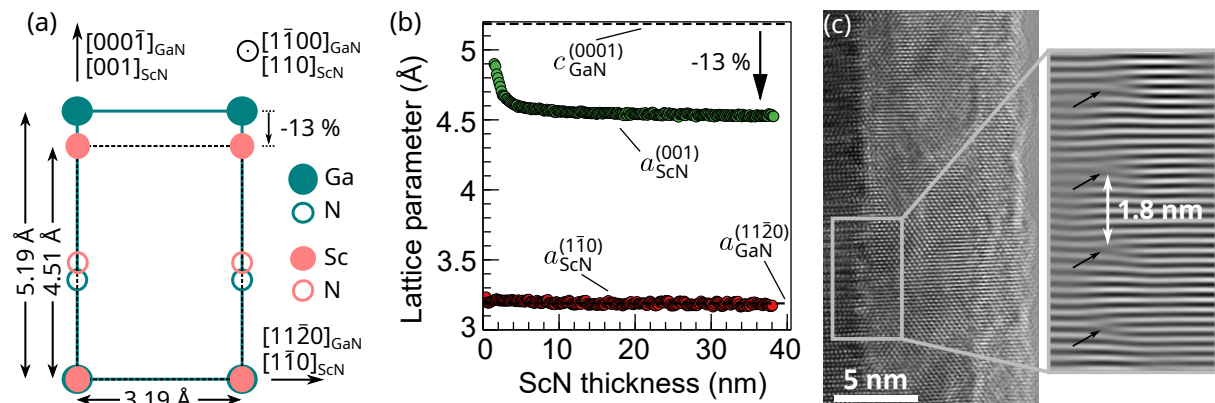


Fig. 2. (a) Schematic atomic arrangement of two-dimensional ScN(110) and GaN(1 $\bar{1}$ 00) unit meshes. (b) Evolution of the ScN lattice parameters along the [001] and [1 $\bar{1}$ 0] directions during growth. (c) HRTEM of the GaN/ScN interface along the [11 $\bar{2}$ 0]_{GaN} zone axis. The inset shows a Fourier-filtered section highlighting the GaN(0002) and ScN(002) planes. Misfit dislocations, indicated by the black arrows, are found every 1.8 nm.

Careful analysis of both the NW shells and the films indicates the absence of twin domains in the ScN. This can be understood by looking at the atomic configuration of the ScN/GaN interface, schematized in Fig. 2(a). For the experimentally determined epitaxial relationship, GaN and ScN are lattice-matched along the $[11\bar{2}0]_{\text{GaN}}$ direction and display a 13% mismatch along the $[0001]_{\text{GaN}}$ direction. No other favourable atomic configuration can be found by rotating or mirroring the ScN lattice in the interfacial plane, which is a necessary condition to achieve a single-domain ScN layer. One competing epitaxial relationship, however, would be that observed for ScN deposited on GaN(0001). Indeed, on GaN($1\bar{1}00$), such a configuration would lead to a very low epitaxial strain ($< 0.5\%$), but the mismatch between the AB_{GaN} and ABC_{ScN} plane stacking sequence would result in a much higher density of dangling bonds. Therefore, the most favourable interfacial atomic configuration appears here to be the one that minimizes the number of dangling bonds, but with significant epitaxial strain.

The relaxation of the huge uniaxial strain (13%) imposed by the GaN on the ScN layer is expected to result in a high density of misfit dislocations. Such plastic relaxation is monitored *in-situ* by recording the time evolution of the ScN reciprocal space lattice parameters with RHEED along the $[0001]_{\text{GaN}}$ and $[11\bar{2}0]_{\text{GaN}}$ azimuths. The real-space lattice parameters derived from this analysis are shown in Fig. 2(b) as a function of the thickness of the grown ScN. These data clearly evidences a uniaxial strain relaxation that takes place along the $[001]_{\text{ScN}}$ direction and occurs during the first 5 nm of ScN growth. The fast strain relaxation is also confirmed by the HRTEM image of the GaN/ScN NW core/shell interface shown in Fig. 2(c). Inverse Fourier filtering is used to highlight the GaN(0002) and ScN(002) planes, revealing the formation of a regular array of misfit dislocations at the GaN/ScN interface. The array has a periodicity of 1.8 nm, close to 1.7 nm expected for fully relaxed ScN. There is no evidence for the formation of threading dislocations or stacking faults, meaning that most of the extended defects resulting from plastic relaxation remain confined to the GaN/ScN interface. As a result, the top surface of the 40 nm-thick ScN layer deposited on GaN($1\bar{1}00$) is essentially free of strain and extended defects, which is particularly favourable for regrowth of TMN heterostructures with high structural perfection.

It is further interesting to investigate whether the epitaxial relationship found for ScN grown on GaN($1\bar{1}00$) holds when GaN is regrown on the ScN(110) film. For this purpose, 3–200 nm thick GaN layers are grown at 600–800 °C on ScN(110) films and shells. Representative TEM micrographs for the GaN/ScN/GaN core/shell structure are shown in Fig. 3. The 3 nm thick GaN shell is rougher than the underlying ScN surface and contains both zinc blende (β) and wurtzite (α) phases [Fig. 3(b)]. Surprisingly, none of these crystal phases follow the epitaxial relationship found for ScN deposited on GaN($1\bar{1}00$). The cubic domains share the same orientation as the underlying ScN, namely $\beta\text{-GaN}(110)[001]||\text{ScN}(110)[001]$, resulting in a commensurate interface with

negligible epitaxial strain [Fig. 3(c)]. The low energy of the interface is certainly a key factor in explaining the kinetic stabilization of the otherwise thermodynamically unstable β -GaN phase. However, wurtzite inclusions rapidly form in the GaN film due to the occurrence of stacking faults along the $[111]_{\beta\text{-GaN}}$ directions. Further GaN growth leads to an increase in the size of the wurtzite inclusions, which eventually cover the entire film surface for thicknesses greater than ≈ 100 nm. The epitaxial relationship at the α -GaN/ β -GaN interface is $\alpha\text{-GaN}(0001)[11\bar{2}0]||\beta\text{-GaN}(111)[1\bar{1}0]$, giving a theoretical tilt between the α -GaN($1\bar{1}03$) and ScN(110) planes of 3.3° . The presence of this tilt is confirmed by XRD analysis of GaN/ScN/GaN($1\bar{1}00$) layers. Finally, the presence of two equivalent $\{111\}$ facets on the β -GaN islands leads to the formation of two twin domains in the top α -GaN layer.

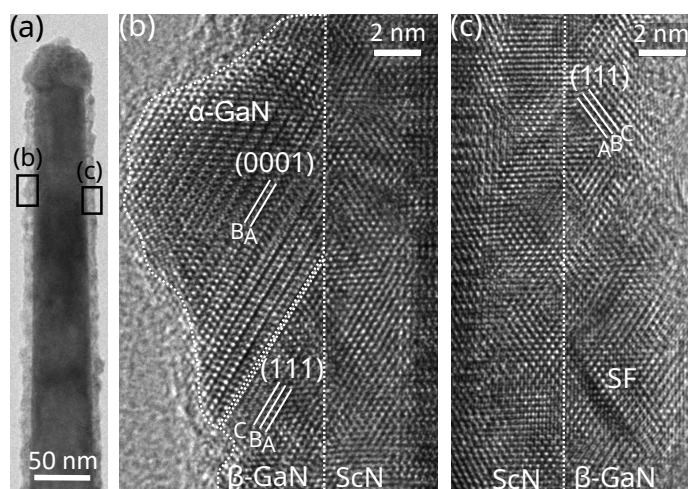


Fig. 3. TEM of a GaN/ScN core/shell NW overgrown by GaN, along the GaN $[11\bar{2}0]$ zone axis of the NW core. (a) Overview showing a shell that is characterized by smooth and rough regions. Magnification over the (b) rough and (c) smooth regions, showing the presence of mixed α -GaN/ β -GaN and pure β -GaN domains, respectively.

investigated the growth of GaN/ScN heterostructures on the low-symmetry GaN($1\bar{1}00$) surface. This approach is successful in growing twin-free ScN layers nearly strain-free for thicknesses exceeding 5 nm. It results from an unexpected epitaxial relationship that minimises the density of dangling bonds and favours rapid relaxation of the uniaxial epitaxial strain. In contrast, the deposition of GaN on the ScN/GaN($1\bar{1}00$) layer results in a twinned α -GaN layer due to the intercalation of β -GaN nuclei. Importantly, the ScN/GaN($1\bar{1}00$) layers provide a new platform for the epitaxy of twin-free TMNs like rock-salt NbN, ZrN and HfN, which are all nearly lattice-matched. These compounds hold great promise for the realisation on GaN nanostructures of all-epitaxial metal-semiconductor heterostructures with unprecedented structural quality.

The growth of phase pure β -GaN on ScN(110) appears to be hindered by the rapid formation of $\{111\}_{\beta\text{-GaN}}$ facets, which promotes the formation of wurtzite inclusions. In comparison, μm thick β -GaN layers can be grown on lattice mismatched cubic substrates such as Si or GaAs. Strategies to prevent the formation of wurtzite inclusions would therefore involve approaching 2D layer growth mode (Frank-van der Merwe) for the β -GaN film, e.g. by using surfactants.

In conclusion, we have investi-

Brief Reports

Phase-selective growth of κ - and β -Ga₂O₃ by In-mediated metal exchange catalysis in plasma-assisted molecular beam epitaxy

A. Ardenghi, O. Bierwagen, J. Lähnemann, J. Kler,¹ A. Falkenstein¹, R. De Souza,¹ M. Martin¹ and P. Mazzolini²

Lately, metal oxides have gained a lot of attention due to their potential in electronic applications. One of the most studied ones is monoclinic gallium oxide (β -Ga₂O₃), an ultra-wide bandgap material ($E_g \approx 4.8$ eV) that can potentially be the future of high voltage power devices. β -Ga₂O₃ can be grown from the melt, its electrical properties can be modulated through n-type doping and its bandgap can be tuned through Al and In alloying. Besides the thermodynamically stable β -Ga₂O₃, other polymorphs can be stabilized: orthorhombic (κ), corundum (α) defect spinel (γ) and cubic (δ).

Due to the similar bandgap and its spontaneous polarization along the [001] direction [M. B. Maccioni *et. al.*, Appl. Phys. Express **9**, 041102 (2016)] the κ -phase also potentially allows to obtain high density 2D electron gases at properly designed heterostructure interfaces. For its epitaxial growth on various substrates (*e.g.*, c-plane sapphire), molecular beam epitaxy (MBE) and pulsed laser deposition (PLD) both require the introduction of a metal catalyst [*i.e.*, In or Sn] resulting in a peculiar growth mechanism defined as metal exchange catalysis (MEXCAT). On the other hand, MEXCAT resulted in the stabilization of β -Ga₂O₃ layers when growing on different bulk β -Ga₂O₃ substrate orientations; in this process MEXCAT allowed to significantly widen the homoepitaxial growth temperature window [P. Mazzolini *et. al.*, APL Materials **8**, 011107 (2020)]. Apart from the possible role of the substrate, the stabilization of the β or κ phase upon MEXCAT could be related to the thermal meta-stability of the orthorhombic polymorph (κ -Ga₂O₃ stable up to ≈ 700 °C [R. Fornari *et. al.*, Acta Materialia **140**, 411-416 (2017)]) as well as the synthesis conditions.

In this work, we use In-mediated MEXCAT in an O-plasma assisted MBE system and identify the growth window of the β - and the κ -Ga₂O₃ polymorphs as a function of substrate and growth conditions. Specifically, we are using α -Al₂O₃ (0001) with a ($\bar{2}01$) β -Ga₂O₃ nucleation layer "nl" containing rotational domains [S. Nakagomi *et. al.*, Phys. Status Solidi A **210**, 1738-1744 (2013)] and single crystalline bulk β -Ga₂O₃ ($\bar{2}01$) substrates. Ga, In and O₂ fluxes were fixed at 3.4×10^{-7} mbar, 1.2×10^{-7} mbar and 1 sccm respectively, and the substrate temperature (T_{sub}) and fraction of activated oxygen (controlled by RF plasma power, P_{RF}) were varied systematically.

Figure 1 summarizes the main results highlighting the different phases [exemplary XRD scan reported in Fig. 2(a)] formed on the α -Al₂O₃ (0001) with a β -Ga₂O₃ ($\bar{2}01$) nucleation layer as a function of the T_{sub} and the P_{PF} . The incorporated fraction of In

¹Institute of Physical Chemistry, RWTH Aachen, D-52056 Aachen, Germany

²Department of Mathematical, Physical and Computer Sciences, University of Parma, Viale delle Scienze 7/A, 43124 Parma, Italy

has been evaluated from secondary ion mass spectroscopy measurements [exemplary depth-resolved SIMS scan reported in Fig. 2(b)].

At low temperature ($T_{sub} = 540$ °C) the growth resulted in amorphous material (sample A) the $2\theta-\omega$ scan [Fig. 2(a)] in fact just highlights diffraction peaks of the β -Ga₂O₃ nl. Notably, at this T_{sub} , without MEXCAT (*i.e.*, without additional In-flux) and regardless of the employed P_{RF} , epitaxial β -Ga₂O₃ can be deposited. This is probably due to the high amount of In incorporated in such synthesis conditions (around 15% of cation percentage, *i.e.* 15 cat.%) that increases the structural disorder.

Even at higher temperatures ($T_{sub} = 640$ °C) at relatively high plasma power ($P_{RF} = 200$ W, sample B), the grown layer is amorphous due to the high In incorporation (22 cat.%).

Therefore, to stabilize κ -Ga₂O₃ a T_{sub} between 590-660°C with a P_{RF} from 150 to 180 W are needed. Nonetheless, both plasma power and substrate temperature play a fundamental role for the incorporation of In inside the orthorhombic layers [*e.g.*, 14 cat.% for sample E ($T_{sub} = 590$ °C, $P_{PF} = 180$ W), 0.7 cat.% for sample F ($T_{sub} = 640$ °C, $P_{PF} = 180$ W), 0.02 cat.% for sample E ($T_{sub} = 660$ °C, $P_{PF} = 150$ W)]. These results on the incorporation of the catalyst during MEXCAT are qualitatively in line with previous reported data on β bulk substrates (*i.e.*, higher P_{PF} and lower T_{sub} both promote higher In content in the layers [P. Mazzolini *et. al.*, APL Materials **8**, 011107 (2020)]).

Above 660 °C only the β phase or a mixed κ/β -phase can be obtained with MEXCAT. We suggest, that this could be related to the temperature approaching the κ thermal stability limit (≈ 700 °C). In fact, for $T_{sub} > 700$ °C the β -Ga₂O₃ polymorph was always obtained with low In incorporation (0.02 cat%), regardless of the plasma power. Due to the desorption of the volatile Ga₂O, β -Ga₂O₃ heteroepitaxy by conventional plasma-assisted MBE is limited to $T_{sub} < 630$ °C. The use of In-mediated MEXCAT allows to grow β also in heteroepitaxy at significantly higher temperatures (at least for $T_{sub} = 750$ °C), which potentially allows to increase the structural quality of MBE deposited β -Ga₂O₃ heteroepitaxial layers.

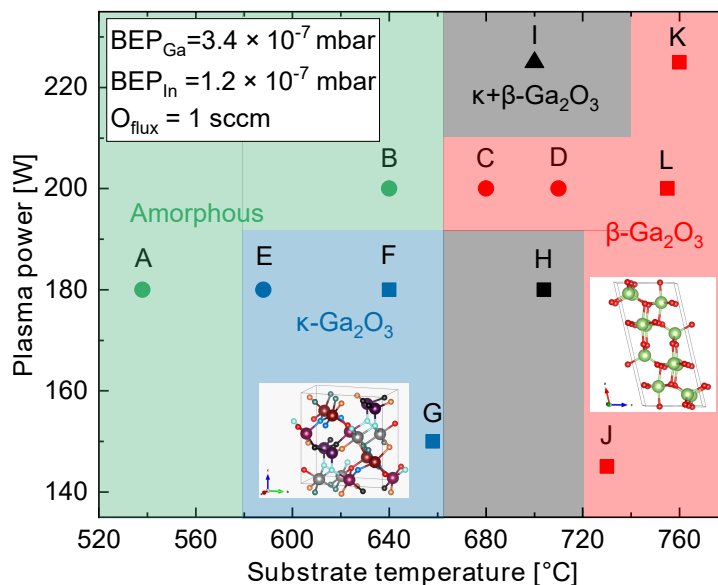


Fig. 1. Diagram on the phase obtained from the MEXCAT growth as a function of plasma power and substrate temperature, circle corresponds to samples with In > 10%, for triangle In = 3% and for square In < 1%. The β - and κ -Ga₂O₃ unit cells were created using VESTA.

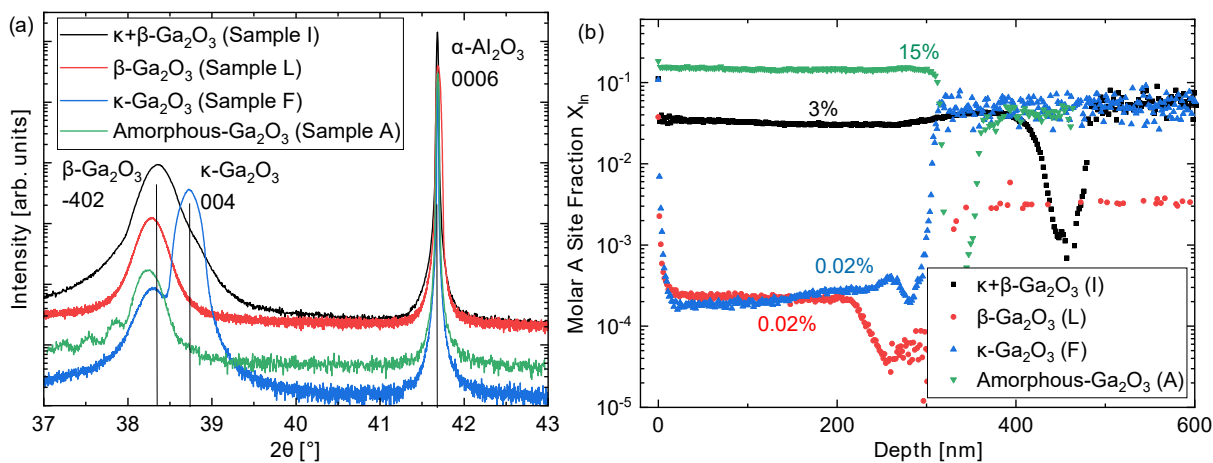


Figure 2: (a) Exemplary 2θ - ω scans highlight the difference between the different phases. (b) SIMS data for the In incorporation relative to the 2θ - ω scans showed in (a).

The growth on a single crystal $(\bar{2}01)$ β bulk substrate represents a more defined system with respect to the α - Al_2O_3 (0001) + β ($\bar{2}01$) nucleation layer: strain, structural defects, and surface roughness of the nl could affect the stabilization of the κ polymorph with MEXCAT. Other techniques already demonstrated the possibility to stabilize the κ polymorph on β - Ga_2O_3 ($\bar{2}01$) substrates [Y. Oshima *et. al.*, J. Appl. Phys. **118**, 085301 (2015)]; nonetheless, to the best of our knowledge, there is no report of MBE grown layers of κ - Ga_2O_3 on ($\bar{2}01$) β - Ga_2O_3 bulk substrates. A β - Ga_2O_3 ($\bar{2}01$) single crystal, a α - Al_2O_3 (0001) substrate with a 70/80 nm β - Ga_2O_3 ($\bar{2}01$) nucleation layer on top (grown in a previous deposition run) and a bare α - Al_2O_3 (0001) substrate were co-loaded and a MEXCAT growth in the optimized conditions identified for the κ polymorph were employed (sample G, *i.e.*, $P_{RF} = 150$ W and $T_{sub} = 660$ °C). After growth, all the substrates showed the presence of the κ -phase (Fig. 3) even if a clear difference is present. The sample with nl reproduced the result of sample G as expected. Direct deposition on α - Al_2O_3 (0001) still resulted in the orthorhombic phase as highlighted by the (004) peak from the symmetric on-axis 2θ - ω scan in Fig. 3 but with a clear difference in intensity compared to the samples grown on the β nl. This is probably related to the difficult nucleation of κ directly on the bare α - Al_2O_3 (0001) substrate. Instead, for the growth on bulk ($\bar{2}01$) β - Ga_2O_3 two different peaks at $2\theta = 38.63^\circ$ and $2\theta = 38.96^\circ$ are identified (Fig.3). The In content in the layer (0.05 cat%) was homogeneously distributed, excluding the possibility of two areas with different In content in order to explain this double peak feature. McCandless *et. al.* [McCandless *et. al.*, Jpn. J. Appl. Phys. **62**, SF1013 (2023)] was able to stabilize α - Ga_2O_3 using MEXCAT on m-plane Al_2O_3 at temperatures higher than ≥ 700 °C but, no XRD reflexes exist at $2\theta \approx 39^\circ$ for the α -phase, excluding the possibility of the coexistence of both metastable polymorphs. Due to the high temperature, also the other polymorphs (*i.e.*, γ , δ) should be

excluded. We suggest that the presence of two different κ -Ga₂O₃ crystallites could be a plausible explanation. The peak at lower 2θ angle (38.63°) is qualitatively in agreement with the lattice constant for κ -phase grown on α -Al₂O₃ (0001) as visible in comparison for the growth on the nucleation layer film. The peak at higher 2θ angle (38.96°) instead seems to reproduce the results of Nishinaka *et. al.* [Nishinaka *et. al.*, ACS Omega **5**, 29585–29592 (2020)] for the growth of single crystal κ -Ga₂O₃ on ϵ -GaFeO₃. Further experiments (e.g., Transmission electron microscopy - TEM) are still needed to properly address the probable presence of two different κ crystallites.

Our study suggests that the concurrent stabilization of the κ and β polymorphs in MEXCAT is strongly affected by the thermal stability of the metastable κ polymorph. Nevertheless, additional experiments should be performed in order to exclude the role of strain and defects on the polymorph stabilization (e.g., different β -Ga₂O₃ substrate orientations).

In summary, we have identified the growth window for β and κ -Ga₂O₃ using MEXCAT-MBE and discussed the role of deposition parameters on crystal quality

and In incorporation. Our data demonstrate how MEXCAT can be applied in order to extend the growth window of β -Ga₂O₃ also in heteroepitaxy, potentially paving the way for higher quality heteroepitaxial films. The comparison between the growth on defective β -Ga₂O₃ nucleation layers and bulk β single crystal with the very same ($\bar{2}01$) orientation suggests a minor role of strain/structural defects on the κ phase stabilization by MEXCAT. Further investigations are needed to thoroughly investigate the different obtainable crystal quality and the effect of different β substrate orientations.

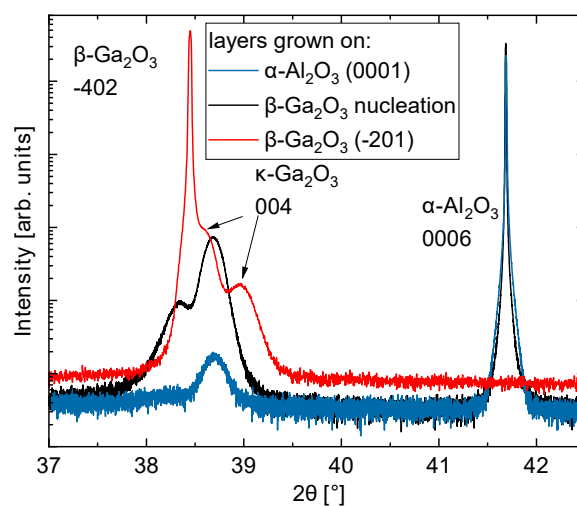


Fig. 3. 2θ - ω scans for the 3 different co-loaded substrates, for all of them we can see the presence of the κ -Ga₂O₃ (004) peak.

In-situ etching of elemental layers in oxide MBE by molecular O₂-assisted formation and evaporation of their volatile suboxide

W. Chen, K. Egbo, and O. Bierwagen

Transparent semiconducting oxides like Ga₂O₃, In₂O₃, SnO₂ and GeO₂ have been re-discovered as promising wideband gap semiconductors for applications in power electronics. Their growth as epitaxial thin films by molecular beam epitaxy (MBE) is beneficial for materials exploration and device applications, both requiring a high-degree of purity and crystallinity.

In the MBE growth of oxides possessing volatile suboxide such as Ga₂O₃, In₂O₃, SnO₂, and GeO₂ from elemental sources (In, Ga, Sn, and Ge), the provided element flux is oxidized via a first oxidization step to form suboxide (In₂O, Ga₂O, SnO, and GeO) on the substrate. The suboxide is further oxidized via a second oxidization step to form solid metal oxide film [P. Vogt *et al.*, *Phys. Rev. Materials*. **2**, 120401 (2018); W. Chen *et al.*, *APL Mater.* **11**, 071110 (2023)]. The competing desorption of the intermediately formed suboxide (typically having a higher vapor pressure than its cation element) can decrease the film growth rate. While in an oxide MBE-growth chamber, suboxides were found to form (and evaporate) readily from the elemental sources at a typical molecular O₂ background pressure present during growth [Hoffmann *et al.*, *APL Mater.* **9**, 111110 (2021)], their oxidation into the stable oxide thin film (e.g. Ga₂O₃, SnO₂, GeO₂ and SiO₂) required more reactive oxygen species, e.g. provided by an oxygen plasma.

Beyond the mere epitaxy, delivering an elemental cation flux to a substrate surface at absent anion flux in the vacuum of the growth chamber has been used for substrate-temperature calibration purposes [R. Held *et al.*, *Surf. Rev. Lett.* **5**, 913 (1998)] or as an in-situ oxide removal technique to remove the native Ga₂O₃ from GaAs (or GaN) substrates by delivering a Ga flux ("Ga polishing") [Wasilewski *et al.*, *J. Vac. Sci. Technol.* **B 22**(3) (2004)]. In the oxide-removal process, the provided element reacts with the oxide into a volatile suboxide, e.g., $4\text{Ga} + \text{Ga}_2\text{O}_3 \rightarrow 3\text{Ga}_2\text{O}$ or $\text{Ge} + \text{GeO}_2 \rightarrow 2\text{GeO}$, which desorbs at elevated substrate temperature. In-situ oxide removal is beneficial not only for preparing a clean substrate surface prior to growth but can speed up MBE growth routine by regaining a fresh substrate surface after in-situ growth calibration or unsuccessful oxide layer growth, thus eliminating the need for unloading/loading of substrates and associate temperature ramps for each growth attempt. Meanwhile, it has even been used as damage-free etching to structure highly scaled vertical and lateral 3D Ga₂O₃-based devices [Kalarickal *et al.*, *Appl. Phys. Lett.* **119**, 123503 (2021)].

Despite these beneficial applications, the elemental fluxes are prone to leave unwanted elemental adsorbates, layers, or droplets on the surface. The removal of these elemental layers, requires heating to the desorption temperature of the element, high-energy sputtering, or ex-situ wet-chemical etching — all of which may create unac-

ceptable degradation of the surface.

Taking advantage of the easy formation of volatile suboxides and their more demanding oxidation into a stable oxide film, this study demonstrates a universal in-situ approach to remove the respective elemental layer from a substrate surface at temperatures well below the desorption temperature of the element. This technique consists of heating the elemental (Me) layer to the desorption temperature of their volatile suboxide, and exposing it to O_2 while at this temperature. A corresponding schematic can be seen in Fig. 1: The O_2 molecules approach the element surface, physically adsorb, dissociate, followed by chemical adsorption (suboxide-formation reaction) and suboxide desorption as described by the following net reaction:



Here, s or l refer to the solid or liquid phase, g to the gas phase; x is the amount of elements involved in the reaction, and y refers to the cation element in the corresponding metastable suboxide (e.g. $y=2$ for Ga_2O , $y=1$ for GeO). Therefore, any excess elemental adsorbates, layers or droplets on the surface can be removed via conversion of the stable cation surface into a volatile suboxide.

We investigated the in-situ etching of Ge layers and Ga layers by an O_2 -flux experimentally on 2-inch c-plane sapphire substrates in the MBE growth chamber. The flux (Φ) of desorbing species from the layer surface was measured in-situ by line-of-sight quadrupole mass spectrometry (QMS). To assess the surface coverage, the process was additionally in-situ monitored by reflection high-energy electron diffraction (RHEED). Fig. 2(a) and (c) presents the QMS signal of Ge/GeO and Ga/Ga₂O (proportional to the desorbing flux $Ge(\Phi_{Ge})/GeO(\Phi_{GeO})$ and $Ga(\Phi_{Ga})/Ga_2O(\Phi_{Ga_2O})$, respectively) during elemental layer deposition and its subsequent etching by O_2 , while Fig. 2(b) and (d) shows corresponding RHEED images of different stages of the experiment. The Ge and Ga layer was deposited in high vacuum (background pressure 10^{-8} mbar) at a substrate temperature (T_{sub}) of 400 °C. For the layer deposition, the used Ge and Ga-cell temperatures of 1300 °C and 900 °C resulted in Ge and Ga-fluxes of $\Phi_{Ge} = 4.6 \times 10^{14} \text{ cm}^{-2}\text{s}^{-1}$ and $\Phi_{Ga} = 1.35 \times 10^{14} \text{ cm}^{-2}\text{s}^{-1}$ impinging on the substrate. When the Ge or Ga shutter is opened, a slight elemental desorption occurs which rapidly fades, corresponding to almost full adsorption of the provided flux. After closing the Ge and Ga shutter, T_{sub} was immediately increased to 700 °C and

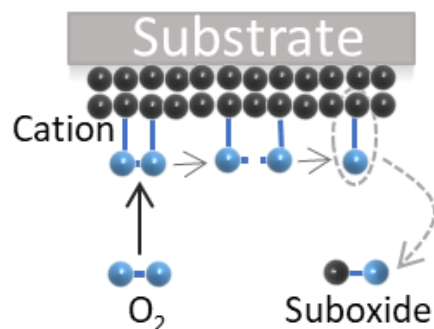


Fig. 1. Schematic describing the in-situ etching of cation layer at high substrate temperature by O_2 -flux, including the physisorption, dissociation, and chemisorption of O_2 , followed by the desorption of the formed volatile suboxide.

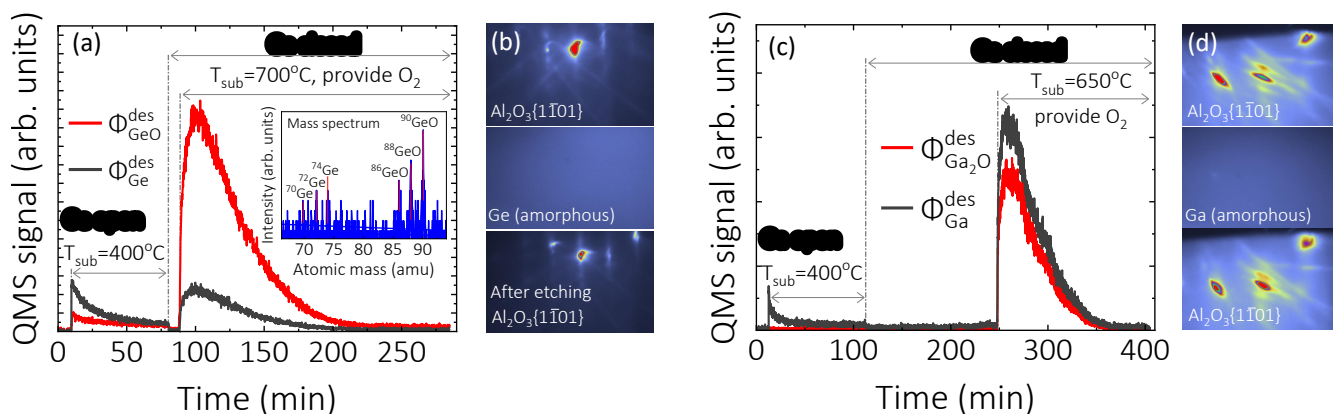


Fig. 2. Ge and Ga deposition and their O₂-assisted removal. (a) and (c) The measurement of the desorbing flux of Ge and GeO/ Ga and Ga₂O by QMS. Three stages are depicted: the deposition of the Ge/Ga layer on the c-plane sapphire substrate, the increase of the substrate temperature (T_{sub}) to enable suboxide desorption, and the subsequent in-situ etching of the already grown Ge/Ga layer. The corresponding Ge/Ga shutter opening and closing, T_{sub} as well as period of O₂ supply are marked. (b) and (d) Evolution of the RHEED pattern during growth and subsequent in situ etching of Ge/Ga: (top) c-plane sapphire substrate before growth; (middle) after growth of an amorphous Ge/Ga layer at 400 °C, and (bottom) after subsequent O₂-assisted etching of the layer at given T_{sub} .

650 °C, respectively, at 0.5 °C/s to facilitate the GeO and Ga₂O desorption in the following etching process. The elevated T_{sub} did not result in detectable desorption of the already grown cation layers (negligible QMS signal before supplying O₂), while the disappeared streaky RHEED pattern (Fig. 2(b) and (d)) clearly indicates a substrate coverage by this layer. A dramatic Φ_{GeO} and $\Phi_{\text{Ga}_2\text{O}}$ signal increase can be observed when O₂ starts impinging on the surface. This observation confirms, that O₂ reacted with Ge and Ga to form GeO and Ga₂O via $2\text{Ge}(\text{s}) + \text{O}_2(\text{g}) \rightarrow 2\text{GeO}(\text{a})$ and $4\text{Ga}(\text{s}) + \text{O}_2(\text{g}) \rightarrow 2\text{Ga}_2\text{O}(\text{a})$ at a temperature that allows the suboxides to desorb. The Φ_{GeO} and $\Phi_{\text{Ga}_2\text{O}}$ fades gradually from the maximum value, likely due to the gradual decrease of surface fraction covered by the elemental layer (the Ge and Ga signals during etching are related to the fragmentation of GeO and Ga₂O molecules by the electrons of the ionizer in the quadrupole mass spectrometer). The complete removal of the Ge and Ga layer is evidenced by the disappearance of Φ_{GeO} and $\Phi_{\text{Ga}_2\text{O}}$ and by the reappearance of the streaky RHEED pattern of the substrate (Fig. 2(b) and (d)).

To determine the efficiency of the etching process, we establish a quantitative relation of impinging O₂ flux and desorbing Ga₂O flux at varying flow rates of O₂. Fig. 3(a) illustrates the QMS signal of $\Phi_{\text{Ga}_2\text{O}}$ during the deposition of 6 equal layers of metallic Ga and their in-situ etching by O₂ at decreasing fluxes. These experiments were carried out in sequence using Ga deposition and etching temperatures of 400 °C and 650 °C, respectively. Similar to Fig. 2(c), a sharp increase of $\Phi_{\text{Ga}_2\text{O}}$ was detected when O₂ was supplied, and different O₂ fluxes are able to fully convert the Ga layers into evaporated Ga₂O, leaving behind a clean surface. Apparently, the maximum $\Phi_{\text{Ga}_2\text{O}}$ decreases with reduced impinging O₂ flux and the required time to completely remove the same amount of Ga increases simultaneously.

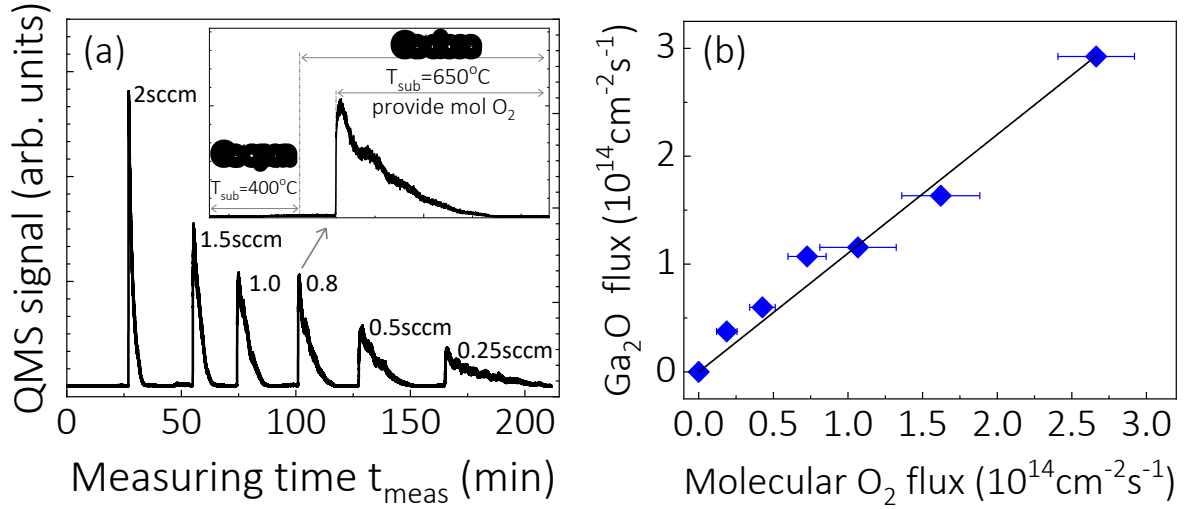


Fig. 3. Ga-deposition/ O_2 -assisted etching cycles using six different decreasing O_2 fluxes. (a) Detected Ga_2O flux by QMS as a function of time t_{meas} during metallic Ga layer deposition and its O_2 -assisted etching. Inset: Zoomed-in example of one of the processes. (b) Calibrated desorbing Ga_2O flux during etching as a function of provided O_2 flux in Fig. 3(a).

Next, we quantify and relate the Φ_{Ga_2O} measured by QMS and the impinging O_2 flux, as presented in Fig. 3(b). All Ga layers were deposited with a fixed Ga flux of $1.35 \times 10^{14} \text{ cm}^{-2}\text{s}^{-1}$ over a period of 780 s, resulting in a total surface Ga-atom coverage of $D = 1.05 \times 10^{17} \text{ cm}^{-2}$. By numerically integrating the QMS signal $Q(t)$ for Ga_2O from the time when O_2 is supplied ($t = t_0$) to the time when the whole layer is removed ($t = t_{rem}$), an equivalence relationship of $D/2 = \alpha \int_{t_0}^{t_{rem}} Q(t) dt$ was obtained and allows us to determine the calibration factor α that converts the QMS-signal Q (arb. units) into the desorbing molecular flux Φ_{Ga_2O} ($Ga_2O \text{ cm}^{-2}\text{s}^{-1}$). The O_2 flux Φ_{O_2} at the different used O_2 flow rates is calculated based on kinetic gas theory from the corresponding measured background O_2 partial pressure (P_{O_2}) according to

$$\Phi_{O_2} = P_{O_2} \times (N_A/2\pi MK_B T)^{1/2} \quad (2)$$

with Avogadro constant N_A , the molar mass M of O_2 , and O_2 temperature T . Fig. 3(b) show the peak $\Phi_{Ga_2O} = \alpha Q(t)_{max}$ observed at the begin of etching-cycle as a function of corresponding Φ_{O_2} . A linear fit yields $\Phi_{Ga_2O} = \Phi_{O_2}$ while $\Phi_{Ga_2O} = 2\Phi_{O_2}$ is theoretically expected based on the chemical reaction: $4Ga(s) + O_2(g) \rightarrow 2Ga_2O(g)$, suggesting an etching efficiency of 50%.

In conclusion, we demonstrated the use of molecular O_2 to etch elemental Ge and Ga layers via formation and desorption of their volatile suboxide at temperatures below those required to desorb the element. This method can be applied in-situ in oxide MBE to remove residual elemental layers, e.g., occurring after exposure to the cation fluxes during in-situ oxide etching or substrate temperature calibration, and is generally applicable for elemental layers whose suboxide exhibits a higher vapor pressure than the respective elements, such as B, In, La, Si, Sn, Sb, Mo, Nb, Ru, Ta, V, and W.

Optical properties of ScN layers grown on Al₂O₃(0001) by plasma-assisted molecular beam epitaxy

D. V. Dinh, F. Peiris, J. Lähnemann, O. Brandt

The rocksalt semiconductor ScN has been first synthesized more than five decades ago [Sclar, *J. Appl. Phys.* **35**, 1534 (1964)]. Recently, high-quality ScN has been grown using plasma-assisted molecular beam epitaxy (PAMBE) [Lupina *et al.*, *Appl. Phys. Lett.* **107**, 201907 (2015)] and hydride vapor phase epitaxy [Oshima *et al.*, *J. Appl. Phys.* **115**, 153508 (2014)], enabling new applications of ScN. In fact, ScN has been theoretically and experimentally proposed for electronic [Adamski *et al.*, *Appl. Phys. Lett.* **115**, 232103 (2019)] and infrared optoelectronic applications [Maurya *et al.*, *Nano Lett.* **22**, 5182 (2022)].

Compared to GaN and AlN, the optical constants (refractive index n and extinction coefficient k) of ScN are less well-known, with n having been most commonly extracted from transmittance [Dismukes *et al.*, *J. Cryst. Growth* **13**, 365 (1972)] and reflectance measurements [Deng *et al.*, *Phys. Rev. B* **91**, 045104 (2015)]. While there is a good agreement between n extracted from reflectance data for photon energies of 1–2 eV and density-functional-theory (DFT) calculations [Deng *et al.*, *op. cit.*], it is important to extend these measurements to the spectral range where ScN starts to absorb strongly, i.e., above its lowest direct band gap.

In this study, we determine the dielectric function of ScN(111) layers (thickness $d_{\text{ScN}} = 8\text{--}250$ nm) grown on Al₂O₃(0001) substrates by PAMBE using spectroscopic ellipsometry (SE) over a spectral range of 0.045–8.5 eV. Additional information on the phononic properties is obtained by Raman spectroscopy. Finally, room-temperature photoluminescence spectroscopy (RT-PL) is used to shed light on the origin of the high electron density in the layers.

Figures 1(a)–1(b) show measured and fitted Δ and Ψ spectra for the 80-nm-thick ScN layer, respectively. To fit the experimental spectra, we develop a three-layer model consisting of the Al₂O₃ substrate, the ScN layer and a top layer accounting for surface roughness modeled by a Bruggemann effective medium approximation. The thicknesses of this ScN (fitted value of 81.5 nm) and the roughness layers (8.8 nm) have been extracted from a Cauchy fit in the spectral range of 1–2 eV.

Figures 1(c)–1(d) show the results of the fits in terms of the complex refractive index $\tilde{n} = n + ik$ and the complex dielectric function $\epsilon = \tilde{n}^2 = \epsilon_1 + i\epsilon_2$, respectively. Each panel also depicts the corresponding theoretical predictions obtained from DFT calculations [R. Deng *et al.*, *op. cit.*]. The overall agreement of experiment and theory is very satisfactory. As commonly observed, the experimental features are broadened compared to the theoretical ones, reflecting a certain degree of disorder in the material.

A five-oscillator model has been used to fit the oscillators in the absorbing spec-

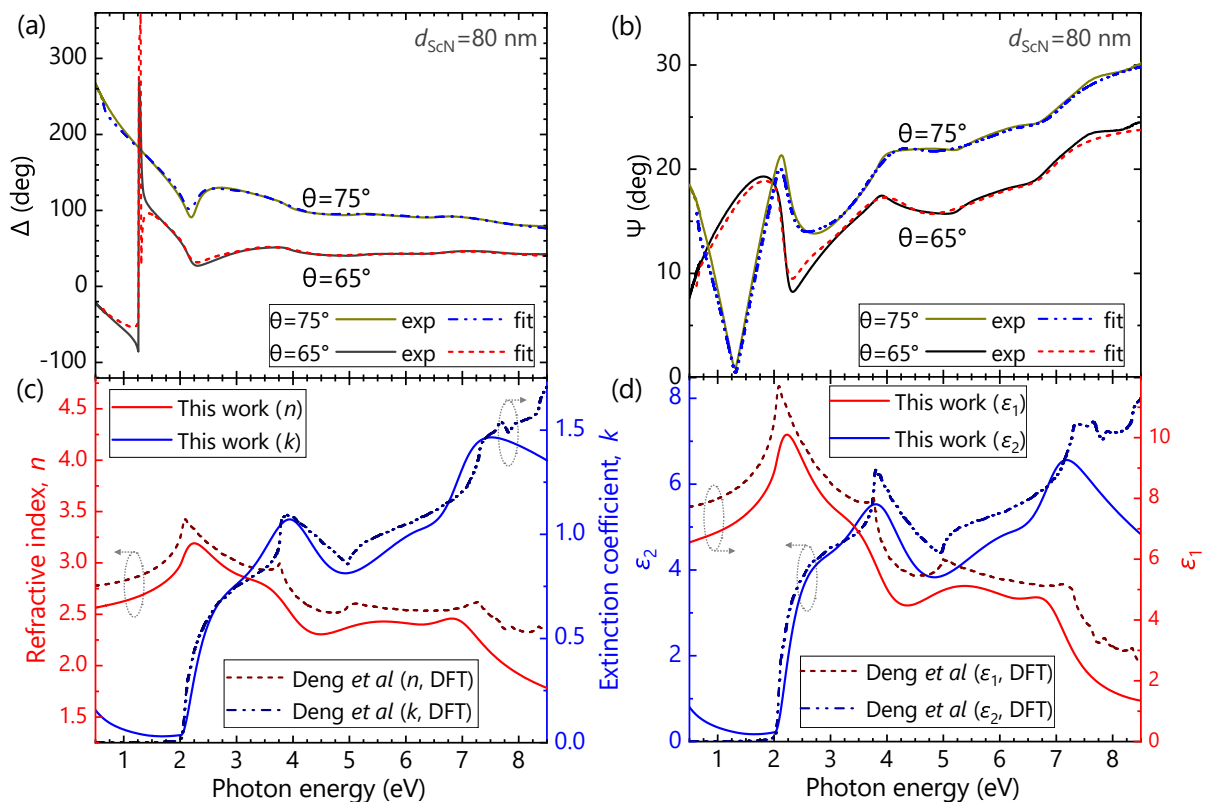


Fig. 1. (a) Δ and (b) Ψ spectra of the 80-nm-thick ScN layer (incident angles $\theta = 65$ and 75°) and their point-to-point fits. (c) Real (n) and imaginary (k) parts of the complex refractive index as obtained from the fits. (d) Corresponding real (ϵ_1) and imaginary (ϵ_2) parts of the complex dielectric function. For comparison, (c) and (d) also show the theoretical curves (DFT) obtained in [Deng *et al.*, *op. cit.*].

tral range (2–8.5 eV), where four oscillators represent band-to-band electronic transitions (Tauc-Lorentz oscillators) associated with the critical points (i.e., high-symmetry points) of the band structure of ScN and the fifth represents free electron absorption (i.e., a Drude oscillator). Fits of SE data return the energies of four oscillators representing critical points in the band structure of ScN, namely, 2.03, 3.89, 5.33, and 6.95 eV. The lowest oscillator corresponds to the lowest energy direct transition at the X point. The other three oscillators are associated with direct transitions that occur at the Γ point between the degenerate heavy- and light-hole bands and the first, second and third conduction bands, respectively.

ScN layers are invariably degenerately n -type doped, inducing a significant free-carrier absorption in the infrared spectral range. This contribution to the dielectric function is taken into account in our model by a Drude oscillator, which governs its behavior in the spectral range below 2 eV. The best fits of the SE data, assuming an effective electron mass of $0.4m_0$, return an electron density (n_e) of $1 \times 10^{20} \text{ cm}^{-3}$ and a mobility of $3.4 \text{ cm}^2 \text{ V}^{-1} \text{ s}^{-1}$, consistent with Hall-effect measurements on this layer.

The strong free-carrier absorption and the strong phonon resonances of the Al_2O_3 substrate dominate the optical response for very low photon energies. We thus investigated the vibrational properties of the ScN layers by Raman spectroscopy. In the

Raman spectrum shown in Fig. 2, some phonon modes from Al_2O_3 are detected for the 20-nm-thick layer, but are no longer present once the layer thickness exceeds the penetration depth of the exciting laser. Hence, the remaining phonon modes can be assigned to ScN. Several first-order modes at the X , W and L points of the phonon band structure of ScN are observed, which we assign to the TO(X) at 420 cm^{-1} , TO(W) at 500 cm^{-1} , LO(W) at 535 cm^{-1} and LO(L) mode at $(678 \pm 2)\text{ cm}^{-1}$, consistent with experiments conducted on bulk ScN crystals [Travaglini *et al.*, Phys. Rev. B **34**, 3876 (1986)], as well as with theory [Paudel and Lambrecht, Phys. Rev. B **79**, 085205 (2009)]. The appearance of these first-order modes is attributed to the existence of defects in the layers breaking the symmetry of the rocksalt structure [Xinh *et al.*, J. Phys. **26**, 717 (1965)]. The LO(L) spectral position is independent of the layer thickness, indicating that all of our layers are essentially fully relaxed. This is expected due to the huge lattice mismatch of 16% between ScN(111) and $\text{Al}_2\text{O}_3(0001)$.

Finally, it is of interest to examine the luminescence properties of the layers, which we do here by RT-PL measurements. The PL spectra of the layers [Fig. 3(a)] exhibit a broad band close to the lowest direct band-gap at the X point. Direct-gap PL of indirect semiconductors has been observed before, and was found to be much enhanced for heavily doped layers [Wagner and Viña, Phys. Rev. B **30**, 7030 (1984)]. This emission band stems, in general, from the recombination of majority carriers with nonthermalized minority carriers at the same point of the Brillouin zone. For the particular case of ScN, the commonly reported electron densities in excess of 10^{20} cm^{-3} result in the Fermi level entering the conduction band and a corresponding band filling [Deng *et al.*, *op. cit.*]. The degenerate doping thus facilitates the recombination of electrons populating the conduction-band minimum with hot photogenerated holes in the uppermost valence band at the X point.

The emission energy of the spectra shown in Fig. 3(a) monotonically decreases from 2.3 to 2.2 eV with increasing layer thickness, very similar to a previous observation [Lupina *et al.*, *op. cit.*]. Hall-effect measurements reveal a decrease in electron density n_e from $7.4 \times 10^{20}\text{ cm}^{-3}$ to $4.3 \times 10^{19}\text{ cm}^{-3}$ with increasing layer thickness with a corresponding reduction in band filling.

Figure 3(b) shows the dependence of the optical band gap of ScN on n_e as reported

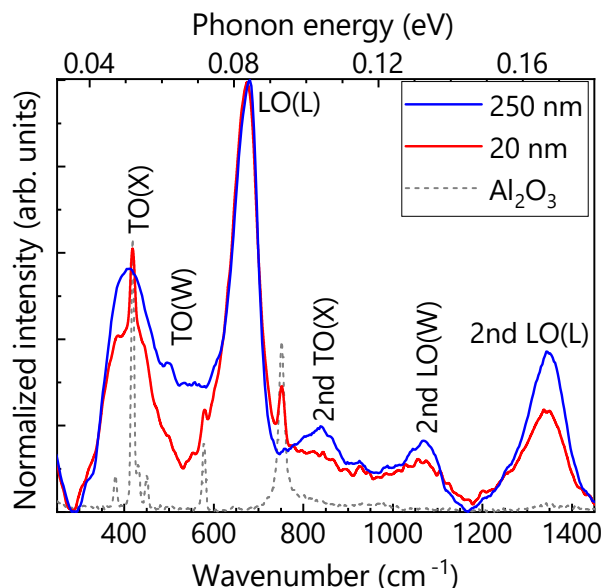


Fig. 2. Raman spectra of 20- and 250-nm-thick ScN layers on $\text{Al}_2\text{O}_3(0001)$ acquired at room temperature. The dotted line shows the Raman spectrum of the Al_2O_3 substrate for comparison.

in the literature and observed by us using SE. The optical band gap is obtained by Tauc plots with the absorption coefficients either derived from transmittance and reflectance measurements or, in our case, directly obtained from the extinction coefficient k . The strong blueshift observed for $n_e > 10^{20} \text{ cm}^{-3}$ is due to band filling and follows the theoretically expected $n_e^{2/3}$ dependence [Deng *et al.*, *op. cit.*]. While this shift would not be observable in emission for an ideal crystal, the presence of a high density of ionized donors induces disorder that relaxes \mathbf{k} conservation, allowing the recombination of electrons and holes occupying higher energy states with different \mathbf{k} vectors [Olego *et al.*, *Phys. Rev. B* **22**, 886 (1980)].

For comparison, Fig. 3(b) also shows the peak energy of the emission bands depicted in Fig. 3(a). Note, however, that this comparison is not straightforward: while absorption sets in at the Fermi energy, the PL lineshape depends on occupation, and is here complicated by the very large high-energy broadening originating from the highly nonthermal hole distribution [Wagner and Viña, *op. cit.*]. The peak energy thus does not, in general, correspond to the Fermi energy. Still, the PL peak energies are in overall agreement with the optical gap, and provide a very convenient and direct means to obtain information about the degeneracy of ScN layers.

Concluding, we have used SE in a spectral range from 0.045 to 8.5 eV to determine the optical constants of PAMBE-grown ScN layers on Al_2O_3 substrates. Fits of ellipsometry data return the energies of four oscillators representing critical points in the band structure of ScN, namely, 2.03, 3.89, 5.33, and 6.95 eV. As the infrared range is dominated by free carriers, the vibrational properties of the layers are examined by Raman spectroscopy. Despite the rocksalt structure of ScN, several first-order phonon modes are observed, suggesting a high density of point defects consistent with the high electron density deduced from Hall measurements. Finally, photoluminescence measurements reveal an emission band slightly above the lowest direct bandgap. We attribute the redshift of the peak emission energy from 2.3 to 2.2 eV with increasing layer thickness to a reduction of the O concentration in the layers.

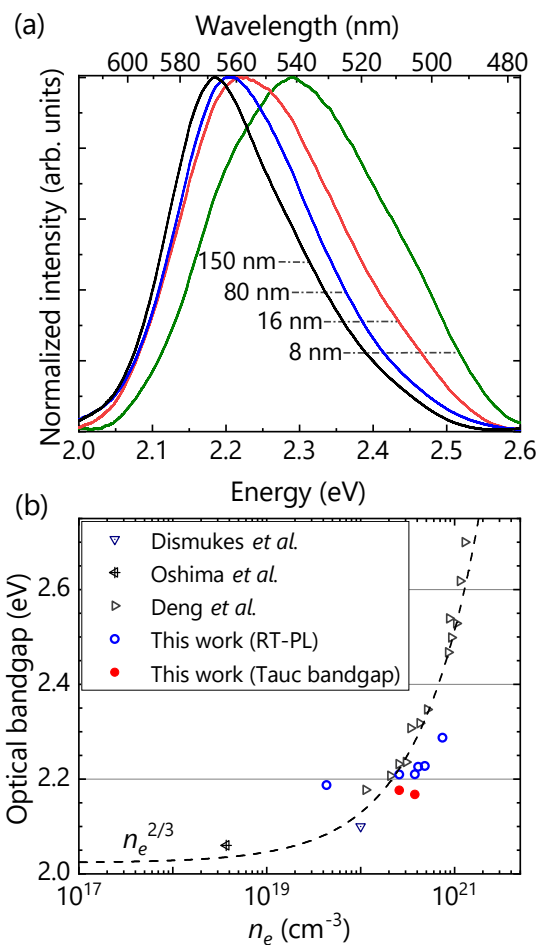


Fig. 3. (a) RT-PL spectra of ScN layers with different thicknesses. (b) PL peak energy and optical bandgap of ScN as a function of n_e . The dashed line shows an $n_e^{2/3}$ dependence as expected for a free carrier gas.

Large-area epitaxial growth and characterization of 2D $\text{Fe}_{5-x}\text{GeTe}_2/\text{WSe}_2$ ferromagnet/semiconductor van der Waals heterostructures

J. M. J. Lopes, H. Lv, M. Hanke, H. Tornatzky, C. Chen¹, J. Redwing¹, A. Trampert, R. Engel-Herbert, M. Ramsteiner

Van der Waals (vdW) heterostructures combining two-dimensional (2D) ferromagnets and other layered materials such as semiconducting transition metal dichalcogenides (e.g., MoS_2 or WSe_2) are promising building blocks for the realization of ultra-compact devices with integrated magnetic, optical, and electronic functionalities. In addition to the individual properties of each 2D crystal, phenomena such as proximity-induced exchange and spin-orbit coupling at the vdW heterointerfaces offer unique opportunities to tailor properties via a layering design.

State-of-the-art heterostructures combining 2D ferromagnets and semiconductors are commonly fabricated via sequential stacking of flakes exfoliated from bulk crystals. Despite their utility for fundamental studies and testing device concepts, exfoliation-based methods are not scalable and difficult to integrate into established device fabrication schemes. Thus, in order to maximise their potential for integration in next-generation technologies, it is crucial to develop bottom-up scalable synthesis allowing to realize uniform vdW heterostructures with high structural quality and well-defined interfaces between different 2D materials.

Another key aspect for applications is that such heterostructures should contain a 2D ferromagnet sustaining magnetic order at least up to room temperature (RT). Among several magnetic 2D compounds investigated recently, the ferromagnetic metal $\text{Fe}_{5-x}\text{GeTe}_2$ (FGT, $x \approx 0$) has been found to offer a great prospect, as it can exhibit a Curie temperatures (T_C) larger than 300 K. FGT is also an itinerant ferromagnet with properties that can be tuned by different means including gating. Similar to the other 2D Fe-Ge-Te compound Fe_3GeTe_2 (exhibiting a lower $T_C \approx 220$ K), FGT possesses a layered structure with each single layer being formed of Fe and Ge 2D slabs encapsulated by layers of Te [see Fig.1(a)].

In this work, we investigated the feasibility of growing FGT thin films via molecular beam epitaxy (MBE) on the 2D semiconductor WSe_2 . Structural characterization confirms the realization of epitaxial FGT films and the preservation of the underlying WSe_2 monolayer thick film. Magneto-transport measurements reveal that ferromagnetism persists above 300 K for FGT, similar to what is reported for FGT flakes and for MBE-grown films we recently realized on graphene templates [Lv *et al.*, Small 2302387 (2023)]. These results represent an important advance beyond exfoliation-based approaches, thus marking an important step towards novel applications.

¹Department of Materials Science and Engineering, The Pennsylvania State University, University Park, Pennsylvania 16802, United States

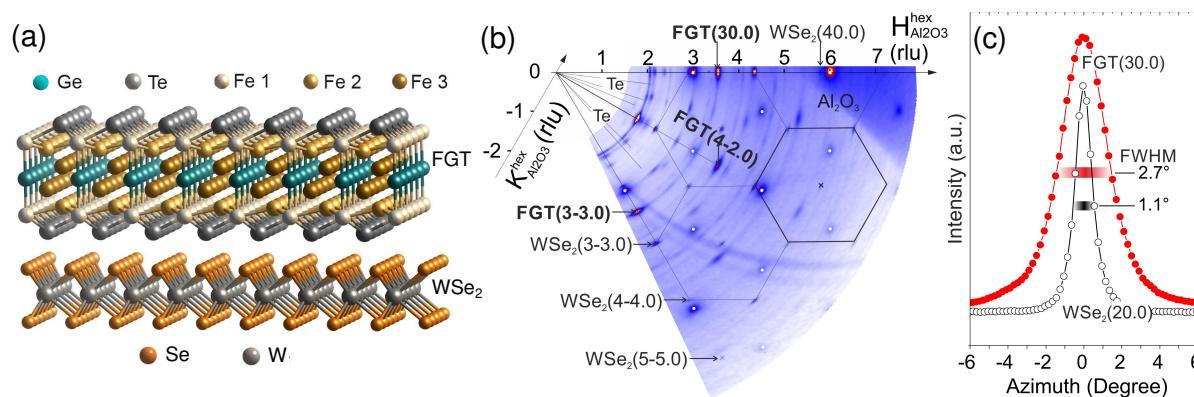


Fig. 1. (a) Schematics of the FGT/WSe₂ vdW heterostructure investigated in this work. Fe1, Fe2, and Fe3 account for the Fe atoms located in the different sublattices within a FGT single layer. (b) GID in-plane reciprocal space map obtained for a ≈ 5 nm FGT/monolayer WSe₂ heterostructure on Al₂O₃(0001). Besides the Al₂O₃(0001) reflections (marked with white dots), contributions from FGT and WSe₂ are identified. Also present are less intense contributions from a 2 nm thick Te polycrystalline capping layer. (c) Two azimuthal scans at different but fixed radial positions of the diffraction vector intersecting the (30.0) and (20.0) reflections of FGT (red) and WSe₂ (black), respectively.

FGT was grown by MBE using elemental Fe, Ge, and Te evaporated from Knudsen cells. The flux for each element was obtained by measuring the beam equivalent pressure employing a pressure gauge. For the flux ratios utilized in this study, Rutherford backscattering spectrometry (not shown) revealed an average composition close to $x = 0$, namely Fe_{4.8}GeTe₂. Continuous films with thicknesses of around 5 and 12 nm [corresponding to 5 and 12 FGT single layers; 1 single layer is ≈ 1 nm thick, formed by sequential Te/Fe/FeGe/Fe/Te slabs, see Fig. 1(a)] were prepared at a substrate temperature of 300 °C. Monolayer-thick WSe₂ films, grown via chemical vapor deposition on Al₂O₃(0001) by our external partners [Zhang *et al.*, Nano Lett. **18**, 1049 (2018)], were utilized as templates. Prior to FGT growth, the 1 cm² large WSe₂/Al₂O₃(0001) samples were *in situ* annealed at 240 °C for 20 minutes in order to remove surface contaminants. The WSe₂ surface quality and FGT growth was monitored via *in situ* reflection high energy electron diffraction (not shown). The FGT films were finally capped *in situ* with a Te layer (2 or 5 nm) deposited after sample cooling to RT. This procedure was adopted to mitigate FGT surface oxidation upon air exposure.

Grazing incidence x-ray diffraction (GID) measurements performed at the BM25B-SpLine beamline of the European Synchrotron (ESRF) in Grenoble allowed to study the epitaxial relationship between FGT and WSe₂. Fig. 1(b) shows an in-plane reciprocal space map of a Te-capped, 5-nm-thick FGT film on monolayer WSe₂ [on Al₂O₃(0001)], in which the color-coded scattered intensity in reciprocal space is plotted as a function of reciprocal lattice units (rlu), referring to the hexagonal lattice of Al₂O₃(0001). The set of reflections observed in the mapping clearly shows that there is a well-defined epitaxial relationship between FGT and WSe₂, with their (n0.0) and (n-n.0) [$n = 3\dots 5$] net planes parallelly aligned. Considering the most intense reflections from both 2D materials, we could determine their in-plane a lattice parameters: 4.008 Å for FGT, and 3.269 Å for WSe₂. This is in close agreement with values reported for single crystalline

bulk material. It is very likely that the resulting ratio $5a_{\text{FGT}} \approx 6a_{\text{WSe}_2}$ promotes the strong in-plane registry between FGT and WSe₂. The formation of a coincident-site lattice matching has also been observed for Sb₂Te₃ films grown on graphene via vdW epitaxy [Boschker *et al.*, *Sci. Rep.* **5**, 18079 (2015)]. Finally, azimuthal scans are depicted in Fig. 1(c). The angular widths, i.e. the full width at half maximum (FWHM), originate from the azimuthal spread of the respective net planes and thus serve as a quantitative measure for the epitaxial in-plane alignment. Both values (1.1° for the WSe₂ layer and 2.7° for FGT) are rather small and prove the formation of an epitaxial FGT/WSe₂ vdW heterostructure.

Raman spectroscopy was utilized to investigate the WSe₂ monolayer film before and after FGT growth (see Fig. 2). The spectrum of the as-grown WSe₂ film is dominated by a peak line at 250 cm⁻¹ which actually consists of a superposition of the E_{2g}¹ and A_g optical phonon modes. These modes are known to be nearly degenerate in monolayer WSe₂. After overgrowth with a 12 nm thick FGT film and a 5 nm thick Te cap layer, the phonon peak of the WSe₂ film is seen in the Raman spectrum together with additional lines at 125 and 145 cm⁻¹ originating from the Te cap layer.

The reduction in the WSe₂ peak intensity is caused by the optical absorption of both the incoming and scattered light in the Te/FGT stack. Its unchanged line width and peak position, however, reveal the minor impact of the overgrowth by FGT on the integrity and structural properties of the WSe₂ film. First measurements under the application of external magnetic fields indicate the occurrence of a giant magneto-optic effect in WSe₂, similar to what has been observed previously for MoS₂ [Ji *et al.*, *PNAS* **113**, 2349 (2016)]. This phenomenon is considered to be particularly valuable for the investigation of magnetic proximity fields in FGT/WSe₂ heterostructures.

Magneto-transport measurements were conducted in the temperature range between 4.3 and 360 K under applied perpendicular magnetic fields up to 0.8 T with the FGT/WSe₂ stack being patterned into a Hall bar structure (40 μm width) using standard photolithography. Figure 3 displays the transverse resistance R_{XY} for the 12 nm thick FGT on the monolayer WSe₂ measured at different temperatures during subsequent downward and upward sweeps of an external magnetic field. The clear hysteresis loops observed for temperatures up to 200 K [see Fig. 3(a)] originate from the

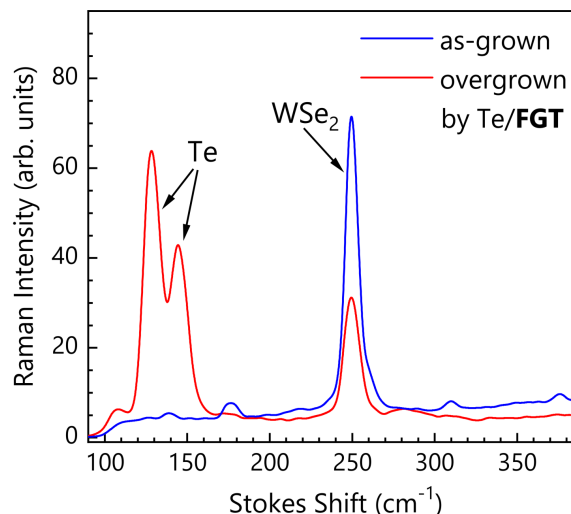


Fig. 2. Raman spectra of a WSe₂ film on Al₂O₃(0001) before (blue) and after (red) overgrowth with a 12 nm thick FGT film and a 5 nm thick Te cap layer.

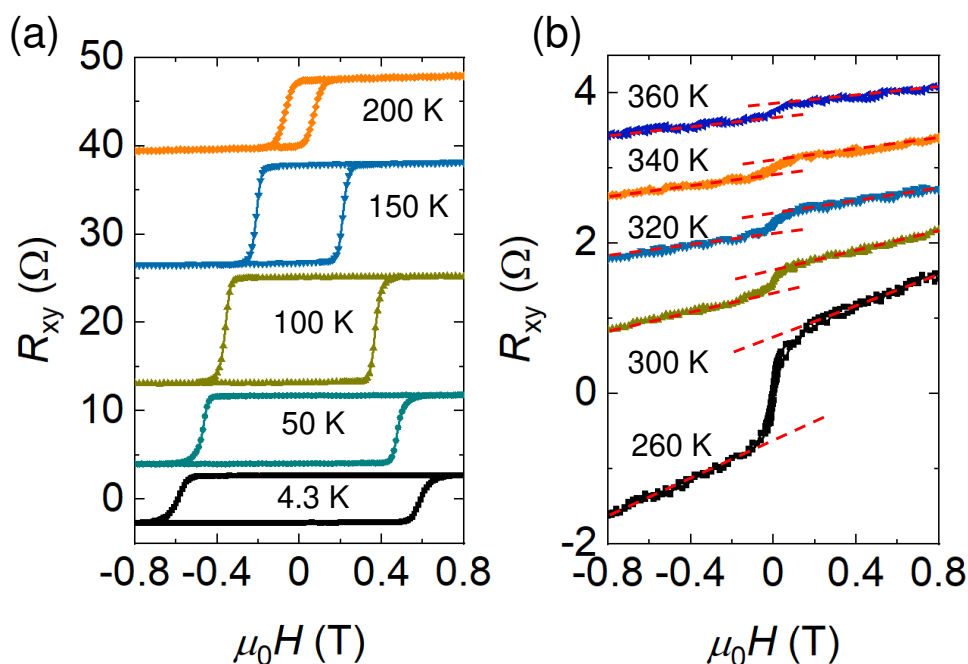


Fig. 3. Hall resistance R_{XY} measured during upward and downward sweeps of an external magnetic field at various temperatures. The R_{XY} curves are successively upshifted for clarity. The square-shaped hysteresis loops in (a) and the S-shaped R_{XY} curves in (b) result from the anomalous Hall effect (AHE).

anomalous Hall effect (AHE) in FGT. Since the AHE signal is proportional to the out-of-plane magnetization, the square shape loops reflect the ferromagnetic order in the FGT film with the observed remanence providing evidence for a perpendicular magnetic anisotropy. At temperatures above 260 K, the R_{XY} curves still exhibit S-shapes indicating ferromagnetic order up to 360 K [see Fig. 3(b)]. The missing hysteresis behavior, however, might be explained by a temperature dependent transition from an out-of-plane to an in-plane magnetic anisotropy. Further magnetometry measurements are currently under way to verify this explanation. The linear background to the R_{XY} curves, which can be clearly seen for higher temperatures, originates from the ordinary Hall effect and reveals the expected hole-like carrier transport in FGT. From the corresponding slopes, the carrier concentration in the FGT films is found to exponentially decrease with increasing temperature from $2 \times 10^{22} \text{cm}^{-3}$ to $5 \times 10^{20} \text{cm}^{-3}$, which might indicate a compensation of the hole-like conductivity due to a thermally activated increase in the population of an electron-like conduction band.

In summary, our results demonstrate the feasibility of realizing large-area, epitaxial 2D ferromagnetic/semiconductor vdW heterostructures combining FGT and WSe_2 directly on an insulating substrate. Our next steps in the research on these epitaxial FGT/ WSe_2 heterostructures (as well as on FGT/graphene, not discussed here) include not only further growth studies to enhance material quality and properties (e.g., to reach $T_C \geq 400 \text{ K}$ in FGT), but also the investigation of proximity effects at the vdW interfaces, which is highly demanded for realizing future atomically thin (opto)spintronic devices.

Optical phonon modes in LaInO₃: Lattice dynamics and complete polarization analysis of Raman-active modes

H. Tornatzky, Z. Galazka¹, R. Gillen², O. Brandt, M. Ramsteiner, M. R. Wagner

LaInO₃ is part of the family of ABO₃ perovskites, and is considered promising for next generation devices, such as for power electronics, due to its band gap of about 4.5 eV. A detailed knowledge of the phonons in LaInO₃ is important as it constitutes one of the most fundamental set of properties of a material, being the basis for mechanical and elastic properties, thermal transport as well as charge-carrier dynamics, phonon-assisted optical excitations, and many more. Though, little is known about the vibrational properties of the pure material.

In this study, we investigate the lattice dynamics by angle-resolved Raman spectroscopy and density functional theory (DFT). We experimentally observe the majority of Raman active modes and compare them to the simulated values from DFT. Furthermore, we present the DFT-derived phonon dispersion relation along the high-symmetry directions in reciprocal space and depict the oscillation patterns for selected phonons at the Γ point. Finally, we determine the relative Raman tensor elements of the observed modes from the angular dependencies of their corresponding scattering efficiencies.

LaInO₃ crystallizes in an orthorhombic crystal structure and belongs to the space group Pnma (D_{2h}^{16} in Schönflies notation). The atomic base comprises 20 atoms, giving rise to 60 phonon modes. At the Γ point these decompose into the irreducible representation:

$$\Gamma = 7A_{1g} \oplus 5B_{1g} \oplus 7B_{2g} \oplus 5B_{3g} \oplus 10B_{1u} \oplus 8B_{2u} \oplus 10B_{3u} \oplus 8A_u.$$

The modes with A_g , B_{1g} , B_{2g} and B_{3g} symmetry are Raman active; therefore, one can expect to observe 24 first-order peaks in the Raman spectra.

Raman measurements were performed with excitation wavelengths of 473 nm and 532 nm in back-scattering geometry. The Rayleigh scattered light was filtered with an edge (473 nm) or notch filter (532 nm); the light was then dispersed by a 1800 lines/mm grating and detected with a CCD. Figure 1 shows the polarized Raman spectra on the (100), (010) and (100) faces of macroscopic melt-grown crystals. The coordinate system xyz is chosen to be parallel to the a , b and c lattice vectors. By careful analysis of the polarization resolved spectra, one can identify 23 of the 24 active Raman modes, of which many overlap and are indistinguishable in unpolarized measurements. The positions of all observed modes are indicated by vertical dashed lines in figure 1. The

¹Leibniz-Institut für Kristallzüchtung, Max-Born-Str. 2, 12489 Berlin, Germany

²Friedrich-Alexander Universität Erlangen-Nürnberg, Staudtstrasse 7, 91058 Erlangen, Germany

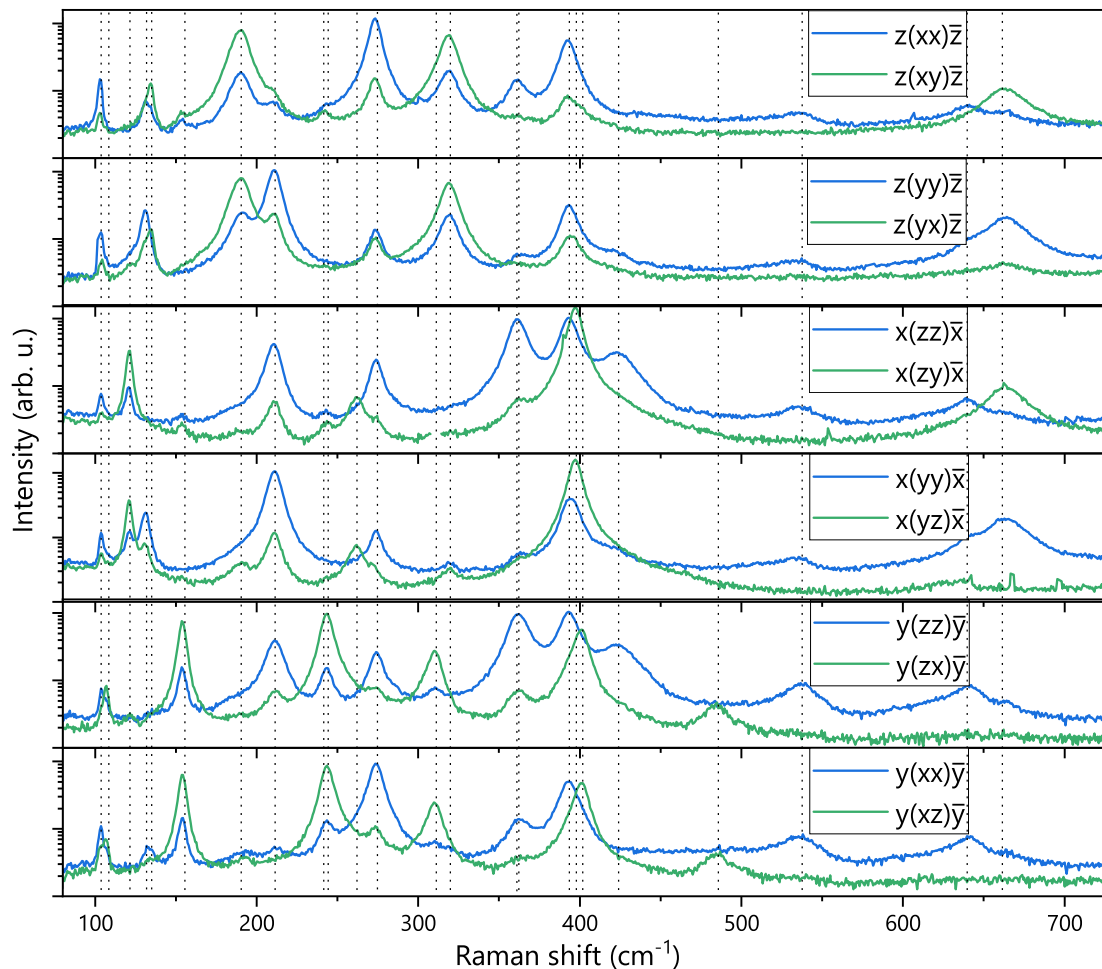


Fig. 1. Polarization-resolved Raman spectra of LaInO_3 with scattering direction and polarization parallel to the lattice vectors (scattering geometry is given in Porto notation). Vertical dashed lines indicate the position of observed Raman active phonon modes.

remaining mode is expected to be either obscured by a mode of the same symmetry or very weak in intensity.

DFT as implemented in the *Quantum Espresso*-suite [Giannozzi *et al.*, J. Phys.: Cond. Mat. **21**, 395502 (2009)], was used with Perdew-Burke-Ernzerhof functionals to calculate the phonon dispersion and derive the oscillation patterns of the phonon modes at the Γ point. Norm conserving ultra-soft pseudopotentials were used with a kinetic cutoff-energy of 80 Ry (800 Ry) for the wave function (charge density and potential). Both, electronic and vibrational properties were calculated on a regular $6 \times 6 \times 4$ k/q -grid pattern. The obtained lattice parameters of $a = 5.776 \text{ \AA}$, $b = 6.015 \text{ \AA}$ and $c = 8.348 \text{ \AA}$ are in good agreement with values from the literature and the lattice constants measured by X-ray diffraction. Figure 2 shows the obtained phonon dispersion along the high-symmetry path $\Gamma\text{XS}|\text{YTZ}|\text{UR}|\text{TX}|\text{SR}|\text{YT}$ (*cf.* inset).

The obtained phonon energies are generally in good agreement with the experiment, but deviate for some modes, especially for the high frequency modes. This deviation is considered as an effect of a non-ideal oxygen pseudopotential. The results

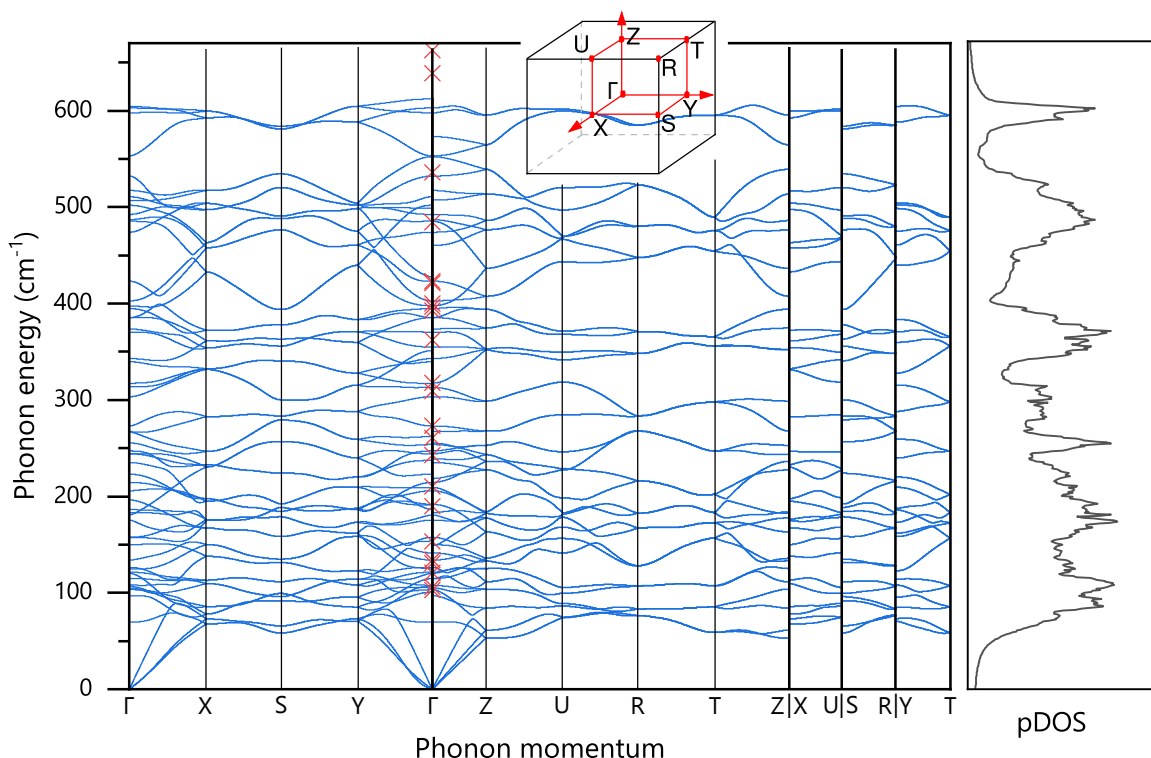


Fig. 2. Phonon dispersion in LaInO_3 . Lines (symbols) represent the simulation (experiment). The inset depicts the Brillouin zone with its high symmetry points. The right panel shows the phonon density of states (pDOS).

from DFT further suggest that the final mode to be observed experimentally is the B_{3g}^3 mode which is nearly degenerate with the A_g^6 mode. Further analysis of the data will be needed to potentially distinguish these two lines. The phonon density of states has been calculated on a regular $50 \times 50 \times 50$ q -point grid and is depicted in the right panel of figure 2.

Figure 3 depicts the oscillation patterns of the A_g^1 and B_{1g}^5 modes at the Γ point, where it is clearly seen that the first is dominated by oscillations on the La-sites, while the B_{1g}^5 mode consists entirely of oscillations of the O-sites. Hence, these two modes are examples for indicator modes to be carefully analyzed when investigating for example alloying in $\text{La}_{(1-x)}\text{Ga}_x\text{InO}_3$ (A_g^1) or doping on O-sites (B_{1g}^5).

Finally, we performed angular resolved Raman scattering, allowing us to analyze the Raman scattering efficiency for arbitrary polarization configurations. Figure 4 shows the evolution of the amplitude of the A_g^1 and B_{1g}^5 modes at 104 cm^{-1} and 319 cm^{-1} , respectively, with the rotation angle on the different crystal faces. The fit function can be calculated from the well-known

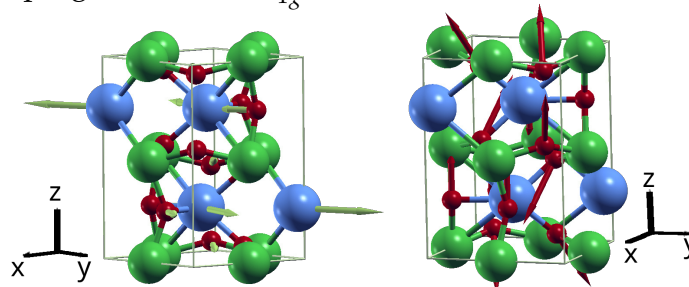


Fig. 3. Phonon displacement patterns of the (left) A_g^1 and (right) B_{1g}^5 modes in LaInO_3 . La-, In- and O-atoms are depicted in blue, green and red, respectively.

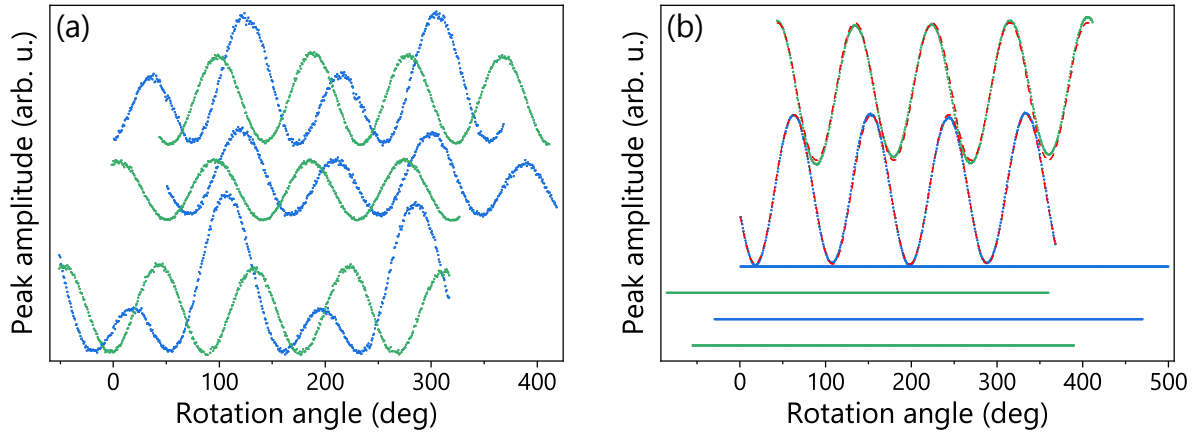


Fig. 4. (a): Angular profiles of the A_g^1 mode. Profile pairs at the top/middle/bottom correspond to the scattering on the (100)/(010)/(00 $\bar{1}$) face in parallel (blue) and crossed polarizations (green). (b): Angular profiles of the B_{1g}^5 mode. Blue and green symbols depict measurements in parallel and crossed polarization on the (001) face, while the lines represent the zero amplitude on the other faces of the crystal. Red dashed lines depict the fits. The profiles are vertically offset for clarity.

relation of the intensity with the scattering geometry and the Raman tensor $I \propto |e_i R e_s|^2$, where R is the Raman tensor of the mode and e_i and e_s are the polarization of the incident and scattered light. The latter can be parametrized, such as $e_i, e_s = (\sin(\phi), \cos(\phi), 0)$, to describe the angular dependence. For the example of the B_{1g}^5 mode the Raman tensor reads

$$B_{1g}^5: \begin{pmatrix} 0 & d & 0 \\ d & 0 & 0 \\ 0 & 0 & 0 \end{pmatrix}.$$

The angular dependence on the (001) plane then calculates as $d^2 \sin^2(2\phi)$ and $d^2 \cos^2(2\phi)$ for parallel and crossed polarization. Fitting all angular profiles of one mode, with common parameters, allows the experimental determination of the relative Raman tensor elements.

In conclusion, we have analyzed the vibrational properties in LaInO_3 both experimentally and theoretically. We were able to observe most Raman active modes and measure their angular dependent scattering behavior, which allowed us to extract the relative Raman tensor elements. Our theoretical simulations agree well with our experimental results and make oscillation patterns of the different modes available. These results provide the basis for a better understanding of the growth of LaInO_3 by the possibility to link changes in growth to the changes in the lattice (mechanical strain, alloying, phase coexistence, etc.), it allows better theoretical prediction of properties such as heat transport in devices, and it provides the necessary input for understanding phonon-mediated optical processes.

Depth-resolved and large area analysis of dislocation filter layer properties by STEM

K. Graser, S. Richter, A. Gilbert¹, L. Cerutti¹, JB. Rodriguez¹, E. Tournié¹, A. Trampert

Lattice mismatched filter layers have been shown to be very efficient for threading dislocation (TD) reduction in a variety of epitaxial systems. In particular, the III-V-semiconductor growth on highly lattice mismatched substrates that typically suffers from a high TD density, greatly benefits from the introduction of such filter layers. The bending of TDs into the interfaces due to the misfit strain and their subsequent reaction and annihilation in complex interfacial misfit dislocation (MD) networks is the basis of the TD reduction process. Understanding of the formation of these MD interface networks and their interaction with TDs is therefore an important prerequisite for further optimization of the filtering efficiency. Scanning transmission electron microscopy (STEM) is an appropriate investigation tool for the accurate analysis of defects and their interaction. Compared to conventional TEM, STEM has the advantage that defect imaging can be performed in thicker samples and disturbing bend contours and thickness fringes are almost completely suppressed. Another essential property that has hardly taken into consideration so far is the depth resolution of the dark-field STEM mode, which in principle allows to distinguish TDs and MDs and to study their interplay.

In our contribution, a sample with an AlSb dislocation filter layer for the growth of the highly lattice-mismatched GaSb-on-Si(001) system is taken as a test structure to demonstrate opportunities and the potential of depth-resolved STEM. The sample was grown by molecular beam epitaxy at the Institut d'Electronique et des Systèmes of the university of Montpellier (joint DFG-ANR project). The STEM observations were carried out with a Jeol 2100F electron microscope operating at 200 kV.

The complete layer structure of the sample is schematically shown in Fig. 1(a). Plan-view bright-field STEM measurements were performed at different positions of the structure and over large areas as wide as $10 \times 10 \mu\text{m}^2$ in order to precisely determine the dislocation density with sufficient statistical accuracy. Figure 1(b) shows the results of the TD density as a function of the layer thickness. The position of the AlSb filter layer is marked by vertical lines in the graph. For a pure GaSb epi-layer on Si, a TD density proportional to $t^{-5/3}$ is expected, where t is the GaSb layer thickness [W. Quian *et al.*, J. Electrochem. Soc. **144**, 1430 (1997)]. This progression is represented by the blue line in the figure and fitted by the measured TD density of a reference sample grown without the AlSb layer. The strong TDD reduction for sample with filter layer is obvious as marked by the red stars. Additionally, it can be conducted that the filter ef-

¹Institut d'Electronique et des Systèmes, Université de Montpellier

efficiency based on the lower interface is enhanced compared to the upper one. This fact is also correlated with the fundamentally different character of the misfit dislocation (MD) networks in both interfaces as reflected by the plan-view BF-STEM images in Fig. 1(c) and (d). While the upper AlSb interface exhibits a regular cross-network of dislocation lines along the two perpendicular $\langle 110 \rangle$ -directions, a more complex MD network with only short dislocation segments is observed in the lower interface. These very dissimilar MD networks in terms of arrangement and dislocation type should have different influence on the propagation and interaction with TDs in the adjacent layers and thus for the filter property. To explore this interplay, it is necessary to locate the exact position of the dislocation within the sample, which requires depth-resolved defect imaging.

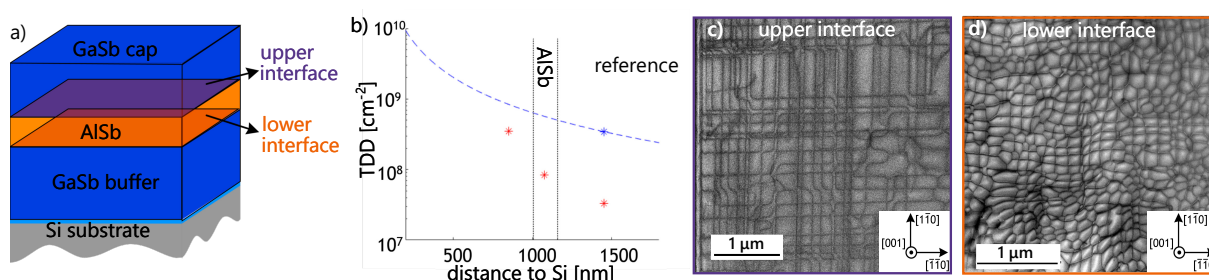


Fig. 1. Interfacial MD networks and their effect on TD density. (a): Depiction of the layer structure of the sample. (b): Measured TD density values at different distances above the Si substrate in red. The blue line indicates the expected TD density without filter layer based on a measurement on a pure GaSb-on-Si sample. Vertical lines mark the positions of the two AlSb interfaces. (c) and (d): BF-STEM images of the upper and lower AlSb interface respectively.

Annular dark-field (ADF) STEM provides the ability to image the location of dislocations in the sample and distinguish superimposed dislocation structures. To illustrate this performance capability, a series of plan-view ADF-STEM images representing the same sample area are shown in Fig. 2, where the angular collection range β of the ADF detector is systematically varied by changing the camera length. The micrographs show the dislocation structure around the AlSb layer including its upper and lower interface, whereas, due to the slightly wedge shape of the TEM foil, the lower interface is incomplete [see schematic in Fig. 2 (a)]. The sample was oriented in the so-called bottom-configuration, i.e., the lower interface is located close to the entrant foil surface. Based on the angular collection range of the detector, the ADF images are classified into three regimes: low-angle (LA) ADF with $8 < \beta < 20$ mrad, middle-angle (MA) ADF with $33 < \beta < 90$ mrad, and high-angle (HA) ADF with $80 < \beta < 210$ mrad, respectively. The LAADF image in Fig. 2 (b) reveals both networks with strong dislocation contrast, i.e. the contrast is independent from dislocation depth in the foil. The dislocation of the complex network is visible as bright-dark lines while the dislocations of the cross-network has pure dark contrast in accordance to the different MD types. Otherwise, both dislocation networks appear in pure bright contrast in the MAADF

image in Fig. 2(c), however, the cross-network that is deeper inside the foil is stronger. On the contrary, in HAADF in Fig. 2(d) the complex network closer to the entrant foil surface displays a strong dark-bright contrast complementary to the contrast in LAADF, while the cross-network disappears almost completely.

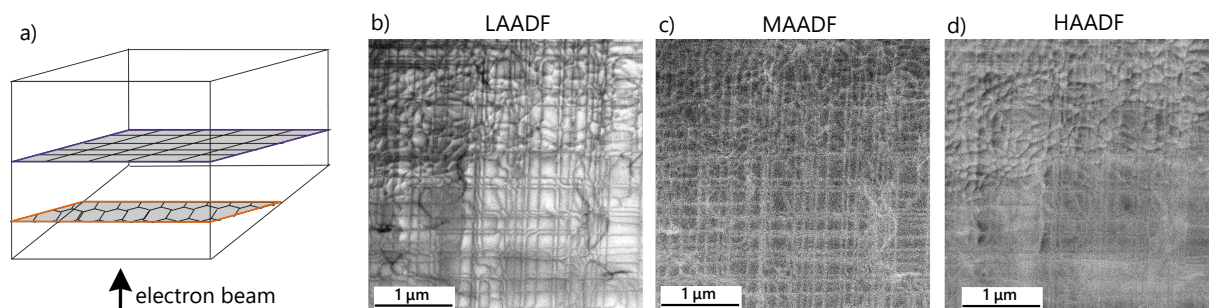


Fig. 2. ADF-STEM images of a conventionally prepared plan-view specimen. (a) depicts the position of the two MD networks inside the wedge shaped specimen. (b) - (d) show a series of ADF-STEM micrographs in the LAADF, the MAADF and the HAADF regime respectively.

The results verify that the ADF image contrast of dislocations not only dependent on the camera length but also on their position inside the sample. The observations can be explained by different scattering processes dominating the angular ranges covered by the DF detector for the different camera lengths. In fact, in LAADF the contrast is predominated by Bragg diffraction. The dislocation is visible due to the long-range strain field (bending of the lattice planes) around the dislocation core, resulting in a local change in the Bragg condition. The MAADF range is characterized by diffuse "Huang" scattering that originates from the strong atomic displacements in the dislocation core. This effect is amplified for dislocations located deeper inside the specimen [E. Oveisi *et al.*, *Ultramicroscopy* **200**, 139 (2019)], which explains the stronger contrast of the cross-network in Fig. 3(c). In the HAADF range de-channelling contributes to the defect image contrast. Channelling appears when the electron beam travels along the directions of atomic rows of the crystal. The beam is then focused by the potentials of the atomic columns and its forward propagation gets enhanced. The increased intensity along the atomic rows results in a stronger Rutherford scattering into larger angles leading to a higher intensity in the HAADF image. The bending of atomic planes around the dislocation core disturbs this channelling effect and results into a de-channelling and a reduced intensity in the HAADF image. The de-channeling is also the reason why the contrast of dislocations deep inside the specimen disappears in HAADF. A dislocation located close to the bottom surface of the specimen has no influence on the beam propagation because all its intensity has already been de-channelled. In this way, ADF-STEM allows to specify the vertical positions of dislocations in the specimen and to each other.

The depth-resolved ADF method has been applied to investigate the complex interplay between TDs and the interface MD network. Figure 3 shows two examples from the

upper and lower filter layer interface, respectively, based on combined BF and HAADF STEM images, each taken in top-configuration, i.e., with wafer surface as the entrant foil surface of the electrons. The BF image in Fig. 3(a) reveals dislocation bending out of the interface by glide process. The contrast enhancement of these curved dislocations in the HAADF image in Fig. 3(b) proves that they extend from the network into the overlying GaSb cap layer. Additionally, the exit points of the TDs at the sample surface appear with a light-dark contrast. This is due to the distortion of the surface caused by the strain field of the dislocations, which is responsible for de-channelling contrast [V. Grillo *et. al.*, J. Cryst. Growth **318**, 1151 (2011)].

Figure 3 (c) and (d) show a typical part of the complex MD network of the lower AlSb interface and the AlSb layer above. Again, the surface exit points of TDs coming out of the interfacial network are clearly visible in the HAADF micrograph. They are marked with orange circles in the associated BF image. On the other hand, in BF more ending dislocation lines in the network can be observed (marked by green circles). These are positions, where TDs from the GaSb buffer below bend into the interface. In contrast to the upper interface the TDs here seem to form preferentially at nodes of the network as a result of dislocation interaction and coalescence instead of the bending of single MDs out of the interface.

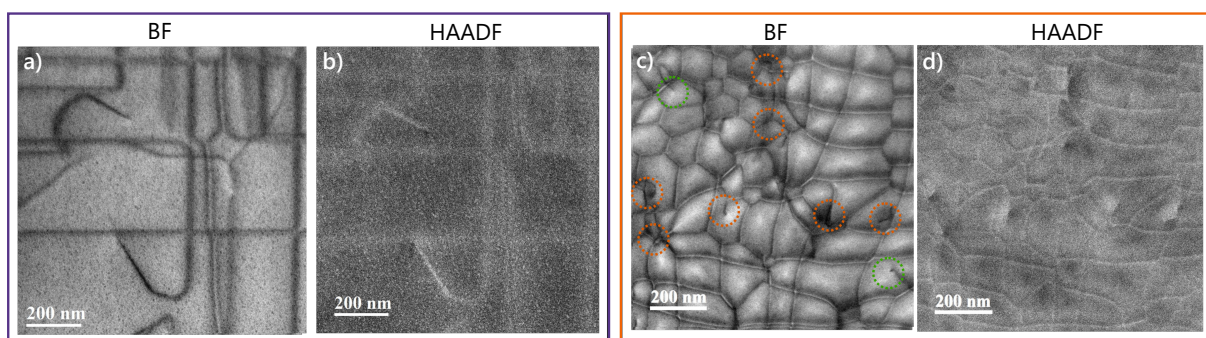


Fig. 3. Plan-view STEM images showing the formation of TDs in the upper (a), (b) and in the lower (c), (d) AlSb-interface. (a), (c) and (b),(d) are recorded in the BF and HAADF mode respectively. The orange and green circles in (c) emphasize points where TDs were running out and into the interface.

In summary, plan-view STEM provides a variety of information about dislocation structures. TDs and MD networks can be observed and characterized over large areas. In addition, the depth-resolved contrast of ADF-STEM allows determination of the vertical position of dislocations in the sample and an investigation of the interplay of TDs with the MD network. In a next step, simulations will be used to consider the influence of the Burgers vector of the dislocation on the depth-resolved ADF contrast. The method presented here are not only helpful for studying filter layer structures, but also for all structures where dislocation propagation and interaction play an important role.

Three-dimensional reconstruction of interface alloy disorder in Ge/GeSi asymmetrically coupled quantum wells using electron tomography

E. Paysen, G. Capellini^{1,2}, E.T. Simola¹, L. Di Gaspare¹, M. De Seta¹, M. Virgilio³ and A. Trampert

A current challenge in realizing an n-type Ge/GeSi THz quantum cascade laser (QCL) compatible with Si-based CMOS fabrication is the subnanometric control over the buried interfaces. Interdiffusion for Ge-rich Si-Ge systems is strong, complicating the growth of layers with thicknesses of a few nanometres. In addition, the compressively strained Ge quantum wells (QWs) and tensile strained GeSi barriers affect the interdiffusion as well as the roughening of the interfaces in three-dimensions (3D). To support this QCL design, the 3D structure of the interfaces can be reconstructed and analysed at a sub-nm-scale using electron tomography (ET). In this report, we present the important structural properties of Ge/Ge_{0.8}Si_{0.2} interfaces of asymmetric coupled QWs (ACQWs) quantitatively determined through ET. The interface alloy disorder in this structure is interpreted as the key property that influences and connects all other structural interface features.

The sample is grown by ultrahigh-vacuum chemical vapour deposition on a Si(001) substrate. A stack of 20 Ge/Ge_{0.8}Si_{0.2} ACQW modules is deposited on a Si-Ge reverse-graded virtual substrate tuned for strain compensation in the ACQWs. A single module consists of a thin (5 nm) and thick (12 nm) Ge QW coupled by a thin GeSi barrier (2.3 nm) and separated from the other QW pairs across a thick GeSi layer (20 nm).

For the tomographic examination, an about 200-nm-thick needle, see Fig. 1(a), is prepared with focused Ga⁺-ion beam milling with its longitudinal axis coinciding with the direction of growth. We examined the four uppermost modules A to D with ET (cf. Fig. 1(b)), but the lower modules are also accessible for tomographic investigation.

In ET, a 3D image or tomogram of the sample is reconstructed from a series of two-dimensional projections from different viewing angles. We use high-angle annular dark-field (HAADF) scanning transmission electron microscopy images as projections like Fig. 1(b) that show a chemically sensitive contrast, making the Ge and GeSi layers distinguishable. But their relatively small compositional difference is reflected in the contrast. To enhance the contrast that is transferred to the tomogram, one can linearize the HAADF intensity of the projections before reconstruction. Ultimately, the tomogram allows for various analyses and visualizations. For example, Fig. 1(c) illustrates the reconstructed interfaces as iso-concentration surfaces also highlighting the Ge QWs.

¹Dipartimento di Scienze, Università degli Studi Roma Tre, Roma, Italy

²IHP – Leibniz-Institut für innovative Mikroelektronik, Frankfurt (Oder), Germany

³Dipartimento di Fisica Enrico Fermi, Università di Pisa, Pisa, Italy

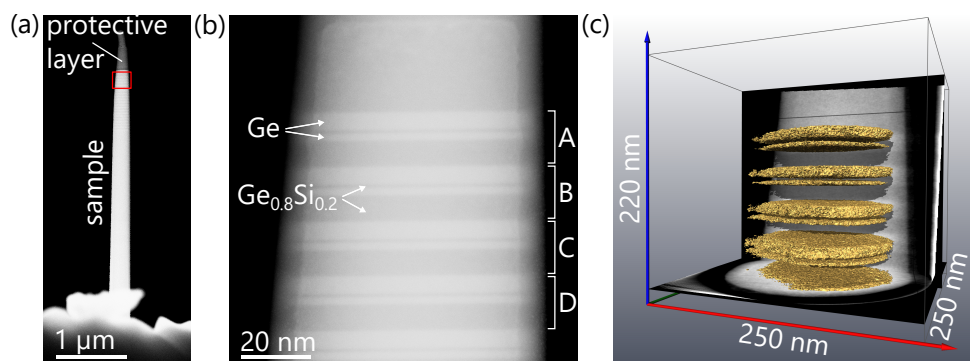


Fig. 1. Dark-field STEM images of (a) the needle sample with the target region marked by the red box and (b) a close-up with the top four ACQW modules A to D. (c) Iso-concentration surfaces in yellow from the reconstructed tomogram to visualize the interfaces or Ge QWs.

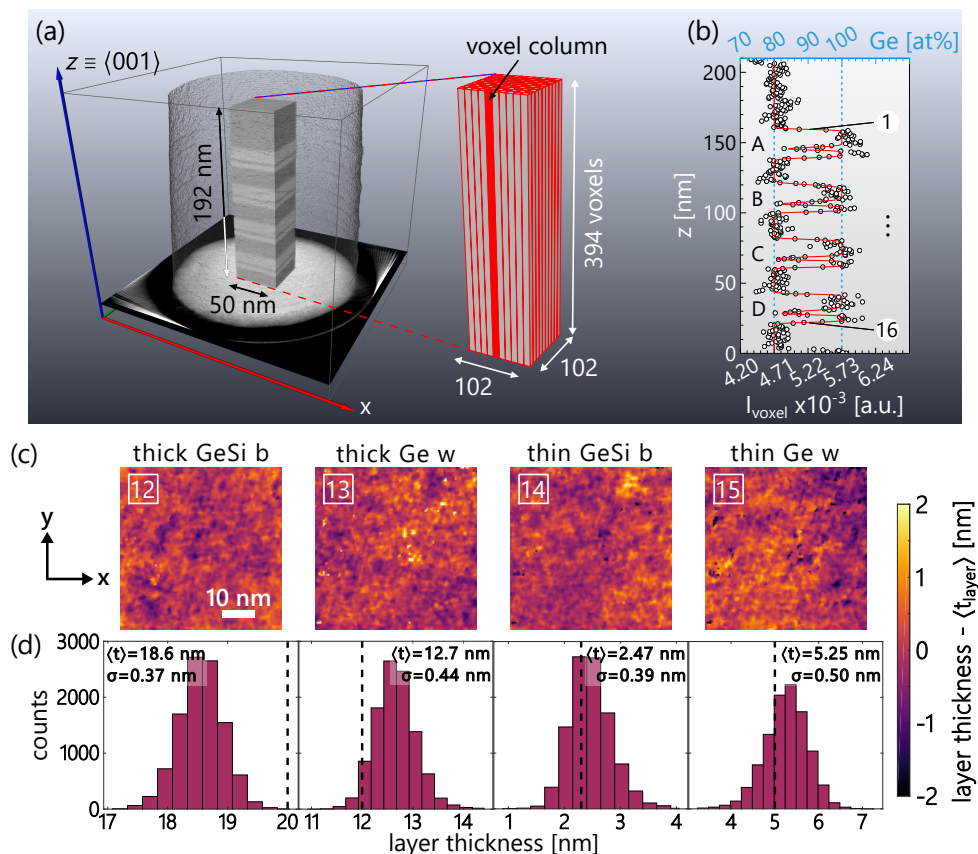


Fig. 2. To determine interface widths and layer thicknesses, a cuboid (a) with a base area of $(50 \times 50) \text{ nm}^2$ is observed in the tomogram. For each of its 102×102 voxel columns, the layer structure is simulated with sigmoidal functions, as shown in (b) with the red line. The interfaces (white circles) and layers are numbered from top to bottom. Exemplary for module D: (c) Maps of the laterally slightly varying layer thickness determined from the simulations (b – barrier, w – well) and (d) corresponding histograms with mean layer thickness $\langle t \rangle$ and standard deviation σ . The dashed line indicates the nominal thickness in each case.

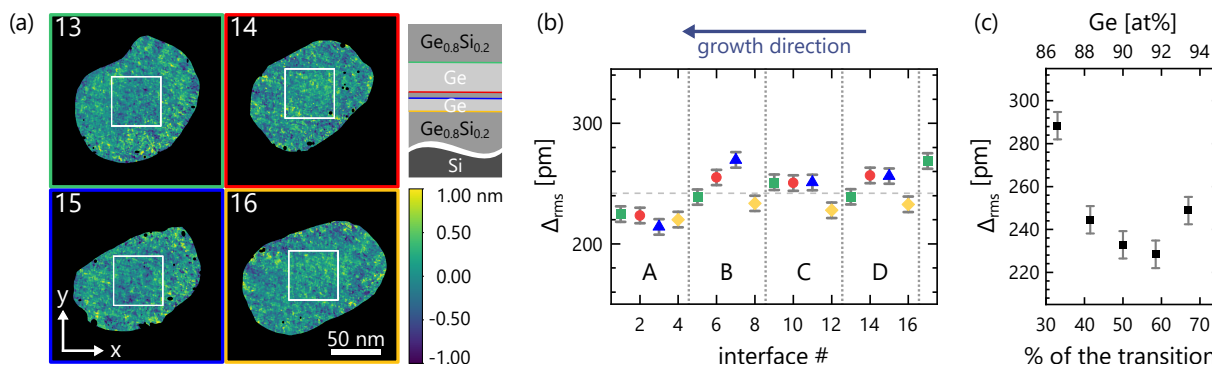


Fig. 3. (a) The topographic maps of the interfaces from module D used to determine the interface morphology. The sketch on the right shows the corresponding color coding of the 4 repeating interfaces. (b) Rms roughness values were obtained for all interfaces within $(50 \times 50) \text{ nm}^2$ regions, as indicated by the white squares in (a). (c) Rms values depending on Ge concentration or percentage of intensity gradient at a single interface (here: interface 16). The error bars represent the uncertainty due to statistical noise.

To determine interface intermixing and fluctuations in layer thickness, the reconstructed layer sequence is simulated. For this, we consider a cuboid from the tomogram as illustrated in Fig. 2(a). For each of its voxel columns (voxel = 3D pixel), the intensity profile reflecting the layer sequence of QWs and barriers is simulated with sigmoidal functions like in Fig. 2(b). Note that the tomogram intensity I_{voxel} is proportional to the at% of Ge in this case. Plotting the resulting simulation parameters in the (x, y) plane yields maps of the intermixing width W for each individual interface (not shown here) or maps of the layers' thickness t as in Fig. 2(c) for module D. The maps reveal a highly uniform layer thickness distribution in lateral dimensions, with minimal fluctuations around mean values in the investigated field of view. This is confirmed by corresponding histograms showing a narrow Gaussian distribution in Fig. 2(d). The $\pm 0.4(5) \text{ nm}$ standard deviation is small and within the unit cell's size. The mean thickness values $\langle t \rangle$ predominantly match nominal values (dashed lines), highlighting excellent growth control over the ACQWs.

To analyse the morphological roughness of an interface, an iso-concentration surface is extracted from the center of its intermixing region, i.e., at the mean Ge concentration between adjacent layers. These surfaces are then rasterized into topographic height maps. Figure 3(a) presents such maps of four consecutive interfaces in module D. The absence of observable morphological anisotropy or strain-induced roughness change aligns with the intended epitaxial strain compensation within a single ACQW module. Quantifying roughness, the root mean square (rms) value $\Delta_{\text{rms}} = \left(\frac{1}{N} \sum_{n=1}^N (z_n - \langle z \rangle)^2 \right)^{1/2}$ of each map is calculated and summarized in Fig. 3(b). The rms values are in a narrow band around 0.24 nm ($< \text{monolayer}$), consistent with the small layer thickness variations from Fig. 2(d) if we reasonably assume two uncorrelated interfaces. There is no significant difference between direct GeSi-to-Ge and reverse transition interfaces. The interfaces appear morphologically smooth without features like terraces or islands. However, the recurring pattern in Fig. 3(b) of low

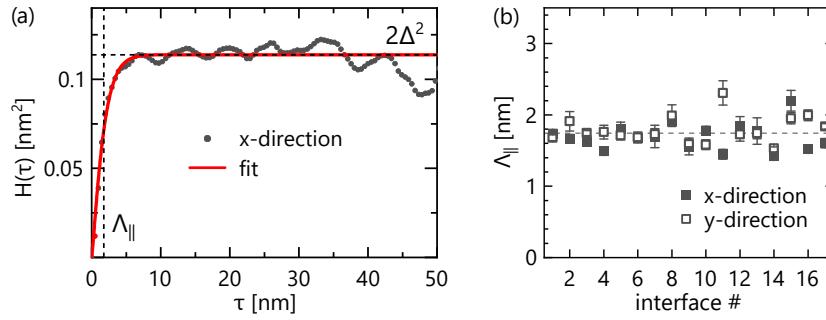


Fig. 4. (a) The 1D height-height correlation function $H(\tau)$ of interface 13 in the x -direction for a (50×50) nm² area, cf. Fig. 3(a). A macroscopic roughness parameter $\Delta (\simeq \Delta_{\text{rms}})$ and the in-plane correlation length Λ_{\parallel} are estimated with a fit. (b) The correlation lengths Λ_{\parallel} found for all interfaces.

Δ_{rms} values among the modules (except for A) suggests that we are not detecting pure noise, but compositional fluctuations governing the roughness, i.e., the interface alloy disorder (IAD). An ordered Ge-Si compound in an (x, y) plane from the transition region would lead to a smooth iso-concentration surface, while alloy disorder causes vertical changes (Δ_{rms}) in the iso-concentration surface perpendicular to the interface. Starting from an abrupt interface, random diffusion kinetics could trigger intermixing and lead to lateral disorder on both sides, which grows with distance from the initial plane. Since Si diffusion in Ge and Ge diffusion in GeSi differ, the interface position with the least disorder is shifted. Figure 3(c) illustrates this for interface 16. Rms values for several topography maps at different Ge concentrations along the intermixing width show increased IAD towards the layers and a shifted minimum to higher Ge content. This generally implies increasing IAD with lower concentration differences. In Fig. 3(b), this probably explains the systematically slightly larger rms values at the thin GeSi barrier (red and blue) compared to the outer module interfaces (green and yellow). Since the thin barriers represent only a small Si reservoir and both Ge QWs must share it, little Si can diffuse across the barrier interfaces, leading to increased IAD.

To determine the in-plane correlation length Λ_{\parallel} of an interface, which is indispensable to describe the morphology, the one-dimensional height-height correlation function $H_x(\tau) = \langle [z(x, \tau) - z(x)]^2 \rangle$ is calculated with the height z at position x and the distance τ between two interface points, see e.g. Fig. 4(a). A fit can be used to determine Λ_{\parallel} as a fit parameter. Figure 4(b) shows the results for all interfaces in x - and y -direction. The correlation lengths are almost constant and very small with about 1.8 nm, which is consistent with the interpretation of IAD significantly ruling the roughness. Due to the random diffusion process and the significant impact of even one Si atom difference between neighbouring unit cells in the Ge/Ge_{0.8}Si_{0.2} system, the formation of larger compositionally correlated regions in-plane is hindered.

Our ET study provides a detailed 3D image of a Ge/GeSi multi-QW structure, revealing interface alloy disorder as the primary cause of interface roughness.

Atomic structures and interfacial engineering of ultrathin indium intercalated between graphene and SiC substrate

V. D. Pham, C. Dong^{1,2}, J. A. Robinson^{1,2}

Crystalline, atomically thin metals stabilized at the interface between epitaxial graphene (EG) and SiC substrate exhibit remarkable physical properties owing to distinct dimensionality and dominant quantum size effects. For example, newly emerging superconductivity in Ga and Ca and semiconducting behaviors in Au, Ag, Ga, In and large nonlinear optical responses in Ga and In which do not occur in their bulk counterparts have been recently demonstrated. Together with 2D van de Waals materials, these heteroepitaxially confined 2D metals are considered as compelling material platforms for quantum and optoelectronic technologies and for exploration of new physical effects. Despite the advanced potentials and functionalities to be expected, the nanoscale picture of the ultrathin metals within the EG/SiC interface that represents their ultimate two-dimensional limit has not been well captured. In this work, we investigate the atomic and electronic structures and the interfacial engineering of the 2D indium using a cryogenic STM system. Here, we utilize partial-buffer EG consisting of sub-monolayer EG and graphene buffer layer (GBL) to enable the intercalation of In. This sample preparation reduces the surface roughness following In intercalation.

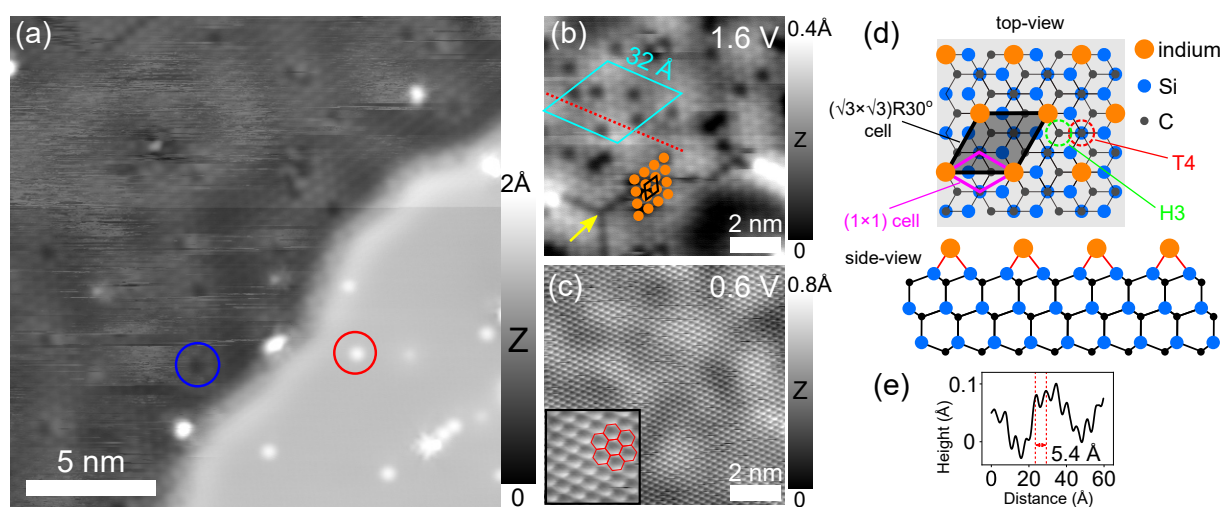


Fig. 1. Pham *et al.*, *Nanoscale Adv.*, 2023, Accepted Manuscript. (a) STM topography image ($V = 2$ V, $I = 50$ pA) showing atomically-resolved structure for In layer in the low intercalated region (left area). In contrast, on the higher layer area, no periodic structure is resolved. (b) Zoomed-in STM topography image ($V = 1.6$ V, $I = 30$ pA) on an area of the low region. Atomic resolution of the In atoms in the low region is clearly shown. The black rhombus indicates the In unit cell (5.4 Å). Cyan rhombus indicates a supercell commensurating to (13×13) times unit cell of graphene. (c) Same area in (b) ($V = 0.6$ V, $I = 30$ pA) imaged at low bias voltage showing only atomic structure of the graphene top layer. (d) Top and side view of the In structure in the low region with respect to the SiC substrate. (e) Height profile across the In structure.

¹Department of Materials Science and Engineering, The Pennsylvania State University, University Park, PA, USA

²2-Dimensional Crystal Consortium, The Pennsylvania State University, University Park, PA, USA

Figure 1(a) shows a typical STM image obtained at 2 V with two distinct atomic phases of In. The details of the low region are further shown in Fig. 1 (b). The high resolution STM image obtained at 1.6 V from a zoomed-in low area reveals an array of bright dots with an average diameter of 3.1 Å which are attributed to individual In atoms. These atoms are arranged in a triangular lattice structure resembling a fcc (111) plane with an atom-to-atom distance of 5.4 Å reflecting the size of its unit cell as indicated by the black rhombus. In contrary, when imaging this area at 0.6 V, only atomic resolution of graphene honeycomb lattice is displayed (Fig. 1 (c)) clearly demonstrating that the ultrathin In is lying below the graphene capping layer. The unit cell of 6H-SiC (0001) is known to be 3.08 Å while the In unit cell found here is 5.4 Å, thus commensurating with the $(\sqrt{3}\times\sqrt{3})R30$ cell of the SiC substrate (that is $\sqrt{3} \times 3.08 = 5.33$ Å). In such case, each In atom must bind to either Si, C (T4) or hollow (H3) sites of the SiC topmost layer as demonstrated in Fig. 1 (d). We tentatively attribute that each In atom sits above the T4 site as it is known to be energetically more favorable. Co-existing with the atomic structure of the In layer, a large superstructure is visible as faint corrugation lines indicated by cyan rhombus in Fig. 1 (b) arising as a result of the lattice mismatch between monolayer graphene and the underlying In layer. This supercell coincides with the (13×13) graphene unit cell emerging from the superposition induced by the two atomic planes between monolayer EG and monolayer In.

Bias-dependent imaging is unable to verify the structure of high In intercalated regions which is hypothesized to be composed of more than one metallic layer preventing individual atoms to be resolved. In Fig. 2 (a) we show a zoomed-in STM image obtained from a smaller area which appears highly flat at 2 V. Apart from this aspect, different point defects are clearly imaged because they have a considerably different electronic density as compared to that of the In atoms. As clearly seen, the bright point defects on the high intercalated region are visible at 2 V as round protrusions. When the bias polarity is switched from 2 V to -2 V, they appear as dark cavities as shown in Fig. 2 (b). The positions of these bright protrusions fully commensurate with the dark cavities except few bright triangular defects belong to graphene. The bias-dependent contrast of the defects shown here is consistent with the previous observation and can be attributed to vacancies in a bilayer In below graphene. Differential (dI/dV) spectroscopy is further used to elucidate the electronic signatures of the defects in 2D indium. Fig. 2 (d) presents different dI/dV spectra obtained with the tip placed above six defects marked from 1 to 6 in Fig. 2 (e) which is an enlarged area from the yellow square in Fig. 2 (a). The spectra taken above these defects mainly exhibit three unoccupied states as indicated by black arrows, while the reference spectrum (black curve) taken at a clean surface area marked with black cross does not show any pronounced resonance in this energy range. This is further confirmed in the series of STM topography images shown in Fig. 2 (e-j) taken at the bias voltages corresponding

to the resonance peaks from the dI/dV spectra.

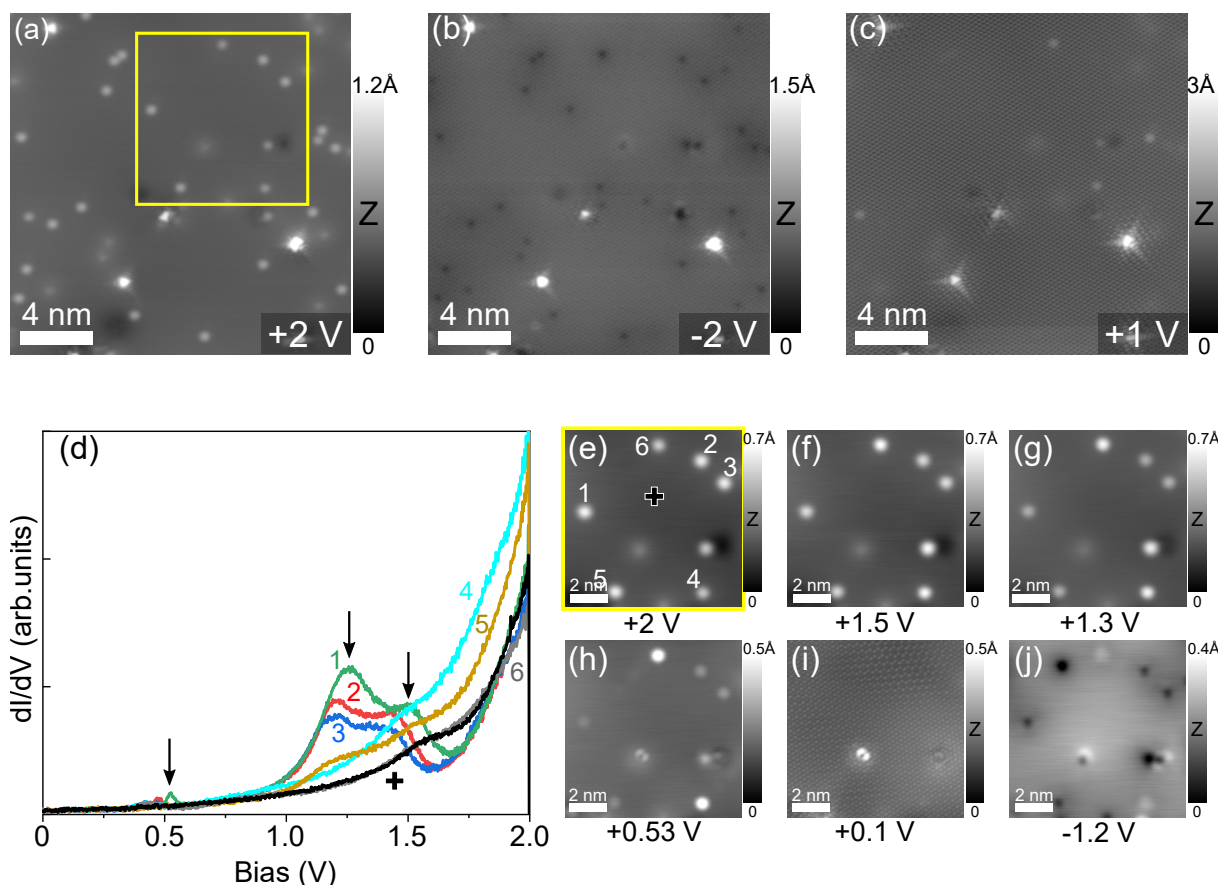


Fig. 2. Pham *et al.*, *Nanoscale Adv.*, 2023, Accepted Manuscript. (a-c) STM topography image of the same area on the high intercalated region at different bias voltages: 2 V, -2 V and 1 V, respectively (tunneling current: $I = 100$ pA). The atomic resolution of In atoms is not resolved here, only intrinsic point defects are visible as bright protrusions, dark cavities at different bias voltages. Triangular defects belong to the graphene coverlayer. (d) dI/dV spectra measured on six defects marked from 1 to 6 indicated in (e). The black spectrum is probed on a clean surface region indicated by black cross in (e). (e-j) Bias-dependent STM topography images obtained from the area indicated as yellow square in (a).

We further used tip-induced surface manipulation to directly visualize and engineer the In layers at the EG/SiC interface (as described in Fig. 3 (a)). Figure 3(b) shows the initial area (which is the same area in Fig. 1 (b) of the low intercalated region) where we placed the STM tip at a fixed position above the surface. Two positive bias voltage pulses of 4 V and 5 V were consecutively applied as indicated as green and orange crosses in Fig. 3 (c) and (d). As the result of the tip voltage pulses, the deep areas appear as holes are formed. The periodicity of 18 \AA (indicated by the white rhombus) in Fig. 3 (d) exhibits only clean EG on SiC without intercalation which is further confirmed by the magnified STM image at low bias voltage (0.02 V) shown in Figure 3 (h). The periodicity of 18 \AA corresponds to typical moiré pattern of the $6\sqrt{3}\times 6\sqrt{3}$ reconstruction of the underlying SiC. This shows an important indication that the area inside the hole is deintercalated and is composed of only EG/SiC without intercalated In atoms (hereafter mentioned as $\sqrt{3}\times\sqrt{3}$ graphene). Based on this observation, we conclude that

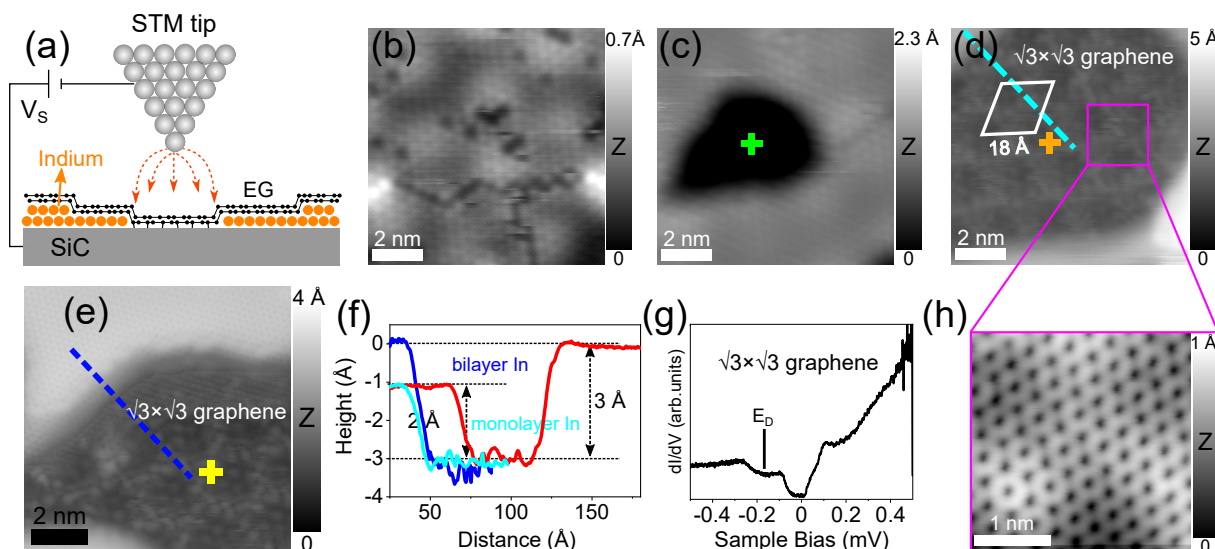


Fig. 3. **Pham *et al.*, *Nanoscale Adv.*, 2023, Accepted Manuscript.** (a) Sketching of STM tip manipulation to deintercalate the In atoms below graphene. (b-d) STM topography images ($V = 1.6$ V, $I = 30$ pA) of a low intercalated location before (b) and after (c-d) two voltage pulses of 4 V and 5 V are applied. The green and orange crosses indicate the tip positions. The superstructure with a periodicity of 18 Å (white rhombus) typical for a $\sqrt{6}\times\sqrt{6}$ reconstruction of SiC (referred as $\sqrt{3}\times\sqrt{3}$ graphene) indicates that only EG/SiC without intercalated In atoms is in the deintercalated region. (e) STM topography image ($V = -1$ V, $I = 100$ pA) of a high intercalated area after deintercalation. (f) Height profiles along the cyan and blue curves indicated in (d) and (e) typically for low and high region thicknesses. (g) Typical dI/dV spectrum obtained on the $\sqrt{3}\times\sqrt{3}$ graphene. (h) Atomic resolution STM image ($V = 0.02$ V, $I = 100$ pA) of $\sqrt{3}\times\sqrt{3}$ graphene indicated by purple square in (d).

the voltage pulse has successfully redistributed the intercalated material under EG in the sense that the In atoms are compressed and shifted laterally to the nearby region outside the hole. Tip-induced interface manipulation is a powerful method to directly visualize and investigate the properties of 2D metals below graphene capping layer. Upon deintercalation, the metal thicknesses in the low and high intercalated regions can easily be explored by measuring the height of the atomic steps between the intercalated and deintercalated ($\sqrt{3}\times\sqrt{3}$ graphene) regions. We have systematically investigated the intercalation heights of low and high regions by performing the tip voltage pulse over different locations and obtained their average heights of 2.13 ± 0.25 Å and 3.38 ± 0.33 Å, respectively, and attribute the low and high regions to be composed of monoatomic and bilayer In below graphene.

This investigation allows one to fully capture the microscopic insights of the ultrathin In at the EG/SiC interface. Our results contribute way in exploring the atomic and electronic structure of the confined metal, strongly emphasizing on the tip-induced manipulation as the first demonstration for intercalated metal at EG/SiC interface. In the further steps, we are currently continuing this investigation in which through the voltage pulse we can also control the number of the intercalated In layers with atomic precision.

Creating quantum dots on the InAs(110) cleavage surface by atom manipulation

V. D. Pham, Y. Pan, S. C. Erwin¹, S. Fölsch

Quantum dots are often called “artificial atoms” because they confine electrons to discrete energy levels. This makes them unique objects of study, for example, in electronic quantum transport and optoelectronics or in the exploration of semiconductor qubits and electron correlation in artificial lattices, to mention only a few. Quantum dots are typically created in semiconductor heterostructures by growing aligned nanocrystals, by imposing lateral confinement using electron-beam lithography, or by depleting a two-dimensional electron gas (2DEG) using external gates and local oxidation.

The method of 2DEG depletion using external gates exploits the electric field effect to spatially modulate the carrier density. In our previous work, we followed a similar idea of spatially controlling the electrostatic surface potential, however, at the level of single atoms: we used the tip of a scanning tunneling microscope (STM) to assemble short atomic chains on an InAs(111)A surface by atom manipulation. The chains consisted of six positively charged In adatoms leading to the confinement of surface-state electrons, and hence, the emergence of a bound state with discrete energy – the fingerprint of a quantum dot. These dots can be arranged on the surface and thereby coupled in various ways yielding quasi-molecular electronic states. Here, we extend this concept to the (110) cleavage surface of indium arsenide.

Different to the InAs(111)A surface grown by molecular beam epitaxy, cleaved InAs(110) is free of native In adatoms. Nonetheless, we showed previously that individual In atoms can be transferred one-by-one from the STM tip to the surface after agglomerating indium at the tip apex (by repeated voltage pulsing at a remote surface location). The left hand-side panel in Fig. 1(a) shows a constant-current topography image of an In adatom adsorbed on the InAs(110) surface. At a sample bias of 0.1 V as used here, the surface As atoms are imaged as protrusions arranged in rows along the $[1\bar{1}0]$ in-plane direction; the spacing between the rows is $a_0 = 6.06 \text{ \AA}$, the cubic lattice constant of InAs. The adatom in the center of the image is located in the channel in between of the rows, consistent with previous theoretical work predicting interstitial configurations in which the adatom is bonded either to two cations and one anion (labeled I_{11}) or to two anions and one cation (I_{12}). Our density functional theory (DFT) calculations reveal that I_{12} is the most stable configuration, as illustrated by the right hand-side panel showing a close-up view together with an overlaid structure model.

Figure 1(b) shows the DFT potential-energy surface for an In adatom diffusing on the InAs(110) cleavage surface and provides quantitative information on the adsorption behavior: the metastable configuration I_{11} is 0.2 eV higher in energy than the stable

¹Center for Computational Materials Science, Naval Research Laboratory, Washington DC, USA.

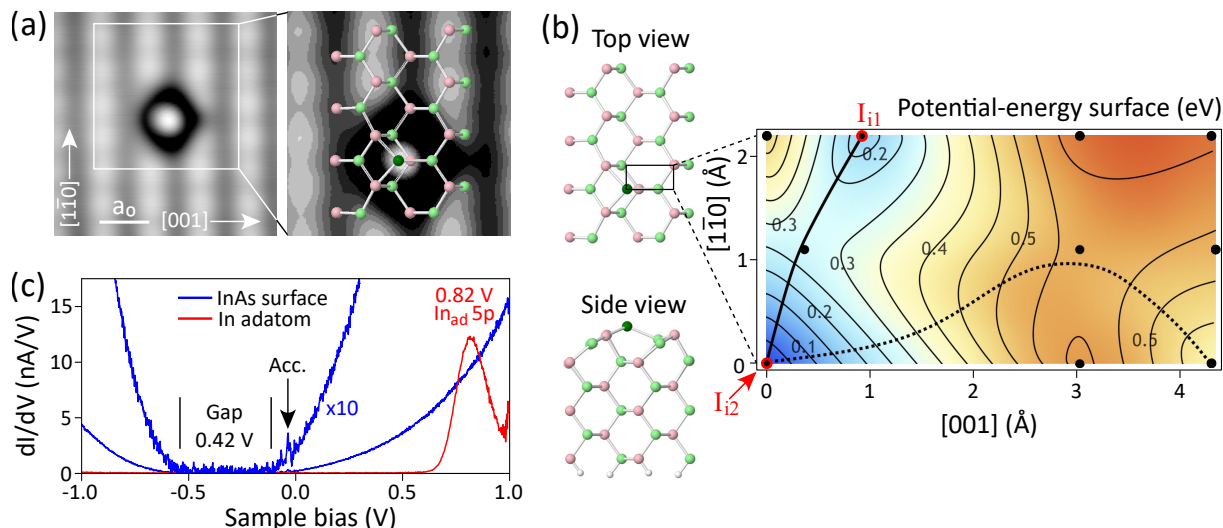


Fig. 1. (a) Left: STM image (1 nA, -0.6 V) of an In adatom on InAs(110) located within the channel between rows of surface As atoms imaged as protrusions, row spacing $a_0 = 6.06$ Å. Right: close-up view at staggered gray scale with overlaid structure model showing the surface In (green) and As atoms (pink) plus the In adatom (dark green). (b) Left: structural model in top and side view as determined by DFT. Right: DFT potential-energy surface for an In adatom diffusing on InAs(110); the solid line shows the minimum energy path between the stable (I_2) and metastable (I_1) configurations along the channel whereas the dotted line indicates the barrier across the channel. (c) Conductance spectra recorded with the tip probing the bare surface (blue) and a discrete In adatom (red). The blue spectrum indicates Fermi level pinning in the conduction band (CB) and accumulation-layer states (arrow) near the CB minimum; the red spectrum reveals an unoccupied state at ~ 0.8 eV deriving from $5p$ atomic orbital states according to DFT.

configuration I_2 . The diffusion barrier along the channel is 0.3 eV (the minimum energy path is sketched as a solid curve); this barrier can be overcome above ~ 120 K. On the other hand, the barrier across the channel is about 0.6 eV (dotted curve) and can be overcome above ~ 240 K. However, this pathway is probably preempted by exchange between the adatom and a surface In atom, similar to the exchange reaction previously reported for Mn substitutional impurities on InAs(110).

We probed the electronic surface properties by scanning tunneling spectroscopy (STS) measurements of the tunnel conductance dI/dV which provides an approximate measure of the electronic density of states. The blue spectrum in Fig. 1(c) was recorded with the tip probing the bare surface. It reveals the expected energy band gap of InAs (0.42 eV at the measurement temperature of 5 K) and, most prominently, Fermi level pinning in the conduction band. The latter is a generic feature of InAs surfaces indicating electron accumulation at the surface. In agreement with previous STS work on cleaved InAs(110), we frequently observe conductance peaks near the conduction band minimum right below the Fermi level (at sample bias $V = 0$). We interpret these peaks as a manifestation of conduction band states that undergo vertical confinement because of the downward band bending near the surface. Accordingly, the blue spectrum in Fig. 1(c) reveals a small peak at -35 mV marked by an arrow. The actual energy and magnitude of the peaks observed depends on the location probed by the tip. We attribute this spatial variation to the effect of electrostatic disorder due to residual defects in the surface-near region.

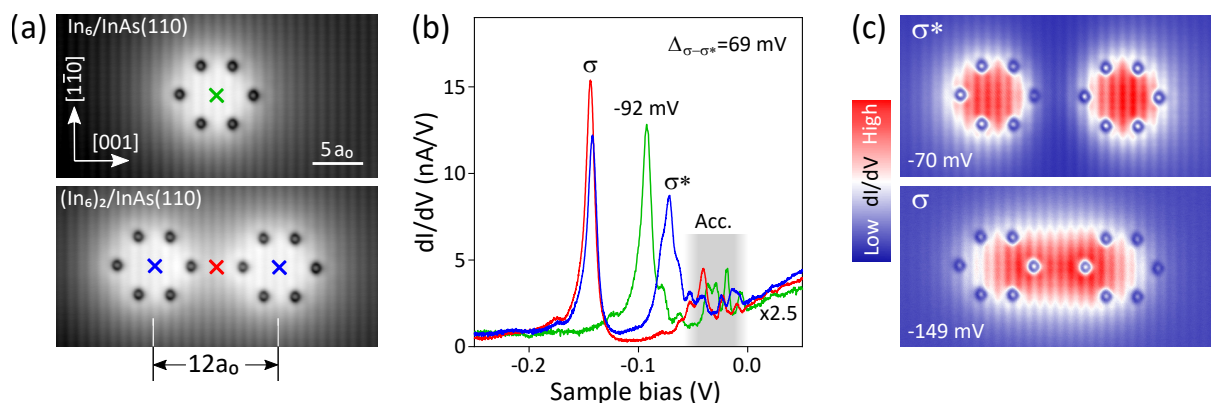


Fig. 2. (a) Upper panel: STM image (0.1 nA, 0.1 V) of a dot consisting of six In adatoms. Lower panel: same as (a) after adding an identical dot at a center-to-center distance of $12a_0 = 72.72 \text{ \AA}$ along the [001] direction. (b) Conductance spectra taken at the respective tip positions marked by colored crosses in (a). The bound state of the discrete dot is at -92 mV (green curve) while a bonding (σ) and an antibonding state (σ^*) are observed for the dimer (see spectral curves in red and blue, the latter is an average of equivalent spectra taken at the center of either dot in the dimer, respectively); accumulation-layer states are highlighted by the grey-shaded area. (c) Spatial conductance maps recorded at the sample biases where the σ and σ^* states are observed in (b), corroborating bonding (lower map) and antibonding character (upper map).

The spectrum shown by the red curve in Fig. 1(c) was recorded with the tip probing an In adatom on InAs(110). It reveals a pronounced state at $\sim 0.8 \text{ eV}$ deriving predominantly from $5p$ atomic orbital states of the adatom according to our DFT calculations. A similar adatom-derived state was reported previously for In adatoms on InAs(111)A and GaSb(110). A further similarity to the InAs(111)A system is that In adatoms on InAs(110) are positively charged. In the STM experiment, this becomes obvious from the increased apparent height around the adatom when imaged at positive sample bias. The increased height is due to the screened Coulomb potential of the charged adatom which locally increases the density of states available for the tunneling process. Complementary DFT calculations of the electrostatic potential above the surface confirm that the In adatom transfers electronic charge to the substrate, giving it a positive charge and hence making it attractive for electrons.

An adatom dropped from the tip can be subsequently repositioned along the surface channel by means of force interaction with the STM tip (lateral atom manipulation). This method was used in the upper panel of Fig. 2(a) to assemble six In adatoms into a hexagon having a width of $7a_0 = 42.42 \text{ \AA}$ along the [001] direction and $8a_0/\sqrt{2} = 34.28 \text{ \AA}$ along the $[\bar{1}10]$ direction. The electrostatic potential induced by the six positively charged adatoms confines electrons at the surface, similar to our previous observations for linear adatom chains on InAs(111)A. The confinement is evident from the green spectrum in Fig. 2(b) showing the emergence of a strong conductance peak at -92 mV when placing the probe tip at the center position. Hence, the hexagon acts as a quantum dot – an “artificial atom” – that creates a bound state of discrete energy.

Finally, it is shown that the quantum coupling between dots arranged on InAs(110)

allows one to create quasi-molecular electronic states: adding an identical dot at a center-to-center spacing of $12a_0 = 72.72 \text{ \AA}$ along the [001] direction yields the quantum-dot dimer shown in the lower panel of Fig. 2(a). The corresponding spectra recorded with the tip above (blue) and in between of the dots (red) reveal the emergence of a bonding (σ) and an antibonding state (σ^*) with a splitting of $\Delta_{\sigma-\sigma^*} = 69 \text{ mV}$. Note also that the $\sigma - \sigma^*$ doublet is downshifted from the energy of the single dot; this shift arises from the electrostatic potential change that each dot experiences from the other as we have previously observed in quantum-dot dimers on InAs(111)A. The symmetric (σ) and antisymmetric (σ^*) wave-function character of the bonding and antibonding states is evident from the spatial conductance maps in Fig. 2(c) recorded at the corresponding bias voltages of the σ and σ^* peaks in panel (b), respectively.

It remains to be shown what kind of electronic states are actually confined by the quantum dots described in this contribution. Our ongoing work will clarify if intrinsic surface states are responsible for the present observations [as on the InAs(111)A surface] or if accumulation-layer states undergo additional, lateral confinement. From the applied point of view, the InAs(110) system presented here has the advantage that large-scale and atomically flat surface terraces are readily prepared by cleavage in ultrahigh vacuum and no extra deposition of material is required to generate charged adatoms, making it an attractive platform for the creation of semiconductor quantum structures by scanning-probe techniques. In addition, this crystallographic surface orientation allows for the cross-sectional investigation of III-V semiconductor heterostructures, offering the long-term prospect to combine the capabilities of STM-based atom manipulation with lateral transport measurements.

Excitonic and deep-level emission from N- and Al-polar homoepitaxial AlN layers grown by molecular beam epitaxy

L. van Deurzen,¹ J. Singhal,¹ J. Encomendero,¹ D. Jena,¹ O. Brandt, J. Lähnemann

The ultra-wide gap semiconductor AlN was first synthesized over a century ago, but its potential lay dormant until very recently, when researchers succeeded in synthesizing large AlN crystals of high structural perfection with low dislocation densities ($< 10^4$ – 10^6 cm⁻²). The availability of AlN substrates has allowed the synthesis of homoepitaxial layers with very high crystal quality, enabling detailed studies of the fundamental optical properties of AlN, particularly the valence-band order and corresponding exciton symmetries. So far, researchers have exclusively used metal-organic vapor phase epitaxy (MOVPE) for the fabrication of this homoepitaxial material, while molecular beam epitaxy (MBE) has not yet been utilized. Furthermore, while Al-polar AlN(0001) layers have been investigated by several groups, studies of N-polar AlN(000 $\bar{1}$) are still lacking, although this orientation with its reversed direction of the polarization fields can be advantageous for the design of both UV light emitting diodes and high electron mobility transistors. In the present work, we aim to fill these gaps by using cathodoluminescence (CL) spectroscopy to analyze and compare the emission of N- and Al-polar homoepitaxial, strain-free AlN layers grown by MBE.

The three samples under investigation were grown by MBE using a radio-frequency plasma source for generating active N and a solid-source effusion cell for Al. As substrates, we used bulk AlN wafers grown by physical vapor transport with a dislocation density $< 10^4$ cm⁻². The layers were grown at substrate temperatures above 1000 °C under Al-stable conditions. Samples I and II consist of a 700-nm-thick Al-polar and a 900-nm-thick N-polar layer, respectively. Sample III consists of a 1- μ m-thick N-polar AlN layer that was capped with 6.7 nm heteroepitaxial GaN. This GaN cap layer serves as a passivation layer for the AlN surface and also acts as a charge-spreading layer during electron beam excitation. As reference and for comparison with other studies, a freestanding AlN substrate was used. Regardless of polarity, the layers exhibit atomically smooth surfaces, high structural perfection and high purity (not shown).

CL spectra of samples I and II are compared with the one of the bare PVT-AlN substrate (N-polar face) in Fig. 1. An acceleration voltage of 7 keV was used to excite the samples, ensuring that electron-hole pairs are generated only within the homoepitaxial layers. Figure 1(a) shows the low-temperature, high-resolution near-bandedge emission spectra normalized to their peak intensities. For all three samples, a distinct high-energy line is observed at (6.038 ± 0.005) eV, with the error due to the uncertainty of the wavelength calibration. This transition energy is close to the average literature

¹Cornell University, School of Applied and Engineering Physics, Ithaca, New York, USA

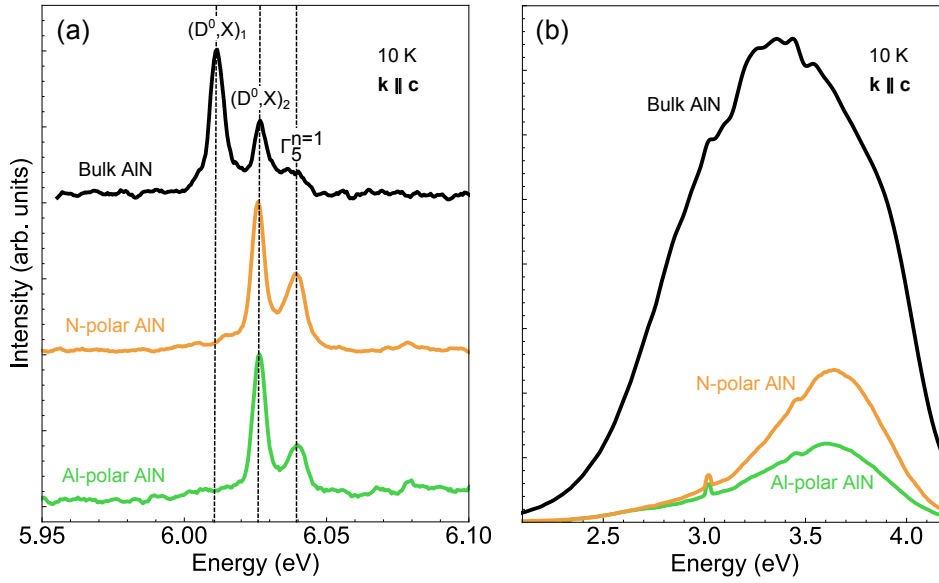


Figure 1: (a) High-resolution near-bandedge and (b) deep-level CL spectra for the bare PVT-AIN substrate, as well as samples I and II. Light was collected with $\mathbf{k} \parallel \mathbf{c}$. The narrow feature just above 3 eV in (b) is the second order of the near-bandedge emission.

value (6.041 eV) for the exciton spin triplet with Γ_5 symmetry in bulk (strain-free) AlN.

For AlN, the negative crystal-field splitting causes the Γ_{7+}^v band to be the uppermost valence band, resulting in exciton states of $\Gamma_7^c \otimes \Gamma_{7+}^v$ symmetry (often referred to as A-excitons). Spin-exchange interaction splits these states into excitons with the irreducible representation $\Gamma_1 \oplus \Gamma_2 \oplus \Gamma_5$, with the Γ_5 spin triplet being the only optically active state that satisfies $\mathbf{E} \perp \mathbf{c}$ and $\mathbf{k} \parallel \mathbf{c}$, i. e., our measurement geometry.

For the PVT substrate, two intense and narrow lines are observed 28 and 13 meV below the $\Gamma_5^{n=1}$ free exciton ground state, the former being absent for both samples I and II. These lines are commonly attributed to donor-bound exciton transitions [e. g., Feneberg *et al.*, Phys. Rev. B **82**, 075208 (2010)]. The $(D^0, X)_1$ line with 28 meV binding energy has been tentatively assigned to either O or Si, while the $(D^0, X)_2$ line with 13 meV binding energy has been speculated to be related to a native shallow donor. While the $(D^0, X)_1$ line dominates the substrate spectra, its total absence in our epitaxial layers implies a significantly lower concentration of the responsible shallow donor in the layers compared to the substrate. Secondary ion mass spectrometry data (not shown) of our samples are consistent with Si (and not O) being the donor related to the $(D^0, X)_1$ line.

To probe radiative deep levels, we performed CL measurements with lower resolution in the range of 2–4.2 eV as shown in Fig. 1(b). All spectra in this figure are normalized to their respective near-bandedge peak intensities. The integrated intensity of the broad luminescence bands observed in this spectral range exceeds the near-bandedge intensity by a factor 2.5 for the bulk AlN substrate, but is lower by factors of 0.5 and 0.8 for samples I and II, respectively. Apart from the higher intensity, the CL band from the substrate is much broader and seems to consist of two individual contributions, with the one at higher energy matching the energy of the band in samples I and II. The lineshape of samples I and II are almost identical, suggesting that similar types of

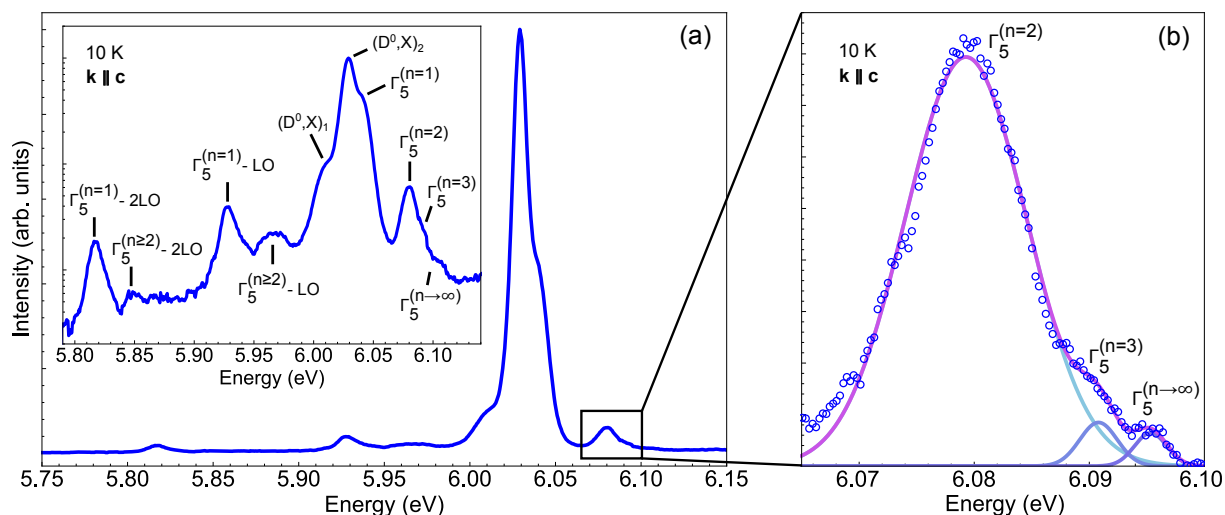


Fig. 2. (a) Low-temperature, high-resolution near-bandedge CL spectrum for sample III on a linear and logarithmic (inset) intensity scale. The integration time was chosen to be $10\times$ longer than for the spectra in Fig. 1(b). (b) Expanded view of the excited free exciton transitions, with $\Gamma_5^{n=2}$, $\Gamma_5^{n=3}$, and $\Gamma_5^{n\rightarrow\infty}$ resolved. The line is a fit of the data with three Gaussians (also shown).

defects are incorporated for both polarities.

The overall similarity between the radiative properties of the Al- and N-polar AlN samples is remarkable. In contrast, studies on N-polar GaN layers, regardless of whether being grown by MBE or MOVPE, have shown that it is difficult to obtain layers with a purity and emission characteristics equivalent to their Ga-polar counterparts. A higher sticking coefficient of impurities as well as a lower formation energy for N vacancies in N-polar GaN growth are discussed as possible reasons for this difference in material quality. For AlN, our data shows that the situation is much more favorable.

For further details of the near-bandedge emission, we turn to sample III, which exhibits the highest emission intensity of all samples. Figure 2(a) shows its low-temperature CL spectrum for an acceleration voltage of 11 keV. The higher energy ensures a high signal intensity, facilitating the reliable detection of weak transitions. As seen best in the inset, ten transitions are resolved. The highest energy transitions associated to excited states of the free exciton are highlighted in the magnified view displayed in Fig. 2(b). Where available, our values are in good agreement with previous studies. In particular, the $E(\Gamma_5^{n=1})$ exciton and its excited states are resolved at 6.038, 6.079, 6.091, and 6.095 eV. Again, the $(D^0, X)_2$ transition and a weak $(D^0, X)_1$ line (originating from the substrate) contribute to the spectra as well. The prominent transition at 6.079 eV can be readily assigned to the $E(\Gamma_5^{n=2})$ transition, for which energy separations of 37–43 meV with respect to the $E(\Gamma_5^{n=1})$ transition have been reported in the literature, while no values were previously available for the higher-order transitions.

To confirm the assignment of the transitions at 6.091 and 6.095 eV to higher excited states, we consider the hydrogenic effective-mass approximation, in which the energies of the excited states as well as the binding energy of the free exciton can be determined based on the 1S-2S splitting. Indeed, the predicted values of 6.087 and 6.093 eV for the

$\Gamma_5^{n=3}$ and $\Gamma_5^{n \rightarrow \infty}$ transitions, respectively, are only slightly lower than the experimentally observed transition energies. Despite shortcomings of this simplistic model, the agreement is not improved by considering the anisotropy of AlN regarding both the reduced exciton mass μ and the relative static permittivity ϵ as well as the exchange and electron-phonon interactions and a true theoretical treatment would have to be even more complex. Other experimental values for the free exciton binding energy reported in the literature range from 47 to 67 meV, with the average being about 54 meV. We additionally resolve two longitudinal optical (LO) phonon replicas each for the free exciton state and for the excited states. In Fig. 2(a), the LO phonon replicas are denoted as $\Gamma_5 - m\text{LO}$ with $m \in \{1, 2\}$. The energy spacing between the phonon replicas and the main peaks is a multiple of 112 meV, in close agreement with existing literature.

To explain the prominence of excited exciton states in our CL experiments, we have to consider the excitation conditions. Given the strong Coulomb interaction in AlN, it may appear surprising to see recombination from free carriers at a nominal temperature of 10 K. The fraction of excitons at a given temperature is governed by Saha's law and is predicted to decrease with increasing carrier temperature and to increase with increasing electron-hole density below the Mott transition. In most previous works, the samples were excited with an ArF laser, which delivers intense ns pulses with a low repetition rate and an energy close to the band edge. Due to the low repetition rate, the lowest excitation densities are typically around 50 kW/cm^2 , resulting in a carrier density on the order of $5 \times 10^{17} \text{ cm}^{-3}$. However, the excess energy delivered per pulse is comparatively low. For our CL experiments, the situation is opposite. The continuous-wave excitation by the electron beam facilitates a comparatively low excitation density. We estimate a carrier density of not more than $4 \times 10^{16} \text{ cm}^{-3}$ for an acceleration voltage of 11 kV. The carrier temperature, however, is typically rather high, since the electron beam creates highly energetic secondary electrons and holes. The cooling of these hot carriers proceeds via the emission of LO phonons, thus creating a nonequilibrium population of hot LO phonons that in turn heats the carrier distribution by strongly increasing the probability of LO phonon absorption. Indeed, from the high-energy slope of the $\Gamma_5^{(n=1)} - 2\text{LO}$ transition, we deduce a carrier temperature of 120 K. With this carrier temperature and excitation density, Saha's law predicts an excitonic fraction of only 0.82, while for the carrier density estimated for ArF excitation, the fraction increases to 0.95 even for the same carrier temperature.

We have shown that MBE-grown AlN of both polarities features intense free exciton emission and suppressed emission from bound excitons and deep-level defects, which highlights the potential of MBE for the growth of UV emitters. The ability to grow N-polar samples and thus to flip the orientation of the polarization fields without compromising the crystal quality provides an additional degree of freedom for the design of devices.

Top-down (In,Ga)N nanowires fabricated from molecular beam epitaxial layers with high structural perfection

J. Kang, M. Gómez Ruiz, D.V. Dinh, A. Campbell, A. Trampert, M. Oliva, P. John, J. Lähnemann, T. Auzelle, O. Brandt, and L. Geelhaar

(In,Ga)N nanowires are attractive as semiconductor electrode and light absorber for photoelectrochemical applications such as solar water splitting and CO₂ reduction because the energies of the band edges are favorably positioned with respect to the relevant redox potentials, the light absorption can be enhanced compared to planar layers, and the large surface-to-volume ratio enables a high loading with catalysts for the electrochemical reactions. For the synthesis of such nanowires, a top-down approach is attractive because composition and doping can be controlled during the initial epitaxial growth of a planar layer, and the nanowire morphology independently during the subsequent structuring. However, an (In,Ga)N layer has to be grown with a thickness corresponding to the desired nanowire length. This is difficult because there are no suitable lattice-matched substrates for (In,Ga)N. In this study, we demonstrate the growth of 500-nm-thick In_{0.12}Ga_{0.88}N layers with high structural perfection on GaN templates, followed by top-down nanowire fabrication based on metal dewetting.

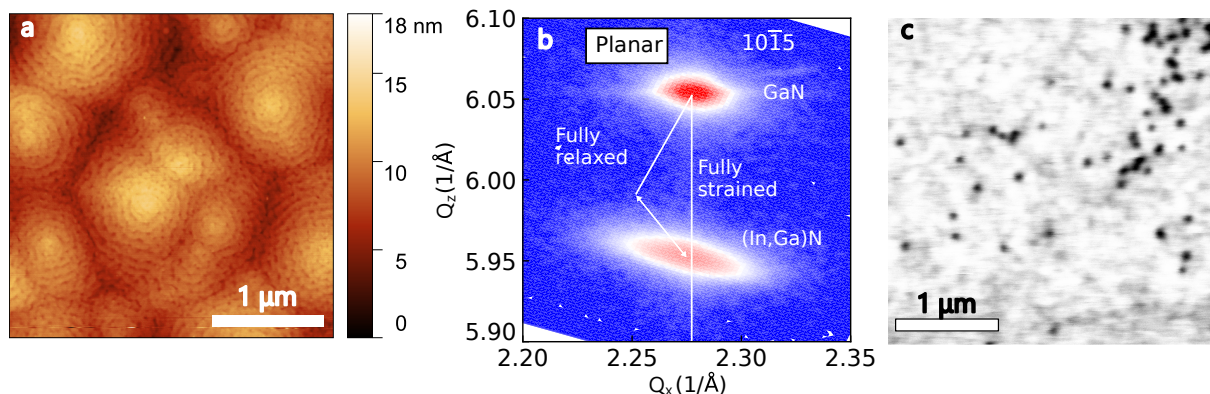


Fig. 1. Structural characterization of a 500-nm thick In_{0.12}Ga_{0.88}N layer grown by PA-MBE on a GaN template. (a) AFM topograph. (b) RSM around the 10 $\bar{1}5$ Bragg reflection revealing an In content of 12% and a strain relaxation degree of 10%. (c) CL intensity map for the wavelength range 398–420 nm acquired at 10 K. The dark spots correspond to TDs.

(In,Ga)N layers with a thickness of 500 nm were grown using plasma-assisted molecular beam epitaxy (PA-MBE) on commercial GaN(0001) templates at a substrate temperature of 620 °C. The growth is aided by two techniques for in-situ monitoring, reflection high-energy electron diffraction and line-of-sight quadrupole mass spectrometry. Substrate temperature and impinging fluxes are adjusted such that a dynamic balance between the impinging and desorbing In flux is achieved to induce the formation of an In adlayer on the growth front.

The patterning needed for top-down nanowire fabrication was based on the dewetting of a metal film, *i. e.* a simple and scalable approach. An In_{0.12}Ga_{0.88}N layer was

covered with a 220-nm-thick SiO_x layer and a 5-nm Pt film. Next, the sample was annealed at 800 °C for 1 hour in an Ar atmosphere. During this process, the Pt film breaks up into nanoislands that serve as mask for the nanowire fabrication. We note that the size, shape, and density of the nanoislands depend on the initial thickness of the Pt film and the annealing conditions, allowing a tuning of the nanowire ensemble morphology. After annealing, the $\text{In}_{0.12}\text{Ga}_{0.88}\text{N}$ layer was structured into nanowires by a sequence of reactive ion etching, inductively coupled plasma reactive ion etching, and KOH wet etching.

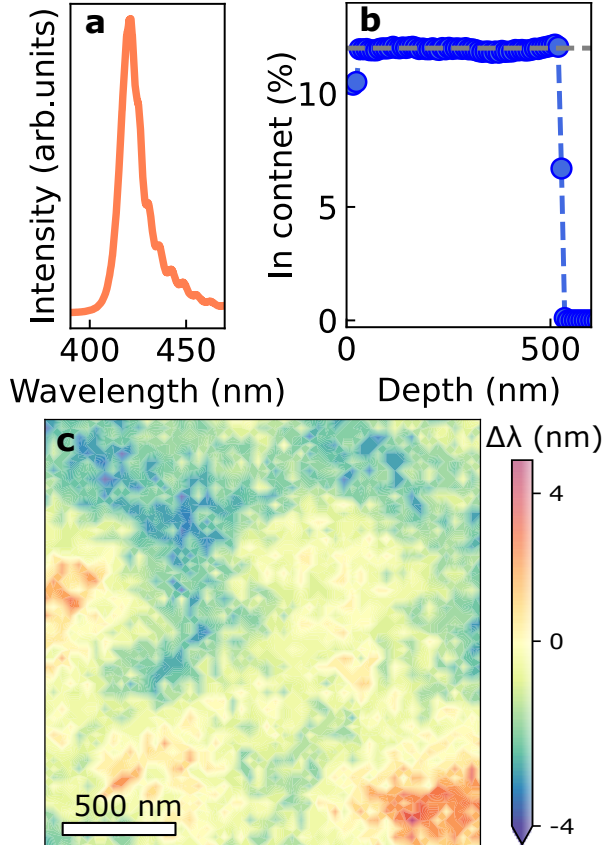


Fig. 2. Further measurement results for the same $\text{In}_{0.12}\text{Ga}_{0.88}\text{N}$ layer characterized for the data in Fig. 1. (a) PL spectrum measured at room temperature. (b) In content depth profile obtained by SIMS. (c) Room temperature map of the CL peak emission wavelength variation.

the cathodoluminescence (CL) intensity was mapped as depicted in Fig. 1(c). Besides minor fluctuations across the surface, there is a number of dark spots indicating positions of essentially zero CL intensity that are associated with TDs. Averaging over different locations on the layer, we found a TD density of $\approx 1 \times 10^9 \text{ cm}^{-2}$. This value was confirmed by transmission electron microscopy measurements (not shown). Furthermore, the value is on the lower end compared to literature, which is consistent with the low strain relaxation degree deduced from the RSM in Fig. 1(b).

The photoluminescence (PL) spectrum for the $\text{In}_{0.12}\text{Ga}_{0.88}\text{N}$ layer under investigation is presented in Fig. 2(a). The spectrum consists of a single emission band that

The topograph in Fig. 1(a) shows the typical spiral pattern that is characteristic for GaN grown by PAMBE. For the present layer, the monolayer spiral growth around screw threading dislocations is well resolved and results in a root-mean-square roughness of 1.9 nm over a scanning area of $3 \times 3 \mu\text{m}^2$. X-ray diffraction (XRD) reciprocal space maps (RSM) were acquired to determine independently the In content and strain relaxation degree of the (In,Ga)N layers. The RSM in Fig. 1(b) reveals for this layer an In content of 12% and a relaxation degree of only 10%. We aim at minimizing the strain relaxation degree to minimize the density of threading arms of misfit dislocations, which would act as nonradiative recombination centers.

To gain direct insight into the density of threading dislocations (TDs),

peaks at 425 nm. This peak position is consistent with the In content and strain relaxation degree deduced by XRD. The full width at half maximum (FWHM) of the emission band is only 75 meV at room temperature, which is one of the lowest values reported for (In,Ga)N layers with similar thickness and In content. Since the emission wavelength is affected by both composition and strain, the low FWHM of Fig. 2(a) suggests for both properties a high uniformity throughout the layer. We point out that maintaining a constant In content during the growth of thick (In,Ga)N layers is challenging since the gradual relaxation of strain typically fosters increasing In incorporation, a phenomenon called ‘compositional pulling’.

A depth profile of the In content was obtained by secondary-ion mass spectrometry (SIMS), and the result is shown in Fig. 2(b). The In content is constant along the growth direction throughout the entire film. In order to probe the homogeneity in the lateral direction, we acquired maps of the CL peak emission wavelength as depicted in Fig. 2(c). Within this area of size $2 \times 2 \mu\text{m}^2$, the variation of the peak emission wavelength is less than 10 nm, indicating that there are only negligible fluctuations in In content. The combination of PL spectroscopy, SIMS, and CL wavelength mapping demonstrates that our $\text{In}_{0.12}\text{Ga}_{0.88}\text{N}$ layer has a uniform In composition, which is an excellent basis for the subsequent top-down nanowire fabrication.

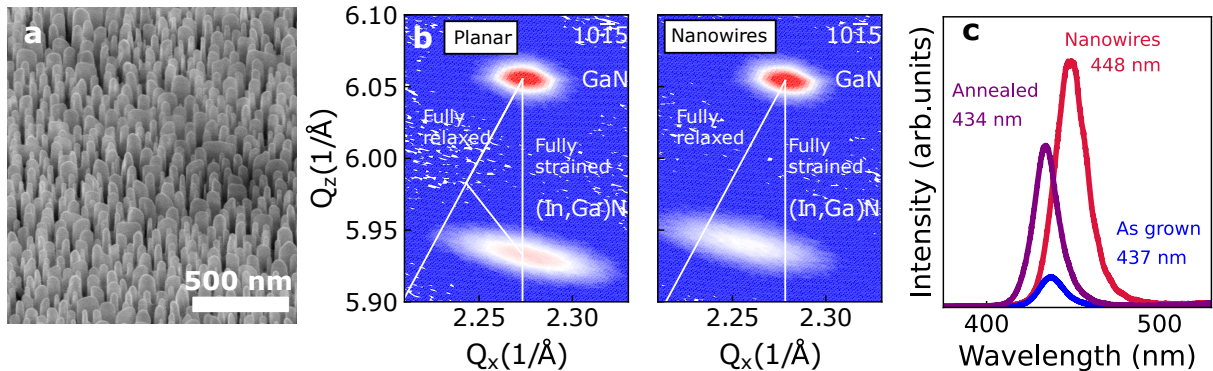


Fig. 3. (a) SE micrograph of a top-down nanowire ensemble from another $\text{In}_{0.12}\text{Ga}_{0.88}\text{N}$ layer. (b) RSMs of this nanowire ensemble (right-hand side) and the corresponding $\text{In}_{0.12}\text{Ga}_{0.88}\text{N}$ layer (left-hand side). (c) Room temperature PL spectra of the as-grown $\text{In}_{0.12}\text{Ga}_{0.88}\text{N}$ layer (blue), the nanowire ensemble (red), and an annealed reference layer (purple).

Figure 3(a) presents a secondary electron (SE) micrograph of the final (In,Ga)N nanowire ensemble. The average nanowire diameter is 45 nm, the number density $1.4 \times 10^{10} \text{ cm}^{-2}$, and the average height 300 nm. The nanowire diameter is significantly smaller than the average distance between TDs. Thus, based on statistics we expect that the majority of nanowires is free of TDs and should thus exhibit a high internal quantum efficiency. Furthermore, compared to a planar structure, in the nanowire geometry strain can be elastically relaxed at the free sidewalls. This effect is illustrated by the RSMs in Fig. 3(b). In the as-grown layer, the (In,Ga)N reflection is positioned vertically below the GaN reflection, indicating that the (In,Ga)N layer is almost fully

strained. We mention that this is a different layer than analyzed extensively above, but the In content and strain relaxation degree are very similar. In the RSM measured after nanowire fabrication, the (In,Ga)N reflection is shifted towards the inclined line indicating fully relaxed (In,Ga)N. This shift demonstrates the elastic strain relaxation occurring during the transition from layer to nanowire structure. That the RSM does not show fully relaxed $\text{In}_{0.12}\text{Ga}_{0.88}\text{N}$ is attributed to the presence of an about 200-nm thick $\text{In}_{0.12}\text{Ga}_{0.88}\text{N}$ layer under the nanowire structure, which is still strained by the lattice mismatch to the GaN template and also probed during the XRD measurement.

PL spectra of both the $\text{In}_{0.12}\text{Ga}_{0.88}\text{N}$ nanowire ensemble and the layer from which it was fabricated are presented in Fig. 3(c). The nanowire spectrum is red-shifted by 11 nm and much more intense. In order to verify whether these differences are caused by the structuring into nanowires, a planar reference samples was prepared which was annealed under similar conditions as applied for the Pt dewetting preceding the etching into nanowires. The PL spectrum of this sample is also included in Fig. 3(c). The annealing results in a substantial enhancement of the PL intensity compared to the as-grown layer, but the peak position barely changes. Thus, the red-shift of the nanowire sample is caused by the strain relaxation associated with the change in morphology and revealed by XRD.

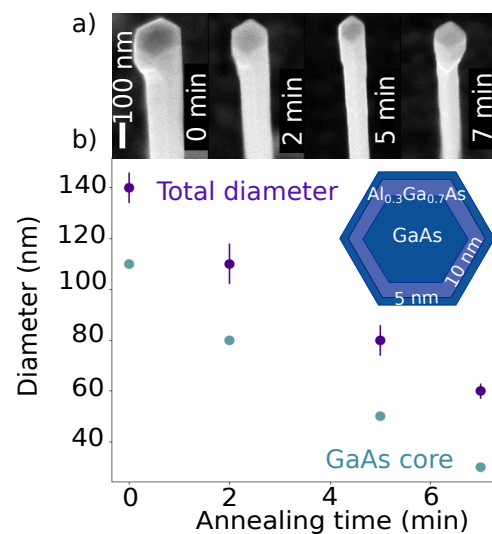
It is very interesting that the annealing itself leads already to brighter PL emission compared to the as-grown layer. Additional measurements of the annealed layer morphology did not reveal any changes in surface or interface roughness that could improve the external quantum efficiency. Hence, we attribute the enhancement in PL intensity induced by annealing to a higher internal quantum efficiency. This improvement suggests that the annealing process reduces the density of point defects in the $\text{In}_{0.12}\text{Ga}_{0.88}\text{N}$ layer. Last, the enhancement of the PL intensity of the nanowire sample compared to the annealed layer could be related to improved light coupling or the fact that the nanowire luminescence is less affected by TDs than the layer. In any case, our experiments demonstrate that the top-down structuring enhances the external quantum efficiency.

In summary, we have achieved the growth of 500-nm thick $\text{In}_{0.12}\text{Ga}_{0.88}\text{N}$ layers with uniform In composition, a low degree of strain relaxation of 10% and a low TD density of $\approx 1 \times 10^9 \text{ cm}^{-2}$. From such layers, we have fabricated an ensemble of nanowires with an average diameter of 45 nm and a density of $1.4 \times 10^{10} \text{ cm}^{-2}$. The change in structure from layer to nanowires leads to elastic relaxation. Most importantly, the nanowire fabrication process enhances substantially the external quantum efficiency. In another study, we have shown that we can control the nanowire dimensions by design of the Pt dewetting. Therefore, we have established a procedure for the large-scale top-down fabrication of tailored (In,Ga)N nanowire ensembles with high structural uniformity and luminescence efficiency.

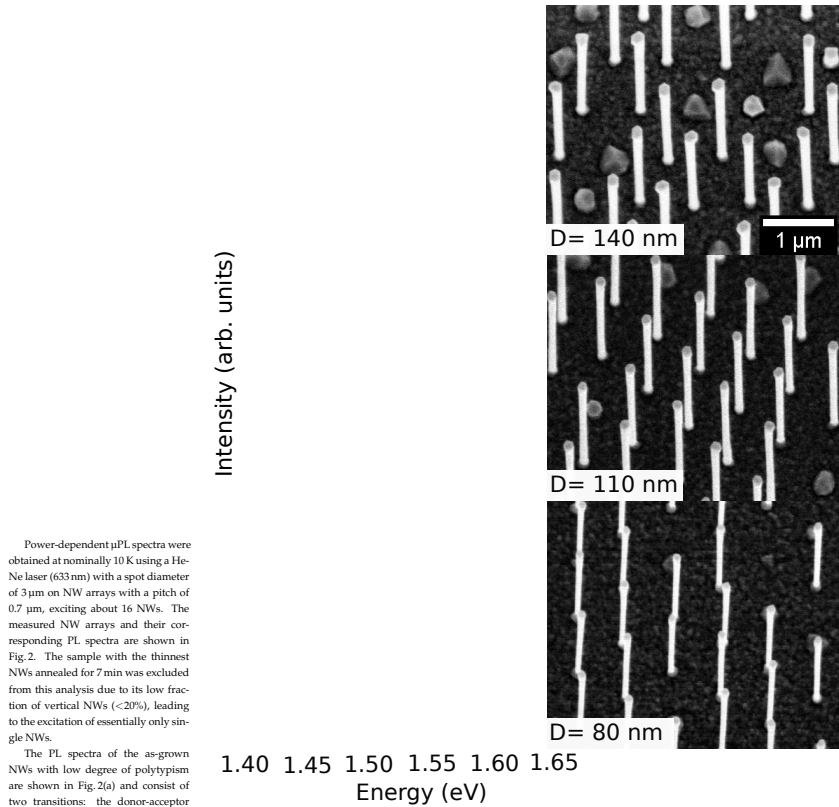
Diameter dependence of light absorption enhancement in GaAs nanowires evidenced by photoluminescence spectroscopy

F. Marin, O. Brandt, L. Geelhaar

Semiconductor nanowires (NWs) have attracted increasing interest for photovoltaic applications, among other reasons because the absorption of light can be enhanced compared to planar layers. This benefit is due to the more complex coupling of light with nanowires whose dimensions are of similar scale as the light wavelength. In fact, light absorption in NW arrays depends sensitively on the combination of wavelength and nanowire diameter, spacing, as well as length. This phenomenon has been extensively investigated by simulations, but experimentally it is very challenging to probe light absorption in NWs, in particular in single NW.



measured per sample). This way, the total diameter is controlled in the range 140—60 nm. We note that for all annealing times the nominal diameter of the NW core is larger than 20 nm and thus out of the quantum confinement regime. Furthermore, for light coupling only the total diameter is relevant since GaAs and (Al,Ga)As have similar real parts of the refractive index.



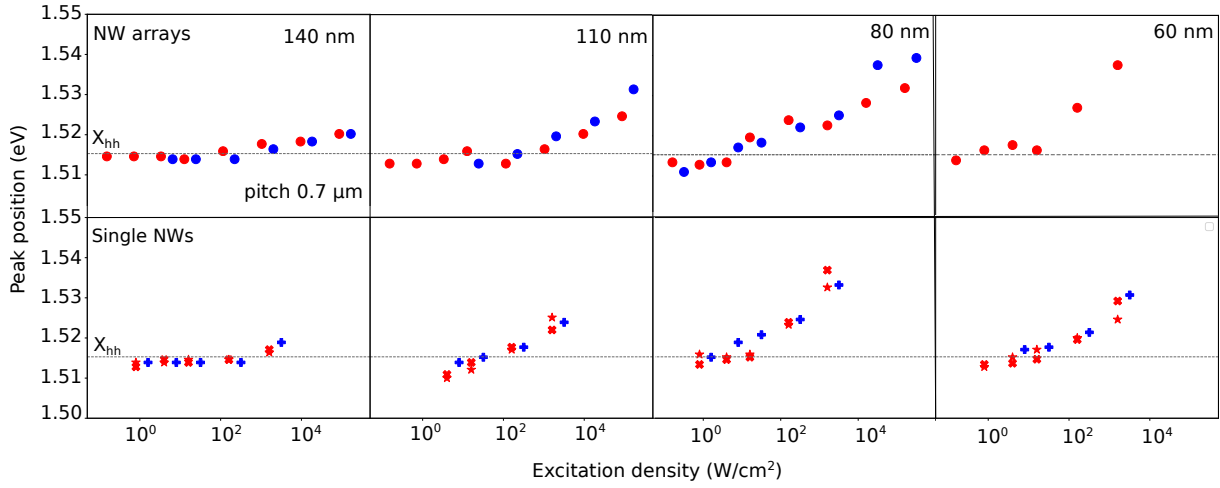


Fig. 3. X_{hh} peak position over excitation densities for (left) NW arrays and their corresponding single NWs (right). The blue and red data points refer to the excitation wavelength used. Different symbols represent different single NWs.

5 μm . In order to compare results between NW arrays and single NW measurements, it is important to consider the experimental difficulties for PL on single NWs: at the lowest excitation densities, focusing on single NWs is not precise, leading to an excitation density lower than the measured one. Also, due to thermal effects, it is not possible to reach the maximum excitation density as in the case of NW arrays.

We observed for all diameters, at the lowest excitation density, a red-shift with respect to X_{hh} bulk, which is attributed to the tensile strain exerted by the (Al,Ga)As shell on the core, indicating that the quantum confinement effect is weaker than the strain effect, i.e. negligible. With increasing excitation density, the X_{hh} peak position blue-shifts to energy transitions higher than X_{hh} in bulk GaAs, indicating a progressive band filling due to the increase of photogenerated carriers.

A comparison between NW arrays and single NWs with same diameter shows that single NWs achieve a higher blue shift than NW arrays at the same excitation densities. This stronger blue shift in single NWs can be explained by the light penetration depth, which increases with increasing nanowire spacing. A special case is the PL on 60 nm diameter NW arrays, where the low vertical yield shows that the PL signal corresponds to a single NW with a diameter around 90 nm and is therefore inconclusive.

Regarding the absorption dependence with excitation wavelength, there is no dramatic effect of the X_{hh} position for the two lasers used. In fact, for the two different excitation wavelength on NW arrays and single NWs, the stronger blue-shift was observed for NW with diameter of 80 nm.

To directly compare the diameter dependence of the light absorption enhancement on GaAs NWs, Fig. 4 shows the shift of X_{hh} over the NW diameter with increasing excitation densities for an excitation wavelength of 633 nm. Single NWs with a GaAs core of about 110 and 50 nm and an $\text{Al}_{0.3}\text{Ga}_{0.7}\text{As}$ shell of 30 nm thickness (pink data points) are shown to broaden the discussion. Dashed lines represent the expected red

shift due to tensile strain exerted by the (Al,Ga)As shell for different Al contents, transitions at energies lower than the dashed lines are identified as polytypic transitions. Different symbols represent different single NWs from the same sample.

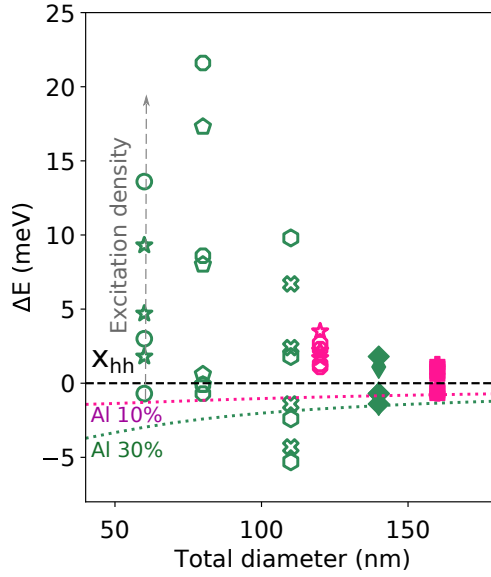


Fig. 4. X_{hh} position versus diameter for individual NWs. Green data points correspond to NWs with an $\text{Al}_{0.3}\text{Ga}_{0.7}\text{As}$ shell, pink to an $\text{Al}_{0.1}\text{Ga}_{0.9}\text{As}$ shell. Dotted lines indicate the expected red shift due to tensile strain of the shell on the core.

With decreasing NW diameter a stronger blue shift was observed, which is maximum for single NWs with an NW diameter of 80 nm and decreases for thinner NWs. This indicates the corresponding NW diameter for which the resonance is increased and therefore the stronger absorption enhancement is achieved. For a fixed wavelength, simulations of single standing GaAs predict an absorption enhancement at a certain diameter which is close to what we find experimentally. The difference can be explained by the presence of the (Al,Ga)As shell, which has a different imaginary refractive index than GaAs and therefore can affect the absorption of the structure.

In conclusion, we have explored the diameter-dependent light absorption enhancement through photoluminescence study, exploiting the low polytypic nature of these GaAs NWs. The absorption enhancement can be distinguished by the evolution of the two main transitions observed; the (D^0, C^0) and X_{hh} , observing an earlier saturation of the former and a stronger blue shift for the latter. As expected from simulations, a very small light absorption enhancement was found at diameters around 150 nm, and a strong increase with decreasing diameter, for which the enhancement maximum indicates photonic resonance.

Cathodoluminescence spectroscopy revealing the interplay of structural and point defects in GaN nanowires grown by molecular beam epitaxy

M. Gómez Ruiz, M. Brubaker¹, K. Bertness¹, O. Brandt, J. Lähnemann

Luminescence techniques are inherently sensitive to the presence of both radiative and nonradiative defects. With its high spectral and spatial resolution, cathodoluminescence (CL) spectroscopy is a powerful tool to identify and locate structural defects, to resolve variations in the concentration of point defects, and to provide valuable feedback on the incorporation of these defects and their interplay during the growth of nanostructures.

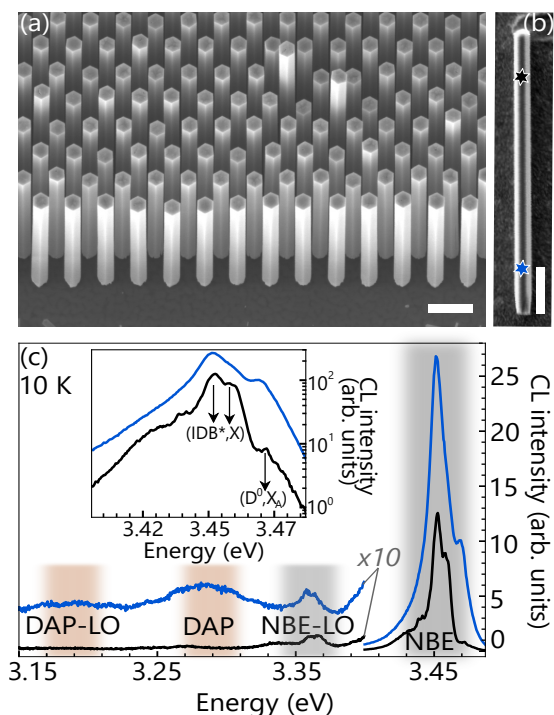


Fig. 1. (a) SE micrograph of a GaN NW ensemble in bird's eye (20°) view grown with $\Phi_N = 1 \mu\text{m/h}$. (b) SE micrograph of a GaN NW with $\Phi_N = 1 \mu\text{m/h}$ dispersed on an Au-coated Si substrate. Both scale bars are $1 \mu\text{m}$. (c) Representative low temperature (10 K) CL spectra recorded in the lower (blue) and in the upper part (black) of the NW, about $1 \mu\text{m}$ from the respective ends. The corresponding positions of the electron beam are indicated in (b).

Figure 1(c) presents the low-temperature CL spectra of two different regions of the NW displayed in Fig. 1(b). The representative spectra of the near-band-edge (NBE) emission shown in the inset are dominated by the recombination of excitons bound to donors (D^0, X_A) and excitons bound to inversion domain boundaries (IDB^*, X) [Auzelle *et al.*, Appl. Phys. Lett. **107**, 051904 (2015); Pfüller *et al.*, Phys. Rev. B **94**, 155308 (2016)].

¹National Institute of Standards and Technology, 325 Broadway, Boulder, CO 80305, USA

The prominence of the latter transition is explained below. Additionally, we observe an asymmetric donor-acceptor pair (DAP) transition at 3.26 eV that has a width of 60 meV, as well as the longitudinal optical (LO) phonon replicas of both the NBE and DAP emission bands. The NBE and the DAP transitions are found to be strongly enhanced in the lower with respect to the upper part of the NW. This trend in the emission intensity and width along the NW axis is a common feature in our measurements of the different NW arrays and samples.

In order to identify the underlying phenomena, we compiled experimental CL intensity profiles for the NBE and the DAP emission bands from hyperspectral line scans and averaged over 20 NWs as a function of the electron beam position along the NW axis [Fig. 2(a)-(b)]. In the case of the NBE, the variation in intensity is notable for a pitch of 0.3 μm , but becomes even more pronounced for a pitch of 1 μm . For both cases, we observe that the intensity first increases with increasing NW height, and then saturates at a NW height approximately equal to the pitch and subsequently declines. Such a behavior suggests that this effect may be caused by a gradient in impurity incorporation as discussed in the following. In the case of the DAP emission, the CL intensity profile for a pitch of 1 μm shows, in the same way, a maximum at 1 μm whereas for a pitch of 0.3 μm , no evident trend is observed.

Schematics of the NW growth at different lengths, where the incoming Ga atoms can either directly impinge on the Si_3N_4 mask or not are shown in Figs. 2(c) and (d), respectively. During the initial NW growth, a significant fraction of the incoming Ga atoms impinge on and can react with the Si_3N_4 mask leading to the unintentional incorporation of Si into the NW. The incorporation is gradually reduced once the NW height is approximately equal to their relative distance, where shadowing prevents the direct impingement of Ga atoms on the mask. In GaN NWs, the Fermi-level pinning at the NW side facets results in internal electric fields, the strength of which depends

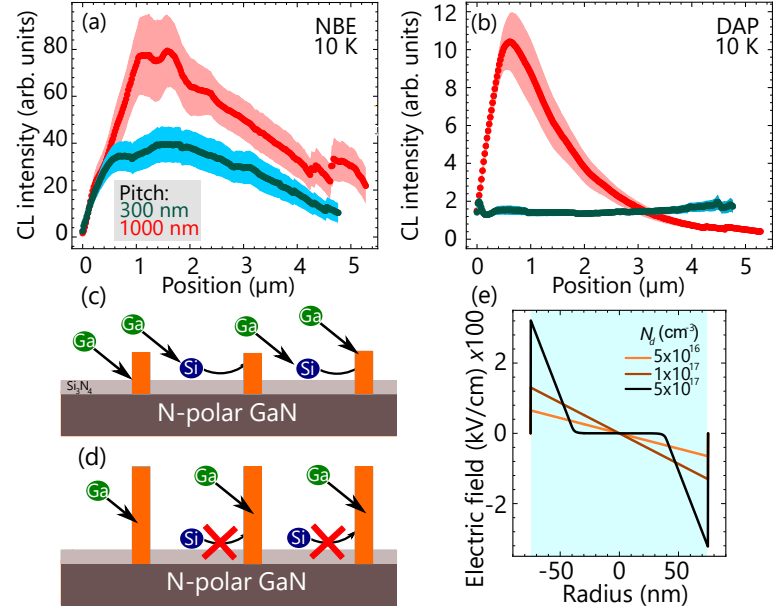


Fig. 2. Experimental CL intensity profiles obtained for (a) the NBE and (b) the DAP averaged over 20 NWs (the shaded area indicates the standard error) as a function of the electron beam position along the NW axis. (c) Schematics of the NW growth when the incoming Ga atoms interact with the Si_3N_4 mask and Si incorporates unintentionally into the NWs. (d) Schematics of the growth when the NW length is equal to their distance, where shadowing prevents the direct impingement of Ga atoms on the mask. (e) Internal electric field strength across a GaN NW with a diameter of 150 nm for different donor densities N_d .

on the doping concentration and the NW diameter [Calarco *et al.*, *Nano Lett.* **5**, 981 (2005)]. These fields can ionize excitons [Auzelle *et al.*, *ACS Photonics* **8**, 1718 (2021)] as well as shallow donors and acceptors and thus quench the corresponding emission intensities. For high doping and large NW diameters, the radial electric field is confined to the near-surface region and the CL intensity is enhanced due to the flat-band conditions in the field-free region around the center of the NWs. For NW diameters of 150 nm, as depicted in Figs. 2(e), a doping concentration above $5 \times 10^{17} \text{ cm}^{-3}$ is required to confine the electric field to the near-surface region and create a significant field-free region in the center. A gradient in Si doping, resulting from the reaction of Ga with the Si_3N_4 mask, can thus lead to a change of the volume fraction that hosts efficient radiative recombination and therefore account for the change in emission intensity. Furthermore, the strong unintentional doping and resultant lateral band profile prevents the additional field-induced quenching of the NBE luminescence under electron beam exposure observed in previous CL studies of GaN nanowires [Lähnemann *et al.*, *Nanotechnology* **27**, 455706 (2016)].

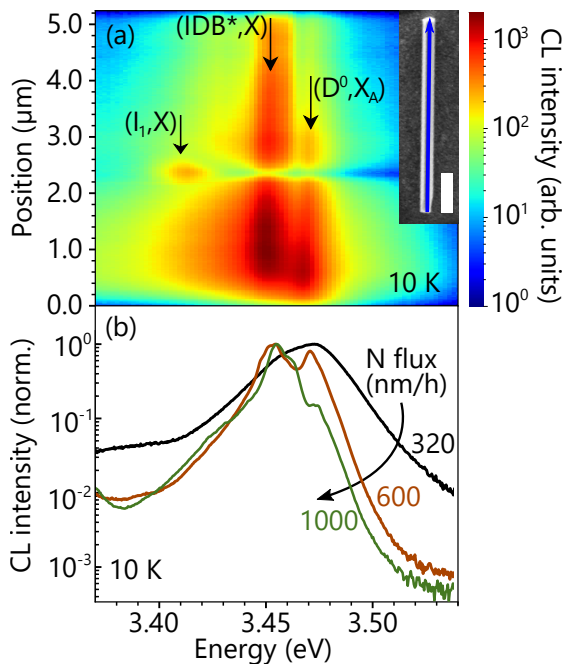


Fig. 3. (a) Low temperature (10 K) hyperspectral CL line scan along the axis of an exemplary GaN NW, as indicated by the blue arrow in the inset. The NW under study was grown at a pitch of $1 \mu\text{m}$ and a N flux of $1 \mu\text{m}/\text{h}$. The CL intensity for the NBE emission range is plotted on a logarithmic, color-coded scale. The spectral positions of the observed transitions are marked with arrows. The scale bar on the inset is $1 \mu\text{m}$ long. (b) Representative low temperature (10 K) CL spectra integrated over linescans on single GaN NWs grown with $\Phi_N = 0.32, 0.6$ and $1 \mu\text{m}/\text{h}$, respectively.

crystal phase quantum well effectively captures the generated carriers in its immedi-

The (IDB^*, X) transitions seen in the inset of Fig. 1(c) are observed for the majority of the studied NWs. We attribute the formation of IDBs to the significant and unintentional Si doping, which is known to induce a polarity inversion of GaN [Rosa *et al.*, *Surface Science* **600**, 335 (2006); Fernández-Garrido *et al.*, *Nano Lett.* **12**, 6119 (2012)]. Figure 3(a) displays a hyperspectral CL line scan along the axis of a GaN NW recorded at a sample temperature of 10 K. The contribution of the (IDB^*, X) transition is visible along the whole length of the NW, indicating that the IDBs do not terminate in the NW and exhibits the already discussed change in NBE intensity and width. In this specific NW, we additionally observe a spatially localized CL band at 3.41 eV. We attribute this emission band to the recombination of excitons at an I_1 basal plane stacking fault [Lähnemann *et al.*, *J. Phys. D: Appl. Phys.* **47**, 423001 (2014)]. Note that the I_1 emission is spatially complementary to the NBE emission bands as this

ate vicinity.

Figure 3(b) shows the normalised CL spectra at 10 K integrated over the entire length of single GaN NWs grown with three different N fluxes: $\Phi_N = 0.32, 0.6$ and $1 \mu\text{m/h}$. We observe that the CL spectrum of the sample grown at $\Phi_N = 0.32 \mu\text{m/h}$ is much broader than for those of samples grown with higher Φ_N such that the contributions of the (IDB*,X) and (D^0, X_A) lines to the NBE luminescence are not resolvable. Additionally, the corresponding CL intensity profiles for $\Phi_N = 0.32 \mu\text{m/h}$ (data not shown) exhibit a weaker intensity variation not correlated to the growth geometry as for the samples grown with $\Phi_N = 0.6$ and $1 \mu\text{m/h}$. We preliminarily assign both the spectral broadening and reduced gradients for $\Phi_N = 0.32 \mu\text{m/h}$ to a heavy doping of the NWs. The samples were further measured by Raman spectroscopy (not shown), which confirmed a higher carrier concentration for both large NW-to-NW pitch and low Φ_N .

Our hyperspectral CL mapping on GaN NWs identifies an unintentional doping by Si of the grown NWs under the presence of Ga on the substrate. While this doping results in a strong and stable luminescence intensity in the bottom parts of the NWs, the presence of Si induces the formation of IDBs in the NWs. To reduce the inadvertent doping levels and avoid IDB formation, a further reduced Φ_{III}/Φ_V flux ratio would need to be investigated. Thereby, we demonstrate how CL can serve as a powerful tool to map the presence and prevalence of both point and structural defects on the nanoscale. Thus, CL can contribute essential insights to the full understanding of growth processes of semiconductor nanostructures and is valuable to optimize growth protocols.

Microcavity phonoritons – a coherent optical-to-microwave interface

A. S. Kuznetsov, A. A. Reynoso, K. Biermann, A. Fainstein, P. V. Santos

The modulation of a quantum system at a rate faster than its decay rate opens the way for the coherent readout and conversion of its state. Such coherent manipulation is a steppingstone towards distributed quantum networks with bidirectional conversion between microwave qubits and optical photons. Phonons can facilitate such conversion for the implementation of these networks. This has motivated the search for systems that combine efficient optical readout, GHz-high phonon frequencies and large single-photon-to-phonon coupling rates.

In this context, microcavity (MC) exciton-polariton light-matter quasi-particles (simply polaritons) can act as an interface between microwave-generated GHz phonons and near-infrared photons. Here, confined polariton Bose-Einstein-like Condensates (BEC) with their ns-long temporal coherence and enhanced interactions with GHz phonons emerge as a platform for the implementation of these interfaces. Furthermore, it has been theoretically proposed, but so far not demonstrated, that the strong opto-mechanical coupling between polaritons and longitudinal acoustic phonons in direct-gap bulk semiconductors and MCs can lead to novel quasiparticles – phonoritons [L. V. Keldysh and A. L. Ivanov, *Sov. Phys. JETP* 57, 234 (1983), S. Latini et al., *Phys. Rev. Lett.* 126, 227401 (2021)]. Phonoritons are relevant, e.g., for novel optomechanical schemes for frequency conversion, phonon and photon lasing, acoustic diodes as well as for high temperature superconductivity.

Here, we present experimental evidence for phonoritons in hybrid polariton-phonon MCs by controlling the polariton-phonon coupling rate via the polariton and phonon

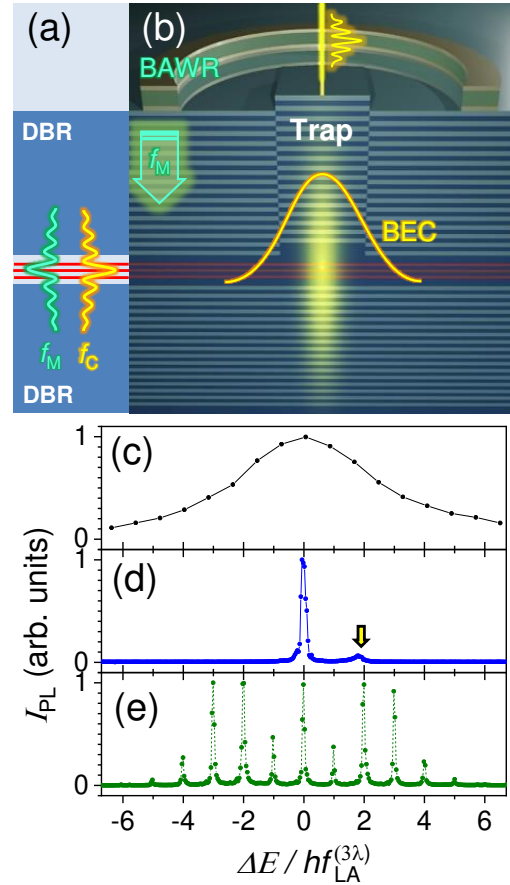


Fig. 1. (a) Simplified structure of a MC, which consists of a spacer embedding quantum wells (QWs, red horizontal lines) sandwiched between acousto-optic distributed Bragg reflectors (DBR). The structure provides the overlap of the optical (f_C) and phonon (f_M) modes with QWs. (b) A sketch of an intra-cavity trap with optically injected confined polariton BEC. Phonons can be injected a bulk acoustic wave resonator (BAWR). PL spectra of the trap at 10 K (c) low polariton density and (d) polariton BEC with BAWR Off. The small yellow arrow in (d) designates the weaker pseudo-spin state. (e) (BAWR On) emission of polariton BEC under coherent modulation by $f_{LA}^{3\lambda} = 7$ GHz phonons.

populations [A.S. Kuznetsov et al., Nat. Commun. (in press, 2023)].

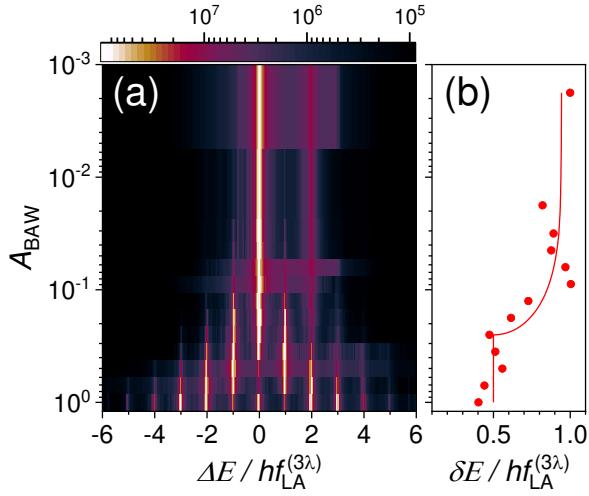


Fig. 2. (a) Dependence of the confined BEC emission spectrum on the acoustic amplitude (A_{BAW}). (b) Dependence of the fitted modulation linewidth (δE) on A_{BAW} . The red solid line represents the prediction of the model.

$f_{TA}^\lambda = 2 \times f_{LA}^{3\lambda} = 14$ GHz and $f_{TA}^{3\lambda} = 5$ GHz, respectively. By modulating the thickness of the cavity spacer on the nm-scale and on the μm lateral scale by shallow etching and MBE overgrowth, we create traps for polaritons and phonons, which further boosts the polariton-phonon interactions. Polaritons are injected into the trap using a non-resonant optical excitation, while the population of $f_{LA}^{3\lambda}$ phonons can be controlled by a bulk acoustic wave transducer (BAWR) fabricated on top of the MC, as shown schematically in Fig. 1(b).

For weak optical excitation (i.e., below the BEC threshold), the polariton ground state (GS) has a single but broad emission line with linewidth $\gamma_{MP} \sim 5 \times f_{LA}^{3\lambda}$, cf. Fig. 1(c). For the excitation above the BEC threshold, the linewidth drastically reduces to sub-GHz values, indicating the enhanced ns-long temporal coherence required to satisfy the condition $\gamma_{BEC} < f_{LA}^{3\lambda}$ for the coherent modulation, cf. Fig. 1(d). Moreover, the BEC GS displays two pseudo-spin resonances (the weaker one is indicated by an arrow) with an energetic splitting, which can lock to hf_{TA}^λ , cf. Fig. 1(d). The locking arises from a combination of non-linear polariton-polariton interactions with the efficient transfer of polaritons between the pseudo-spins mediated by absorption and emission of phonons. Per calculations, the transfer rate can exceed the linewidth of the pseudo-spin lines, which marks the emergence of the phonoriton. This also demonstrates the ability to control interactions between photons, excitons and phonons optically.

An important aspect of our platform is the ability to precisely control the population of $f_{LA}^{3\lambda}$ phonons using the piezoelectric BAWR. The color map of Fig. 2(a) shows BEC GS spectra as the function of the amplitude (A_{BAW}) of the $f_{LA}^{3\lambda}$ phonons, which was tuned

Our platform is based on hybrid light-sound (Al,Ga)As MC that co-localizes, within its spacer, optical mode for $\lambda_C = 800/n$ nm light, where $n \approx 3$ is the refractive index of the spacer, and strain field of a-few-GHz phonons. The MC maximizes the coupling of sound and light to excitons in GaAs quantum wells, as illustrated in Fig. 1(a). Specifically, MC confines two longitudinal acoustic (LA) modes with wavelength $\lambda = \lambda_C$ and $\lambda = 3\lambda_C$, and $f_{LA}^\lambda = 20$ GHz and $f_{LA}^{3\lambda} = 7$ GHz frequencies, respectively. Furthermore, each LA mode has an associated transverse (TA) one with frequencies of

by the radio-frequency power applied to the BAWR at a fixed frequency of 7 GHz. For very low A_{BAW} , the corresponding spectrum is shown in Fig. 1(d). With increasing acoustic amplitudes, additional lines corresponding to phonon sidebands appear.

The spectrum for the highest A_{BAW} in Fig. 2(a) is displayed in Fig. 1(e). The well-resolved sidebands, which are symmetrically located with respect to the central peak, prove the coherent modulation of the BEC by the phonons. The sidebands to the left (right) of the central peak correspond to the coherent emission (absorption) of phonons, thus demonstrating the bidirectional microwave-to-optical conversion.

Remarkably, Fig. 2(b) shows that the linewidth of the sidebands reduces by exactly 1/2 for high A_{BAW} values. Conceptually, the phonon field with lifetime exceeding $10^2/\gamma_{BEC}$ drives coherent oscillations between the pseudo-spin states. In the strong coupling regime, the swapping rate exceeds the γ_{BEC} . The polariton BEC then effectively spends half of the time as phonons, thus leading to a halving of their decay rate. This conclusion is further corroborated by a model calculation displayed by the solid line in Fig. 2(b). The model reveals that, unconventionally, the coupling rate depends both on the BEC and phonon populations.

Finally, we complement the microwave-phonon control of phonoritons with resonant optical one. As schematically shown in Fig. 3(a), the confined BEC is excited by an external narrow-band laser with tunable energy ($E_L = E_{ZPL} + \Delta_L$), where Δ_L is the detuning relative to the central BEC line (the zero-phonon-line, ZPL). For the detuned case, Fig. 3(b), phonoriton spectrum remains unchanged. In contrast, when the laser is resonant with one of the phonoriton peaks, the emission intensity is significantly enhanced while the linewidth decreases, cf. Fig. 3(c). This experiment thus demonstrates the coherent energy conversion between the external photons and phonoritons.

In conclusion, we have tailored the photonic, electronic and phonon resonances of patterned semiconductor MCs to demonstrate phonoritons. The latter are quasi-particles arising from the strong optomechanical coupling between polariton and phonons, which opens the way for the coherent bidirectional microwave-to-optical conversion in semiconductor systems. In perspective, our results also hint at a far richer physics in-

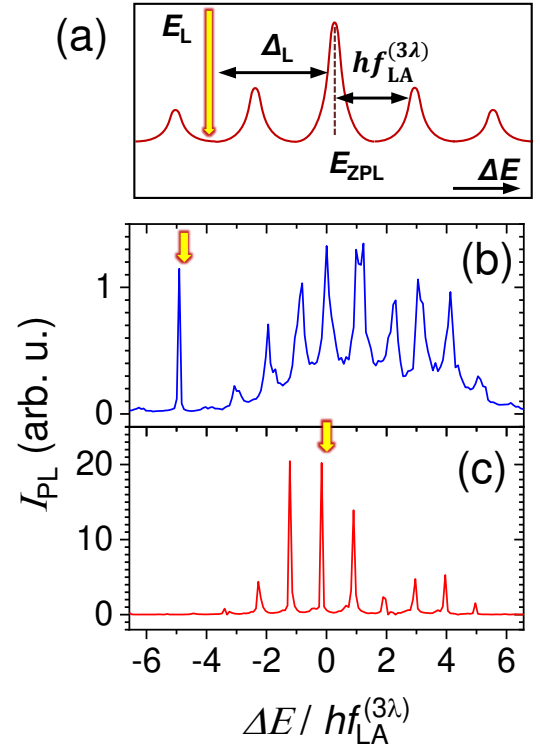


Fig. 3. (a) Experiment energy scheme. control laser detuning (Δ_L) position of the zero-phonon line (E_{ZPL}) (b) Reference GS spectrum in the absence of the control laser and (c) for selected values of Δ_L indicated by the yellow arrows.

volving new interaction regimes between optical, electronic, and mechanical degrees of freedom in the solid state, and challenge the existing understanding of the polaromechanical interactions, in particular, regarding the role of non-linear interactions.

We gratefully acknowledge the funding from German DFG (grant 359162958) and QuantERA grant Interpol (EU-BMBF (Germany) grant nr. 13N14783).

Imaging acoustic fields on surfaces and metasurfaces

A. Pitanti¹, M. Yuan, S. Zanotto², P. V. Santos

The last decades have witnessed a rich activity towards the integration of acoustic technologies within electro-optical circuits in high-frequency hybrid devices. The main role in this trend has been played by surface acoustic waves (SAWs), which are waves propagating along a surface that can be easily introduced in several material platforms exploiting the piezoelectric effect. Given their high operation frequency (typically up to ~ 10 GHz) and quality factors, simple, unidimensional SAW delay-line resonators have found wide application as sensors, spectral filters, and oscillators for telecommunication applications [K.-Y. Hashimoto, *Surface Acoustic Wave Devices in Telecommunications* (Springer, 2000)]. Further technological advances have made SAWs a flexible tool for both applied and fundamental physics, the latter reaching, for example, the quantum regime and enabling single particle manipulation [P. Delsing et al., *J. Phys. D* **52**, 353001 (2019)]. More complex manipulation of acoustic waves would boost SAW-based technologies even more, becoming a relevant key for the transition to 6G technologies. Here, one can expect, along with the increase in operating frequency, an enhancement of (acoustic) data transmission rate with spatial or frequency multiplexing, allowing on-chip operations on several parallel communication channels. Similarly to electromagnetic waves, acoustic waves can be manipulated by using artificially defined structures in the form of phononic crystals (PhC) or acoustic metasurfaces. The impressive results obtained in advanced light control are presently being translated to acoustic waves with μm -sized wavelengths ($\sim\text{GHz}$ frequencies), propagating on the millimeter to centimeter scale. Interesting proof-of-concepts experiments have already been demonstrated or theoretically proposed, like acoustic holography [M. Xu et al. *Advanced Materials* **35**, 2208002 (2022)] or negative acoustic refraction [H. He et al. *Nature* **560**, 61 (2018)], albeit mostly in the kHz to MHz frequency range. Extension to the GHz range would offer the most promise for integration with modern communication technologies, including mm to cm footprint devices operating at the frequency of the standard electromagnetic carrier waves for wireless telecommunication. Moreover, the acoustic wavelengths of the mostly used semiconductor materials in the GHz range is comparable to those of 3rd telecom window photons: SAW-based structures can thus offer a powerful platform for photon manipulation [M. M. De Lima Jr. et al., *Rep. Prog. Phys.* **68**, 7 (2005)] and optomechanical hybrid systems for light-based telecommunication.

The development of high-frequency SAW-based devices for the next generation technologies requires efficient techniques for locally probing GHz acoustic field distribu-

¹on leave from NEST Lab., CNR-NANO, piazza San Silvestro 12, 56127, Pisa, Italy

²NEST Lab., CNR-NANO, piazza San Silvestro 12, 56127, Pisa, Italy

tions in the sub- μm length scale. In this context, we will illustrate two scanning probe techniques currently used for a fine investigation of GHz acoustic fields in complex devices. The two techniques, based on light interferometry and atomic force microscopy, respectively, represent state-of-the-art technologies for direct and nonlinear detection of surface waves and will be here employed for investigating phononic crystals for complex wave manipulation.

In a recent publication, we have reported the use of phononic crystal to manipulate the refraction of GHz SAWs [S. Zanotto et al., *Nat. Comm.* **13**, 5939 (2022)]. In the experi-

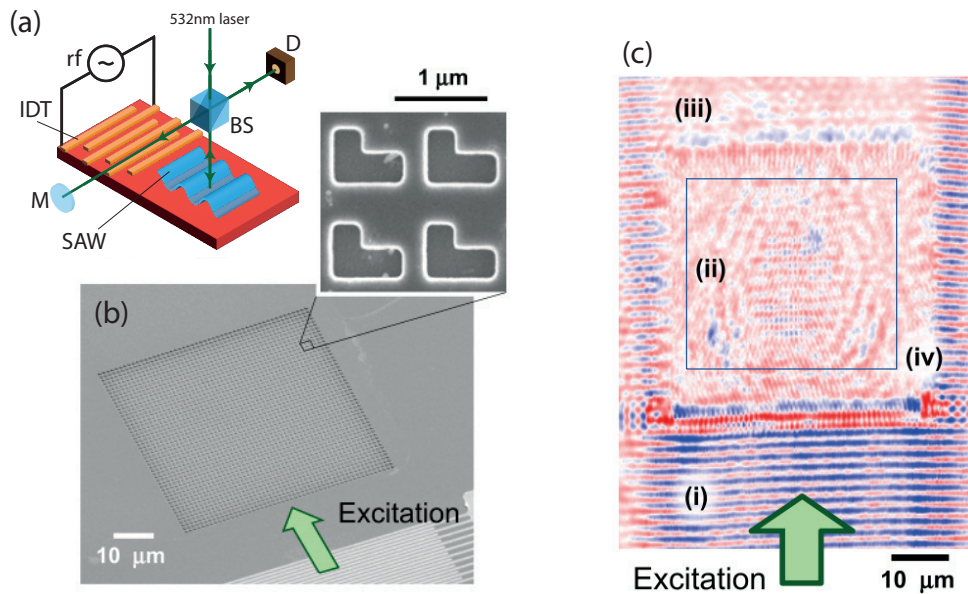


Figure 1: (a): Scheme of the laser interferometer experimental setup. (b): SEM micrograph of the investigated photonic crystal. A detail of the pattern is shown in the inset. (c): Typical interferometric measurement. SAW is incoming from the bottom (i), exciting Bloch modes in the patterned region (ii) and being partially transmitted (iii). Given the lateral wavefront size, acoustic waves can propagate along the phononic crystal side (iv).

ment we have mapped the acoustic fields using light interferometry. With reference to the scheme of Fig. 1 (a), we adapted a standard Michelson interferometer in such a way that one of the arms ended on the sample surface, while the other on a standard mirror (M). The presence of SAWs, generated by an interdigitated transducer (IDT) biased at radio frequencies (rf), changes the sample reflectivity, which modified the interferogram at the detector (D) accordingly. The investigated devices have been fabricated in GaAs material, placing metallic IDTs designed to resonate at different frequencies in front of a patterned region comprised by a square lattice of *L-shaped* holes, see Fig. 1 (b). Removing the sacrificial layer underneath the pattern resulted in a suspended phononic crystal membrane, which can be acoustically excited by SAWs and probed by light interferometry. Changing the laser position, it is possible to directly map the vertical acoustic displacement, producing data similar to the ones in Fig. 1 (c). Here, it

is possible to recognize different regions: the flat wavefront of the excited SAW coming from the bottom (i), which evolves then in the Bloch modes within the phononic crystal (ii) and gets partially transmitted (iii). Given that the lateral SAW wavefront is larger than the phononic crystal, a portion of the wave propagates around the device (iv).

Taking the Fourier transform of the interferometric signal within the square region of Fig. 1 (c) reveals interesting properties of the wave propagation within the phononic crystal. The resulting reciprocal space map has been reported in Fig. 2 (a), in a white-to-dark red colorscale proportional to the out-of-plane displacement of the different acoustic modes. It is possible to distinguish clear features, which are well-reproduced in the theoretical map of Fig. 2 (b).

It is a well known fact that the group velocity of a mode with a certain wavevector in the reciprocal space can be obtained from the gradient of its isofrequency contour. Since the surface wave propagation in GaAs is well known, elaborating the results of Fig. 2 (a) we can determine, for each incident angle of the SAW incoming from the substrate, θ_i , the relative diffracted angle by the phononic crystal, θ_r . The result has been

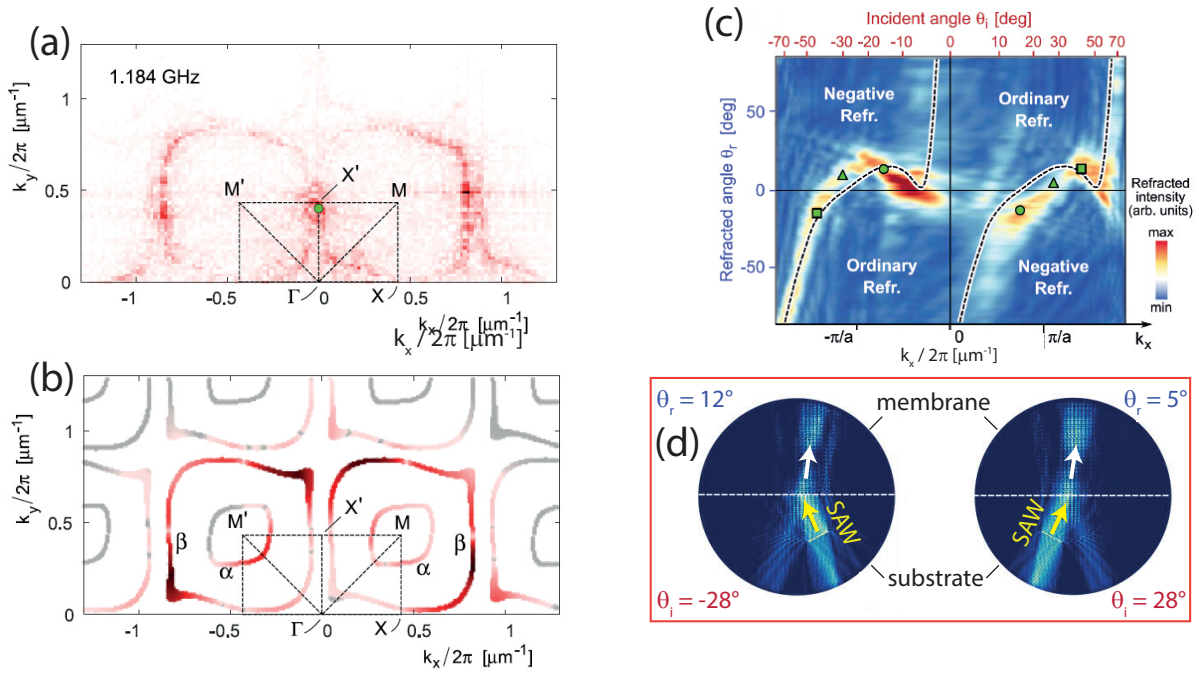


Figure 2: Experimental (a) and simulated (b) isofrequency contour obtained from the interferometric map. (c): Refracted versus incident angle map. (d): simulation of the asymmetric negative refraction regime.

summarized in Fig. 2 (c). Here it is possible to identify different refraction regimes, including ordinary and negative refractions. It is also worth to note the peculiar **Asymmetric negative refraction** regime, for example at $\pm 28^\circ$ incidence. This is illustrated in the finite-element-method simulations of Fig. 2 (d), where the bottom half of the circular simulation domain is an ordinary GaAs slab, while the upper half is the pat-

terned membrane. For a -28° angle of incidence, we find a negative refracted wave at $\theta_r = 12^\circ$. Inverting the sign of the incident angle would normally flip the sign of the refracted angle accordingly; here, instead a 28° incidence produces an ordinary refracted wave at 5° . Our experiments show how high-frequency acoustic wave can be manipulated by appropriately designing passive phononic crystals elements.

An equally intriguing possibility for mapping SAW fields employs atomic force microscopy (AFM). Even if the the mechanical cantilever tip used as a probe cannot follow

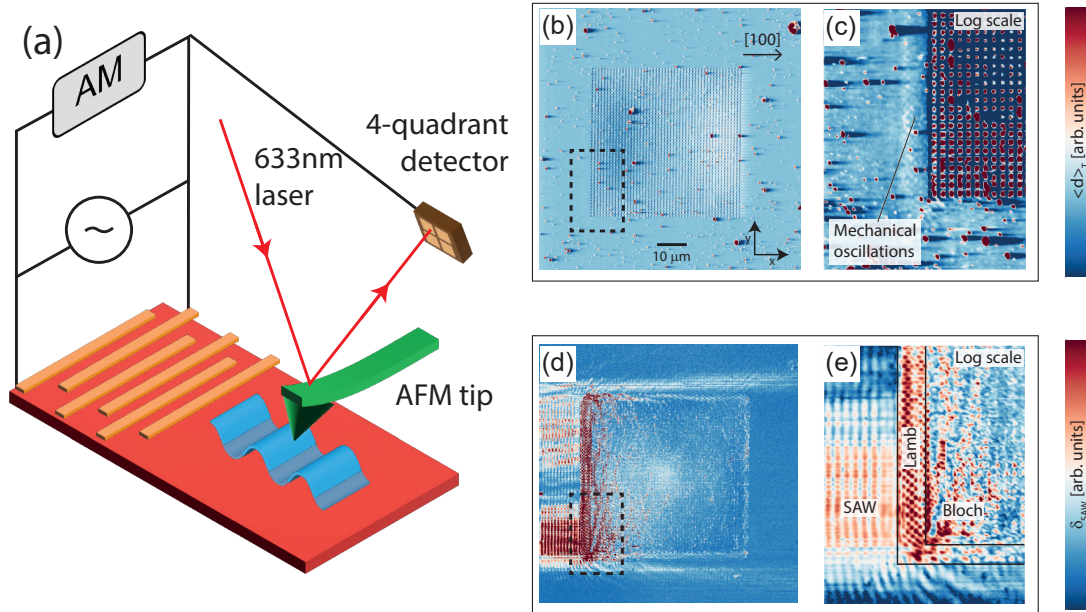


Fig. 3. Scheme of the acoustic AFM technique (a). Topography (b-c) and displacement (d-e) of a typical device excited with a SAW of frequency 1.18 GHz.

oscillations at 100s of MHz and above, it is possible to obtain a partial rectification of the SAW perturbation, exploiting the nonlinearity of the tip-to-surface interaction, resulting in a net signal in the “slow” tip deflection when the SAW is probed [T. Hesjedal, *Rep. Prog. Phys.* **73**, 016102 (2009)]. The weak nonlinear SAW signal can be efficiently extracted by imposing an amplitude modulation (AM) on the rf source which can then be used as a reference for lock-in demodulation (see Fig. 3 (a)). The main advantage of acoustic AFM (AAFM) lies in the ultra-high lateral resolution, whereas in optical interferometry it is essentially limited by the employed laser wavelength; conversely AAFM returns a signal proportional to the square of the displacement w , $\delta_{SAW} \propto w^2$, while optical interferometry assesses the linear displacement. Figure 3 reports a typical AAFM measurement of a device similar to the one previously described. Panel (b) displays the topography map given by the cantilever time-averaged deflection signal $\langle d \rangle_T$. Using a logarithmic colorscale, it is possible to see a weak contribution coming from the SAW mechanical oscillations (panel (b)). The latter can be efficiently extracted via lock-in demodulation at 535 kHz, producing the map reported in Fig. 3 (d). As can

be better inspected in the magnified panel (e), one can easily recognize the incoming SAW (from the left), coupling to a Lamb wave in the unpatterned suspended region and finally to Bloch modes within the patterned suspended region.

In conclusion, we have demonstrated how passive devices such as phononic crystals can be efficiently used for manipulating \sim GHz and above acoustic waves. Scanning probe techniques for imaging acoustic fields are quintessential tool for detailed device investigation, unveiling interesting features which will be the foundation for future hybrid and acoustic technology.

We acknowledge financial support by the Alexander von Humboldt Foundation through its Experienced Researcher Fellowship program.

Quantification of magnetoacoustic waves in epitaxial Fe₃Si/GaAs hybrid structures

M. Rovirola¹, M. Waqas Khaliq², B. Casals¹, M. Foerster², M. A. Niño², L. Aballe², J. Herfort, J. M. Hernández¹, F. Macià¹, A. Hernández-Mínguez

The use of charge carriers for information processing has proven to be very successful, but current technology is reaching its limits, and the growing need for smaller, faster, and more efficient information processing units requires new types of data carriers. Possible candidates that are compatible with existing technology and involve low energy dissipation are collective excitations of magnetic order, such as spin waves and skyrmions. In recent years, the dynamic strain of surface acoustic waves (SAWs) has been shown to be an efficient tool to control magnetization dynamics at the nanoscale via the magnetoelastic (ME) coupling. In this context, imaging techniques capable of quantifying both SAW and magnetization dynamics are required to fully understand the interaction between these excitation modes. In this contribution, we use time- and space-resolved x-ray photoemission electron microscopy (XPEEM) with x-ray magnetic circular dichroism (XMCD) sensitivity to simultaneously image SAWs and magnetization in hybrid ferromagnetic/semiconductor structures and to quantify the amplitude of magnetoacoustic waves excited by the SAW strain field [M. Rovirola *et al.*, accepted for publication in *Phys. Rev. Appl.*].

Figure 1(a) shows a scheme of the experimental setup. The sample under investigation consists of a Fe₃Si film grown on a GaAs(001) substrate by molecular beam epitaxy. First, a clean c(4×4)-reconstructed GaAs surface was prepared by growing a 500-nm-thick GaAs buffer layer in a dedicated III-V semiconductor growth chamber. The substrate was then transferred in ultra-high vacuum to an As-free chamber, where the Fe₃Si film with a thickness of $d = 74$ nm was grown on the GaAs substrate by co-deposition of Si and Fe from high-temperature effusion cells. Next, the Fe₃Si film was etched into rectangular mesas with a length of $L = 3.2$ mm. In the final fabrication step, pairs of interdigital transducers (IDTs) for SAW generation and detection were patterned on the GaAs regions at the opposite sides of the Fe₃Si mesas by e-beam lithography, metal evaporation, and lift-off. The finger periodicity of the IDTs determines the SAW wavelength, which was set to $\lambda_{\text{SAW}} = 5.73$ μm to excite SAWs with a frequency of $f_{\text{SAW}} = 500$ MHz and a wave vector \mathbf{k}_{SAW} propagating along the $x \parallel [110]$ axis of the GaAs substrate.

The XPEEM experiments were performed by placing the sample on a holder containing coplanar waveguides for applying radio frequency signals to the IDTs and an electromagnet to generate an in-plane magnetic field, \mathbf{B} , parallel to \mathbf{k}_{SAW} . To visualize

¹Department of Condensed Matter Physics, University of Barcelona, Martí i Franquès 1, 08028 Barcelona, Spain

²ALBA Synchrotron Light Source, 08290 Cerdanyola del Vallès, Spain

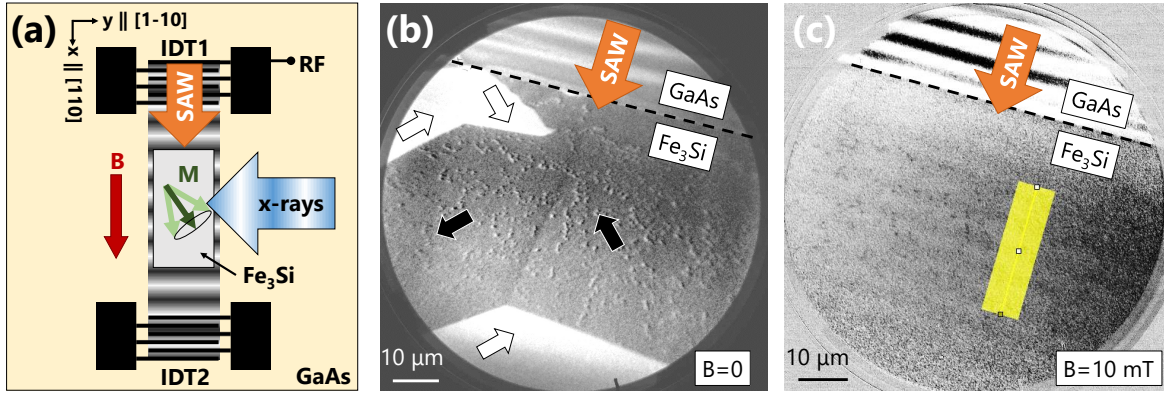


Fig. 1. (a) Schematic set-up of the sample under study. A radio frequency (RF) signal sent to IDT1 excites a SAW propagating along Fe_3Si film. The in-plane magnetic field, B , rotates the magnetization, M , towards the direction of the SAW. The x-rays are sent to the sample perpendicularly to the SAW propagation direction. (b) XMCD image of magnetic domains in Fe_3Si at $B = 0$. The black and white arrows indicate the magnetization direction at each domain. (c) XMCD image under $B = 10$ mT showing magnetization oscillations in the Fe_3Si film. Both images have been digitally edited for better visualization of the magnetization.

the SAW and magnetization dynamics, XPEEM images are obtained by exciting the sample with x-ray pulses synchronized to the SAW frequency. The magnetic sensitivity is obtained by subtracting two identical XPEEM images taken with opposite x-ray circular polarizations. The brightness contrast of the XMCD images is proportional to the magnetization component along the in-plane incidence direction of the X-rays, which in our experiment is parallel to the $y \parallel [\bar{1}10]$ axis.

Figures 1(b) and (c) show XMCD images taken with a SAW arriving at the edge of the Fe_3Si film (marked by the black dashed line in the figures). Due to the high structural quality of the Fe_3Si film, the equilibrium magnetization, M , exhibits cubic in-plane anisotropy, with the easy and hard axes being the families of $\langle 100 \rangle$ and $\langle 110 \rangle$ planes, respectively. In the absence of B , the image in Fig. 1(b) reveals magnetic domains with strong brightness contrast. The white and black arrows indicate the estimated directions of M for each magnetic domain, with the magnetization lying along all four easy axis directions. Figure 1(c) shows the same sample area for the case of $B = 10$ mT. Here the magnetic domains are no longer present and the magnetization rotates towards the magnetic field direction. In this case, the dynamic strain of the SAW induces a time- and space-varying effective magnetic field, which leads to weak oscillations in the magnetization orientation. Figure 2(a) shows the amplitude of the oscillating XCMD signal along the yellow path of Fig. 1(c), which can be well fitted by a sinusoidal function with the period of the SAW wavelength (red curve). By comparing the amplitude of the oscillating signal with the equilibrium magnetization values extracted from the magnetic domain image in Fig. 1(b), we estimate a relative amplitude of the oscillating magnetization of $\delta m_y = \delta M_y / M \approx 0.025$. This corresponds to a precession angle around its equilibrium direction of about 1.3° .

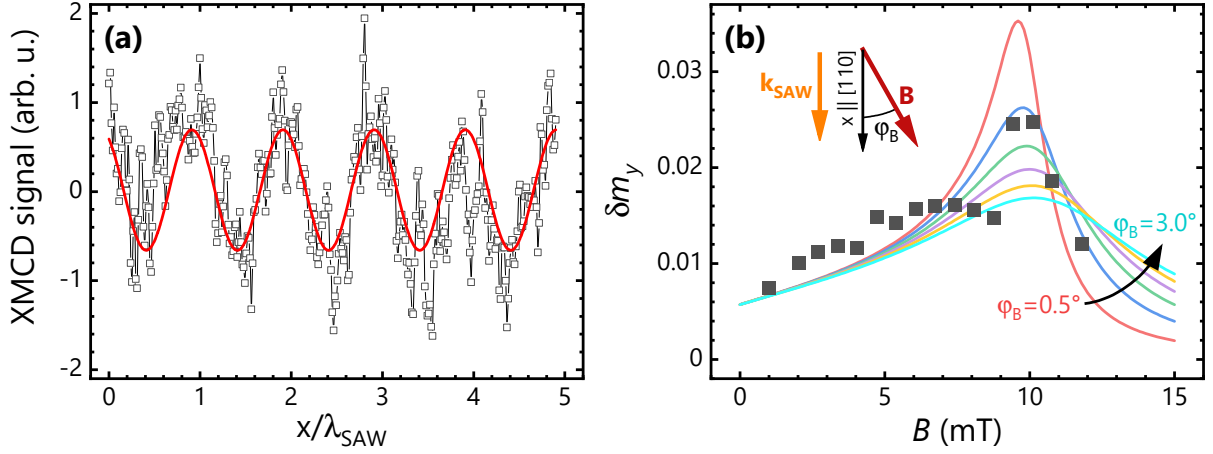


Fig. 2. (a) Spatial dependence of the XMCD signal along the yellow region in Fig. 1(c). The red curve is a fit to a sinusoidal function. (b) Amplitude of the magnetoacoustic waves obtained from the XMCD images as a function of the magnetic field strength (black squares). The solid curves are the result of numerical simulations under several misalignment angles φ_B between SAW propagation direction and magnetic field.

To confirm that these magnetization oscillations correspond to magnetoacoustic waves, we repeated the measurement of the XMCD images as a function of magnetic field strength. In the absence of \mathbf{B} , the frequency of spin waves in the Fe_3Si film is on the order of several GHz. However, as the magnetic field increases and the magnetization rotates from the easy axis to the direction of \mathbf{B} , the spin wave frequency decreases and reaches zero when \mathbf{M} is parallel to the $x \parallel [110]$ hard axis. Therefore, the amplitude of the SAW-excited magnetization oscillations should increase at the magnetic field strength for which the spin wave frequency and wave vector match those of the SAW. The results are shown in Fig. 2(b) (black squares), where two regions can be identified: a broad inverted parabola along the entire magnetic field range attributed to non-resonant magnetoacoustic excitation, and a narrow peak around 10 mT with a width of about 1 mT corresponding to the magnetic field strength where spin wave and SAW are close to the resonant condition.

To theoretically analyze the experimental results, we numerically solved the magnetization dynamics described by the Landau-Lifshitz-Gilbert equation:

$$\dot{\mathbf{m}} = -\gamma \mathbf{m} \times \mathbf{B}_{\text{eff}} + \alpha \mathbf{m} \times \dot{\mathbf{m}}, \quad (1)$$

where γ is the gyromagnetic ratio, α is the Gilbert damping constant, and the dot denotes the time derivative. The temporal evolution of $\mathbf{m} = \mathbf{M}/M$ depends on the effective magnetic field $\mathbf{B}_{\text{eff}} = -\vec{\nabla}_{\mathbf{m}} F$, where F is the normalized free magnetic energy. In addition to the Zeeman, shape, and crystalline anisotropy energies, it includes the magnetoelastic energy that couples the dynamic strain of the SAW to the magnetization in the Fe_3Si film. The solid curves in Fig. 2(b) show a summary of the results, where the magnetic field dependence of the magnetization oscillations along the y axis is plotted for several small misalignment angles of \mathbf{B} , φ_B , with respect to the $x \parallel [110]$

axis. The theoretical curves show a behavior similar to the experimental data, with a reasonable agreement for $\varphi_B \approx 1^\circ$. Finally, we also investigated the dependence of the simulated curves on the values of the magnetoelastic constants b_1 and b_2 for the Fe_3Si film. While the simulation is almost independent of the value of b_1 due to the geometry of the experiment, it depends strongly on the value of the b_2 constant. The best agreement between experimental results and simulation was obtained for $b_2 = 10 \pm 4 \text{ MJ/m}^3$.

In conclusion, we have studied the acoustic excitation of spin waves in hybrid structures consisting of a piezoelectric GaAs substrate and a ferromagnetic Fe_3Si thin film. We have directly imaged and quantified the magnetoacoustic waves excited by the dynamic strain of the SAW, observing a clear increase in the amplitude of the magnetization oscillations when spin wave and SAW are in resonance. Finally, we have determined the value of the shear magnetoelastic constant b_2 . These results provide valuable insight into the efficiency of the acoustic excitation and manipulation of spin waves in epitaxially grown ferromagnetic/semiconductor hybrid structures.

Towards terahertz quantum-cascade lasers with increased practical operating temperature

X. Lü, K. Biermann, L. Schrottke

Terahertz (THz) quantum-cascade lasers (QCLs) have been established as powerful radiation sources for THz high-resolution spectroscopy. THz QCLs developed at PDI were implemented for the local oscillator of the heterodyne spectrometer in the German Receivers for Astronomy at Terahertz frequencies (GREAT and upGREAT) on board the Stratospheric Observatory for Infrared Astronomy (SOFIA). From 2014 to 2022, the instruments were used for about 50 missions. Recently, the oxygen density in a plasma was determined using an absorption spectrometer [J. Wubs *et al.*, *Plasma Sources Sci. Technol.* **32**, 025006 (2023)] for which we developed the required lasers.

The most severe challenge is currently the necessary operation at cryogenic temperatures, since the optical gain of THz QCLs decreases at elevated temperatures. In view of realistic applications, we defined a practical operating temperature T_{po} at which the laser exhibits an output power of at least 1 mW in continuous-wave (cw) mode. Any increase of T_{po} , which is typically between 50 and 60 K, would facilitate the cooling, since the cooling power of mechanical systems increases with increasing temperature. Furthermore, $T_{po} > 80$ K would allow for the use of systems based on liquid nitrogen, while $T_{po} > 100$ K would even allow for passive cooling in space missions. To increase T_{po} , several approaches may be followed. An improved thermal management is expected to result in a lower temperature of the active region due to an improved conduction of heat to the heat sink so that the gain is increased. On the contrary, reduced resonator losses will lead to lower threshold gain. Furthermore, new designs of the active region with increased optical gain may be developed.

Currently, we focus on the development of designs with improved optical gain of the active region. These designs are intended to reduce the electron temperature by converting kinetic energy into potential energy. This approach is motivated by the fact that the electron temperature is significantly above the lattice temperature, which is probably caused by inefficient channels for relaxation of the kinetic electron energy to the lattice if the characteristic energies are below the energy of the longitudinal-optical (LO) phonon. The active regions of the new design include an additional quantum well (QW) that exhibits a transition energy lower than the energy of the LO phonon. Therefore, this transition is only possible for large-momentum and higher-energy electrons under emission of an LO phonon towards a low-momentum and lower-energy state so that a certain electron cooling is expected. The additional QW also leads to a stair-like structure from the ground state in the doped QW to the upper laser level, which also may lead to a conversion of kinetic into potential energy. Since an initial design, which was developed for 3.5 THz, exhibited promising oper-

ating properties with increased T_{po} , a design for 4.7 THz was developed by a gradual scaling of the layer structure. For both frequencies, sets of several lasers with varying doping density were grown by molecular beam epitaxy (MBE) for a systematic study of the operating properties. The Fabry-Pérot ridge QCLs are based on single-plasmon waveguides and can be operated in a mechanical cryocooler.

For the 3.5-THz design, 6 GaAs/AlAs QCLs were investigated. QCLs A (1.0*d*), B (1.2*d*), C (1.5*d*), D (1.8*d*), and E (2.2*d*) were grown in 2022, while QCL F (2.0*d*) was grown in 2023. The numbers in brackets denote the Si-doping density in the injection stage with $d = 10^{17} \text{ cm}^{-3}$. The ridge dimensions of these lasers are about $0.12 \times 1.0 \text{ mm}^2$. Figure 1 shows the light output-current density-voltage (*L-J-V*) characteristics at 35 K for these 6 QCLs.

For the lasers grown in 2022, the cw maximum output power at 35 K is in the range of 2–4 mW while the electrical pump power P_{elec} is in the range of 1–1.3 W. Due to the rather low values of P_{elec} , the cw output power can be increased by using wider or longer ridge stripes. QCL D has the lowest threshold current density of 112 A/cm^2 and highest output power of 4.1 mW. We conclude that the doping concentration of QCL D

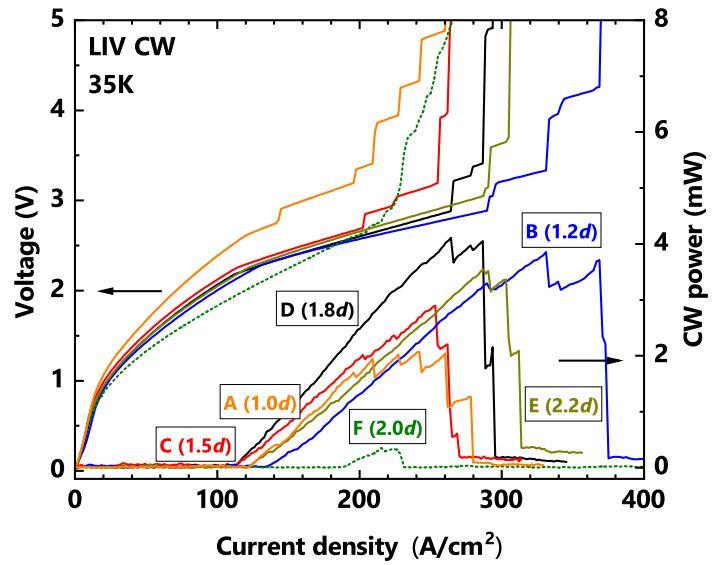


Fig. 1. *L-J-V* characteristics at 35 K for QCLs A, B, C, D, E, and F under cw operation.

has an optimum value. The significant variation of the threshold current density, output power, and dynamic range indicates the important role of the Si-doping density for the lasing properties of QCLs. QCL F was grown after maintenance of the MBE system. The nominal Si-doping density of QCL F is only 11% higher than that of QCL D. However, the maximum output power of QCL F is remarkably reduced to about 0.3 mW. This reduction suggests that the currently employed MBE system starts to exhibit severe problems with respect to a reproducible growth, which however is a prerequisite for a systematic empirical investigation and optimization of THz QCLs.

For the 4.7-THz design, 3 QCLs were grown with different doping density in the injection stage and bottom contact. The ridge dimensions of these lasers G (2.0*d*,2.0*b*), H (3.0*d*,2.0*b*), and I (3.0*d*,3.0*b*) are similar to the values for the 3.5-THz QCLs. The first number denotes the nominal Si-doping concentration in the active region with $d = 10^{17} \text{ cm}^{-3}$, while the second number denotes the Si-doping density in the bottom contact with $b = 10^{18} \text{ cm}^{-3}$. Figure 2 shows the *L-J-V* characteristics at 40 K for these

3 QCLs. The large differences in output power and current density for the lasers with nominally identical layer structures show again that the doping concentration is a very critical parameter for both the active region and the bottom contact layer. However, the number of QCLs for this design is too small to conclude the optimum doping. In addition to the exceptional low output power for QCL F, we found in an earlier secondary-ion mass spectroscopy study, that the Si flux may

deviate significantly from the nominal value. To understand and optimize the operating parameters of the lasers, systematic studies with a variation of individual parameters such as barrier thickness, doping concentration, have to be carried out, which requires stable and reproducible fluxes, in particular, of Si. For future systematic empirical studies, a new customized MBE system (MBE X) was installed.

The new MBE growth chamber comprises efficient vacuum pumps and 12 ports for high volume effusion sources to enable prolonged growth campaigns (estimated to 3.5 times the growth campaign duration of the old MBE system), thus limiting the effect of unintentional high impurity background doping during the first weeks after maintenance work. The higher material reservoirs of the group-III sources enable an increased flux stability, and due to the geometry of the chamber a higher lateral homogeneity is achievable, which – if desired – can be reduced by changing the distance from sources to substrate. A line-of-sight mass spectrometer will be used for improved As flux measurements. Finally, the Si source is mounted at a port far away from the As source, as the proximity of Si and As sources in the old system might have been caused some n-type doping instabilities.

To obtain more insight into the carrier dynamics and to improve the designs of our QCLs, we developed a new model based on the density matrix formalism. For the in-plane carrier distribution, no assumptions are made so that we may reasonably well simulate this distribution and may understand to what extent our new designs allow for carrier cooling. We start from the general equation of motion using Lindblad operators

$$\left. \frac{d\rho_{jn}}{dt} \right|_{ee,ep} = \frac{1}{2} \left[\text{tr} \left(\left[L^{ee,ep\dagger}, c_n^\dagger c_j \right] L^{ee,ep} \rho \right) \right] + \text{h.c.} \quad (1)$$

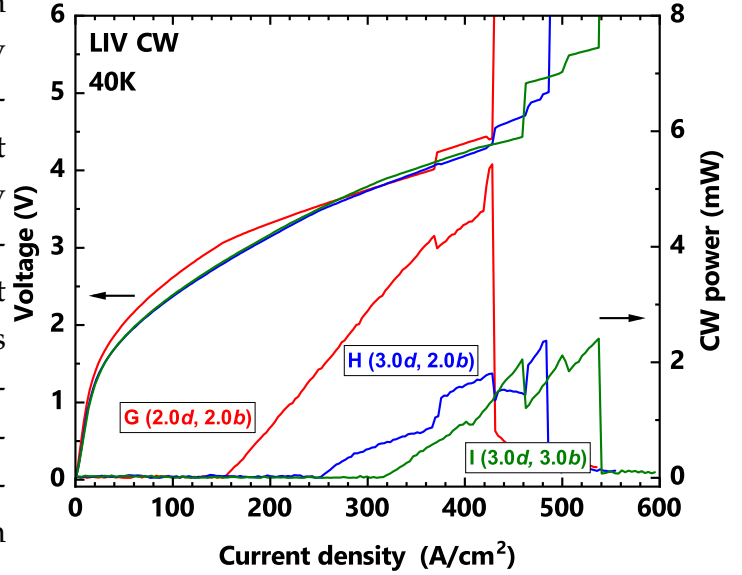


Fig. 2. L - J - V characteristics at 40 K for QCLs G, H, and I under cw operation.

with

$$L^{\text{ep}} = \sum_{j_1 n_1} L_{j_1 n_1}^{\text{ep}} c_{j_1}^\dagger c_{n_1} \quad (2)$$

for electron-phonon scattering, i.e. a "one-body problem", and

$$L^{\text{ee}} = \frac{1}{2} \sum_{j_1 j_2 n_1 n_2} L_{j_1 j_2 n_1 n_2}^{\text{ee}} c_{j_1}^\dagger c_{j_2}^\dagger c_{n_2} c_{n_1} \quad (3)$$

for electron-electron scattering, i.e. a "two-body problem", where h.c. labels the Hermitian conjugate. The indexes cover both the subband indexes of the heterostructure and all momentum states in the subbands. We derived general scattering rates for the density matrix elements assuming isotropy of the system so that only subband indexes and moduli of the in-plane momenta of the carriers are taken into account. These rates are expressed in terms of our Fourier transform model and can be included in the existing implementation of our previous model.

Unfortunately, the scattering rates depend in general on the matrix elements. Therefore, the rate equation system is no longer linear. To solve this system, we employ a self-consistent procedure, which can be integrated in the self-consistent solution of the Schrödinger and Poisson equations. We first solve the Schrödinger equation for a initial guess of the carrier distribution, i.e. of the electrostatic potential. In the next step, the scattering rates are calculated based on a corresponding initial guess of the density matrix followed by the solution of the generalized rate equation system that allows us to calculate a corrected electrostatic potential. Finally, the Schrödinger equation is solved again and all steps are repeated until the procedure exhibits satisfactory convergence. First tests for a simple superlattice show that convergence can be achieved and the diagonal elements of the density matrix, i.e. the occupation numbers of the states, are determined to be real with positive values between 0 and 1, which suggests that the Lindblad character of the operators is maintained by our approach.

However, the computation time is much too long. A significant part of the computation time is occupied by the determination of the scattering rates, which is a multi-dimensional summation of expressions for all combination of states. However, most of these contributions are very small as they do not fulfill the energy and momentum conservation and may be neglected. Currently, we work on a procedure which allows us to predetermine and select the significant contributions for the computation of the scattering rates. Provided that a considerable acceleration can be achieved, detailed insight in the carrier distribution and possible electron cooling is expected. The improved simulation of the carrier distribution in the cascade structure, the systematic empirical investigation of THz QCLs grown in the customized MBE, and the improvement of thermal and optical properties of the laser ridges are expected to considerably increase the value for T_{po} .

Facts and Figures

(as of 31.12.2023)

PDI Publications 2023

- Aleksandrova, A., C. Golz, H. Weidlich, M. Semtsiv, W. T. Masselink, and Y. Takagaki, Ballistic transport and surface scattering in (In,Ga)As-InP heterostructure narrow channels, *Semicond. Sci. Technol.* **38**, 055017 (2023).
DOI: [10.1088/1361-6641/acc08d](https://doi.org/10.1088/1361-6641/acc08d)
- Aleksandrova, A., C. Golz, K. Biermann, A. Trampert, M. Semtsiv, H. Weidlich, W. T. Masselink, and Y. Takagaki, Molecular beam epitaxy of InAs quantum wells on InP(001) for high mobility two-dimensional electron gases, *CrystEngComm* **25**, 5541 (2023).
DOI: [10.1039/D3CE00010A](https://doi.org/10.1039/D3CE00010A)
- Alonso-Orts, M., R. Hötzel, T. Grieb, M. Auf der Maur, M. Ries, F. Nippert, B. März, K. Müller-Caspary, M. R. Wagner, A. Rosenauer, and M. Eickhoff, Correlative analysis on InGaN/GaN nanowires: Structural and optical properties of self-assembled short-period superlattices, *Discover Nano* **18**, 27 (2023).
DOI: [10.1186/s11671-023-03808-6](https://doi.org/10.1186/s11671-023-03808-6)
- Andrade Deus, D. P. de, J. M. J. Lopes, and R. H. Miwa, Stacking order effects on the energetics and electronic properties of n -doped graphene/h-BN van der Waals heterostructures on SiC(0001), *Carbon* **213**, 118244 (2023).
DOI: [10.1016/j.carbon.2023.118244](https://doi.org/10.1016/j.carbon.2023.118244)
- Auzelle, T., M. Oliva, P. John, M. Ramsteiner, A. Trampert, L. Geelhaar, and O. Brandt, Density control of GaN nanowires at the wafer scale using self-assembled SiN_x patches on sputtered TiN(111), *Nanotechnology* **34**, 375602 (2023).
DOI: [10.1088/1361-6528/acdde8](https://doi.org/10.1088/1361-6528/acdde8)
- Baki, A., M. Abdeldayem, C. Morales, J. I. Flege, D. Klimm, O. Bierwagen, and J. Schwarzkopf, Potential of La-doped SrTiO₃ thin films grown by metal–organic vapor phase epitaxy for thermoelectric applications, *Cryst. Growth Des.* **23**, 2522 (2023).
DOI: [10.1021/acs.cgd.2c01438](https://doi.org/10.1021/acs.cgd.2c01438)
- Bengoechea-Encabo, A., S. Albert, M. Niehle, A. Trampert, and E. Calleja, Selective area growth of high quality GaN nanocolumns on Si(001) by plasma assisted molecular beam epitaxy, *Journal of Crystal Growth* **624**, 127367 (2023).
DOI: [10.1016/j.jcrysgro.2023.127367](https://doi.org/10.1016/j.jcrysgro.2023.127367)
- Bravo-Velázquez, C. A., L. F. Lastras-Martínez, O. Ruiz-Cigarrillo, G. Flores-Rangel, L. E. Tapia-Rodríguez, K. Biermann, and P. V. Santos, Spin relaxation of conduction electrons in coupled quantum wells, *Phys. Rev. B* **108**, 045306 (2023).
DOI: [10.1103/PhysRevB.108.045306](https://doi.org/10.1103/PhysRevB.108.045306)
- Cecchi, S., J. Momand, D. Dragoni, O. Abou El Kheir, F. Fagiani, D. Kriegner, C. Rinaldi, F. Arciprete, V. Holý, B. J. Kooi, M. Bernasconi, and R. Calarco, Thick does the trick: genesis of ferroelectricity in 2D GeTe-rich (GeTe)_m(Sb₂Te₃)_n lamellae, *Advanced Science* **11**, 2304785 (2024), published online November 21th, 2023.
DOI: [10.1002/advs.202304785](https://doi.org/10.1002/advs.202304785)

Chafatinos, D. L., A. S. Kuznetsov, A. A. Reynoso, G. Usaj, P. Sesin, I. Papuccio, A. E. Bruchhausen, K. Biermann, P. V. Santos, and A. Fainstein,
Asynchronous locking in metamaterials of fluids of light and sound,
Nat. Commun. **14**, 3485 (2023).

DOI: [10.1038/s41467-023-38788-9](https://doi.org/10.1038/s41467-023-38788-9)

Cheah, E., D. Z. Haxell, R. Schott, P. Zeng, E. Paysen, S. C. Ten Kate, M. Coraiola, M. Landstetter, A. B. Zadeh, A. Trampert, M. Sousa, H. Riel, F. Nichele, W. Wegscheider, and F. Krizek,
Control over epitaxy and the role of the InAs/Al interface in hybrid two-dimensional electron gas systems,

Phys. Rev. Materials **7**, 073403 (2023).

DOI: [10.1103/PhysRevMaterials.7.073403](https://doi.org/10.1103/PhysRevMaterials.7.073403)

Chen, W., K. Egbo, H. Tornatzky, M. Ramsteiner, M. R. Wagner, and O. Bierwagen,
In situ study and modeling of the reaction kinetics during molecular beam epitaxy of GeO₂ and its etching by Ge,

APL Mater. **11**, 071110 (2023).

DOI: [10.1063/5.0155869](https://doi.org/10.1063/5.0155869)

Dinh, D. V., J. Lähnemann, L. Geelhaar, and O. Brandt,
Lattice parameters of Sc_xAl_{1-x}N layers grown on GaN(0001) by plasma-assisted molecular beam epitaxy,

Appl. Phys. Lett. **122**, 152103 (2023).

DOI: [10.1063/5.0137873](https://doi.org/10.1063/5.0137873)

Dinh, D. V., F. Peiris, J. Lähnemann, and O. Brandt,
Optical properties of ScN layers grown on Al₂O₃(0001) by plasma-assisted molecular beam epitaxy,
Applied Physics Letters **123**, 112102 (2023).

DOI: [10.1063/5.0164058](https://doi.org/10.1063/5.0164058)

Egbo, K., J. Lähnemann, A. Falkenstein, J. Varley, and O. Bierwagen,
Acceptor and compensating donor doping of single crystalline SnO (001) films grown by molecular beam epitaxy and its perspectives for optoelectronics and gas-sensing,

Appl. Phys. Lett. **122**, 122101 (2023).

DOI: [10.1063/5.0130935](https://doi.org/10.1063/5.0130935)

Egbo, K., E. Luna, J. Lähnemann, G. Hoffmann, A. Trampert, J. Grümbel, E. Kluth, M. Feneberg, R. Goldhahn, and O. Bierwagen,
Epitaxial synthesis of unintentionally doped *p*-type SnO (001) via *suboxide* molecular beam epitaxy,

J. Appl. Phys. **133**, 045701 (2023).

DOI: [10.1063/5.0131138](https://doi.org/10.1063/5.0131138)

Fazlioglu-Yalcin, B., M. Hilse, and R. Engel-Herbert,
Thermogravimetric study of metal–organic precursors and their suitability for hybrid molecular beam epitaxy,

Journal of Materials Research **39**, 436 (2024), published online December 12th, 2023.

DOI: [10.1557/s43578-023-01237-w](https://doi.org/10.1557/s43578-023-01237-w)

Fazlioglu-Yalcin, B., A. C. Suceava, T. Kuznetsova, K. Wang, V. Gopalan, and R. Engel-Herbert,
Stoichiometric control and optical properties of BaTiO₃ thin films grown by hybrid MBE,
Adv. Materials Inter. **10**, 2300018 (2023).

DOI: [10.1002/admi.202300018](https://doi.org/10.1002/admi.202300018)

Fernando-Saavedra, A., S. Albert, A. Bengoechea-Encabo, A. Trampert, M. Xie, M. A. Sanchez-Garcia, and E. Calleja,

Growth of non-polar *m*-plane GaN pseudo-substrates by molecular beam epitaxy,

Journal of Crystal Growth **617**, 127272 (2023).

DOI: [10.1016/j.jcrysgro.2023.127272](https://doi.org/10.1016/j.jcrysgro.2023.127272)

Hanke, M., N. Ashurbekov, E. Zatterin, M. E. Msall, J. Hellemann, P. V. Santos, T. U. Schulli, and S. Ludwig,

Scanning X-ray diffraction microscopy of a 6-GHz surface acoustic wave,

Phys. Rev. Applied **19**, 024038 (2023).

DOI: [10.1103/PhysRevApplied.19.024038](https://doi.org/10.1103/PhysRevApplied.19.024038)

Hassanen, A. M., J. Herranz, L. Geelhaar, and R. B Lewis,
Bismuth surfactant-enhanced III-As epitaxy on GaAs(111)A,
Semicond. Sci. Technol. **38**, 095009 (2023).

DOI: [10.1088/1361-6641/ace990](https://doi.org/10.1088/1361-6641/ace990)

Hoffmann, G., M. Zupancic, D. Klimm, R. Schewski, M. Albrecht, M. Ramsteiner, F. Zohair, and O. Bierwagen,

Adsorption-controlled plasma-assisted molecular beam epitaxy of LaInO₃ on DyScO₃(110): Growth window, strain relaxation, and domain pattern,

Phys. Rev. Materials **7**, 084605 (2023).

DOI: [10.1103/PhysRevMaterials.7.084605](https://doi.org/10.1103/PhysRevMaterials.7.084605)

Jaber, N., J. Feldl, J. Stoeber, K. Irmischer, M. Albrecht, M. Ramsteiner, and J. Schwarzkopf,
Thermally activated increase of the average grain size as the origin of resistivity enhancement in NbO₂ films grown by pulsed-laser deposition,

Phys. Rev. Materials **7**, 014601 (2023).

DOI: [10.1103/PhysRevMaterials.7.014601](https://doi.org/10.1103/PhysRevMaterials.7.014601)

John, P., M. Gómez Ruiz, L. Van Deurzen, J. Lähnemann, A. Trampert, L. Geelhaar, O. Brandt, and T. Auzelle,

Growth kinetics and substrate stability during high-temperature molecular beam epitaxy of AlN nanowires,

Nanotechnology **34**, 465605 (2023).

DOI: [10.1088/1361-6528/acefd8](https://doi.org/10.1088/1361-6528/acefd8)

Kaganer, V. M., O. V. Konovalov, G. Calabrese, D. van Treeck, A. Kwasniewski, C. Richter, S. Fernández-Garrido, and O. Brandt,

X-ray scattering study of GaN nanowires grown on Ti/Al₂O₃ by molecular beam epitaxy,

J. Appl. Crystallogr. **56**, 439 (2023).

DOI: [10.1107/S1600576723001486](https://doi.org/10.1107/S1600576723001486)

Kuznetsov, A. S., K. Biermann, A. A. Reynoso, A. Fainstein, and P. V. Santos,
Microcavity phononitons – a coherent optical-to-microwave interface,
Nat Commun **14**, 1 (2023).

DOI: [10.1038/s41467-023-40894-7](https://doi.org/10.1038/s41467-023-40894-7)

Kuznetsova, T., M. Müller, S. F. Fischer, and R. Engel-Herbert,

Toward ultraclean correlated metal CaVO₃,

APL Mater. **11**, 041120 (2023).

DOI: [10.1063/5.0143611](https://doi.org/10.1063/5.0143611)

Kuznetsova, T., J. Roth, J. Lapano, A. Pogrebnyakov, and R. Engel-Herbert,

Growth of SrMoO₃ thin films by suboxide molecular beam epitaxy,

J. Vac. Sci. Technol. A **41**, 053412 (2023).

DOI: [10.1116/6.0002853](https://doi.org/10.1116/6.0002853)

Lin, Y.-C., R. Torsi, R. Younas, C. L. Hinkle, A. F. Rigosi, H. M. Hill, K. Zhang, S. Huang, C. E. Shuck, C. Chen, Y.-H. Lin, D. Maldonado-Lopez, J. L. Mendoza-Cortes, J. Ferrier, S. Kar, N. Nayir, S. Rajabpour, A.

C. T. van Duin, X. Liu, D. Jariwala, J. Jiang, J. Shi, W. Mortelmans, R. Jaramillo, J. M. J. Lopes, R. Engel-Herbert, A. Trofe, T. Ignatova, S. H. Lee, Z. Mao, L. Damian, Y. Wang, M. A. Steves, K. L. Knappenberger, Z. Wang, S. Law, G. Bepete, D. Zhou, J.-X. Lin, M. S. Scheurer, J. Li, P. Wang, G. Yu, S. Wu, D. Akinwande, J. M. Redwing, M. Terrones, and J. A. Robinson, Recent advances in 2D material theory, synthesis, properties, and applications, *ACS Nano* **17**, 9694 (2023).

DOI: [10.1021/acsnano.2c12759](https://doi.org/10.1021/acsnano.2c12759)

Liu, D. S. H., M. Hilse, A. R. Lupini, J. M. Redwing, and R. Engel-Herbert, Growth of nanometer-thick γ -InSe on Si(111) 7×7 by molecular beam epitaxy for field-effect transistors and optoelectronic devices, *ACS Appl. Nano Mater.* **6**, 15029 (2023).

DOI: [10.1021/acsanm.3c02602](https://doi.org/10.1021/acsanm.3c02602)

Liu, Z., B. Szczefanowicz, J. M. J. Lopes, Z. Gan, A. George, A. Turchanin, and R. Bennewitz, Nanoscale friction on MoS₂/graphene heterostructures, *Nanoscale* **15**, 5809 (2023).

DOI: [10.1039/D3NR00138E](https://doi.org/10.1039/D3NR00138E)

Lorenz, H., S. Kohler, A. Parafilo, M. Kiselev, and S. Ludwig, Classical analogue to driven quantum bits based on macroscopic pendula, *Sci Rep* **13**, 18386 (2023).

DOI: [10.1038/s41598-023-45118-y](https://doi.org/10.1038/s41598-023-45118-y)

Lü, X., B. Röben, K. Biermann, J. R. Wubs, U. Macherius, K.-D. Weltmann, J. H. van Helden, L. Schrottke, and H. T. Grahn, Terahertz quantum-cascade lasers for high-resolution absorption spectroscopy of atoms and ions in plasmas, *Semicond. Sci. Technol.* **38**, 035003 (2023).

DOI: [10.1088/1361-6641/acb1cd](https://doi.org/10.1088/1361-6641/acb1cd)

Lv, H., A. da Silva, A. I. Figueroa, C. Guillemard, I. F. Aguirre, L. Camosi, L. Aballe, M. Valvidares, S. O. Valenzuela, J. Schubert, M. Schmidbauer, J. Herfort, M. Hanke, A. Trampert, R. Engel-Herbert, M. Ramsteiner, and J. M. J. Lopes, Large-area synthesis of ferromagnetic Fe_{5-x}GeTe₂/graphene van der Waals heterostructures with Curie temperature above room temperature, *Small* **19**, 2302387 (2023).

DOI: [10.1002/smll.202302387](https://doi.org/10.1002/smll.202302387)

Lv, H., X. C. Huang, K. H. L. Zhang, O. Bierwagen, and M. Ramsteiner, Underlying mechanisms and tunability of the anomalous Hall Effect in NiCo₂O₄ films with robust perpendicular magnetic anisotropy, *Adv. Sci.* **10**, 2302956 (2023).

DOI: [10.1002/advs.202302956](https://doi.org/10.1002/advs.202302956)

Oliva, M., V. Kaganer, M. Pudelski, S. Meister, A. Tahraoui, L. Geelhaar, O. Brandt, and T. Auzelle, A route for the top-down fabrication of ordered ultrathin GaN nanowires, *Nanotechnology* **34**, 205301 (2023).

DOI: [10.1088/1361-6528/acb949](https://doi.org/10.1088/1361-6528/acb949)

Oliva, M., T. Flissikowski, M. Góra, J. Lähnemann, J. Herranz, R. B. Lewis, O. Marquardt, M. Ramsteiner, L. Geelhaar, and O. Brandt, Carrier recombination in highly uniform and phase-pure GaAs/(Al,Ga)As core/shell nanowire arrays on Si(111): Implications for light-emitting devices, *ACS Appl. Nano Mater.* **6**, 15278 (2023).

DOI: [10.1021/acsanm.3c03242](https://doi.org/10.1021/acsanm.3c03242)

- Paysen, E., S. Schütt, S. Michler, Q. Yang, R. Aidam, and A. Trampert, Interface tomography of GaInAs/AlInAs quantum cascade laser active regions, *Semicond. Sci. Technol.* **38**, 055009 (2023).
DOI: [10.1088/1361-6641/acc34f](https://doi.org/10.1088/1361-6641/acc34f)
- Peraticos, E., S. Kumar, M. Pepper, A. Siddiki, I. Farrer, D. Ritchie, G. Jones, and J. Griffiths, Resistance hysteresis in the integer and fractional quantum Hall regime, *Phys. Rev. B* **107**, 205307 (2023).
DOI: [10.1103/PhysRevB.107.205307](https://doi.org/10.1103/PhysRevB.107.205307)
- Pham, V. D., C. Dong, and J. A. Robinson, Atomic structures and interfacial engineering of ultrathin indium intercalated between graphene and a SiC substrate, *Nanoscale Adv.* **5**, 5601 (2023).
DOI: [10.1039/D3NA00630A](https://doi.org/10.1039/D3NA00630A)
- Puustinen, J., J. Hilska, A. Aho, E. Luna, A. Fihlman, and M. Guina, Low bandgap GaAsNBi solar cells, *Solar Energy Materials and Solar Cells* **264**, 112598 (2024) published online October 26th, 2023.
DOI: [10.1016/j.solmat.2023.112598](https://doi.org/10.1016/j.solmat.2023.112598)
- Rajabi Kalvani, P., A. Parisini, G. Sozzi, C. Borelli, P. Mazzolini, O. Bierwagen, S. Vantaggio, K. Egbo, M. Bosi, L. Seravalli, and R. Fornari, Interfacial properties of the SnO/ κ -Ga₂O₃ p-n heterojunction: A case of subsurface doping density reduction via thermal treatment in κ -Ga₂O₃, *ACS Appl. Mater. Interfaces* **15**, 45997 (2023).
DOI: [10.1021/acsami.3c08841](https://doi.org/10.1021/acsami.3c08841)
- Reis, A., M. Hanke, O. Bierwagen, A. Trampert, P. Mazzolini, and E. Welter, Disorder–order transition in Ga₂O₃ and its solid solution with In₂O₃ upon thermal annealing, *Phys. Status Solidi B* **260**, 2200535 (2023).
DOI: [10.1002/pssb.202200535](https://doi.org/10.1002/pssb.202200535)
- Reis, A., M. Hanke, J. M. J. Lopes, and A. Trampert, Anisotropic strain relaxation in epitaxially constrained α -(Al,Ga)₂O₃ thin films on a-plane Al₂O₃, *Applied Physics Letters* **123**, 122102 (2023).
DOI: [10.1063/5.0168314](https://doi.org/10.1063/5.0168314)
- Ries, M., E. Poliani, F. Nippert, D. Seidlitz, L. T. H. Greif, I. Koslow, J. Bläsing, M. Auf der Maur, A. Hoffmann, N. Esser, and M. R. Wagner, Impact of nanoscale fluctuations and cap-layer thickness in buried InGaN single quantum wells probed by tip-enhanced Raman scattering, *J. Appl. Phys.* **133**, 094303 (2023).
DOI: [10.1063/5.0129896](https://doi.org/10.1063/5.0129896)
- Ries, M., F. Nippert, B. März, M. Alonso-Orts, T. Grieb, R. Hötzel, P. Hille, P. Emtenani, E. M. Akinoglu, E. Speiser, J. Plaickner, J. Schörmann, M. Auf der Maur, K. Müller-Caspary, A. Rosenauer, N. Esser, M. Eickhoff, and M. R. Wagner, Origin of the spectral red-shift and polarization patterns of self-assembled InGaN nanostructures on GaN nanowires, *Nanoscale* **15**, 7077 (2023).
DOI: [10.1039/D2NR05529E](https://doi.org/10.1039/D2NR05529E)
- Rovirola, M., M. Waqas Khaliq, B. Casals, M. Foerster, M. A. Niño, L. Aballe, J. Herfort, J. M. Hernández, F. Macià, and A. Hernández-Mínguez, Resonant and off-resonant magnetoacoustic waves in epitaxial Fe₃Si/GaAs hybrid structures,

Ph. D. Theses

Nicolai, Lars

Interface Tomography of III-V Semiconductor Heterostructures
Humboldt-Universität zu Berlin

Hoffmann, Georg

Polarization-discontinuity-doped two-dimensional electron gas in BaSnO₃/LaInO₃ heterostructures grown by plasma-assisted molecular beam epitaxy

Liou, Yi-Ting

Acousto-electric Transport in Epitaxial Graphene on SiC

Master Thesis

Rose Mary, Jose

Control improvement in large-area top-down GaN nanowire fabrication
Technische Universität Ilmenau

Students Working on their Master Thesis

Doustipour, Farshad

Freie Universität Berlin

Kassa, Atekelte Abebe

Technische Universität Darmstadt

Seminars of Visitors

11.12.2023

Danielle Hickey, Pennsylvania State University

Understanding Atomic Structures and Properties Using Aberration-Corrected Transmission Electron Microscopy

7.12.2023

Gaia Tomasello, Advanced Electronics Materials

The use of Generative Artificial Intelligence tools in scientific writing and publishing with Wiley

15.12.2023

Sergio Valenzuela, ICN2 Barcelona

Designer van der Waals Heterostructures for Spintronic Applications

04.12.2023

Clemens von Korff Schmising, Max Born Institute Berlin

Ultrafast magnetization dynamics probed by transient spectroscopy in the extreme ultraviolet spectral range: recent results and prospects for 2D materials

24.11.2023

Arnaud Gloppe, CNRS & University of Strasbourg

Optomechanics of a suspended magnetic van der Waals membrane

23.10.2023

Nadire Nayir, Istanbul Technical University and Pennsylvania State University

Low-Dimensional Advanced Materials by Computational Modeling, Simulation and Theory: From Atomic Properties to Emergent Functionalities

19.10.2023

Simone Zanotto, Nanoscience Institute Pisa

Membrane metasurfaces: from high speed modulation to chiral coherent absorption

09.06.2023

Yongjin Cho, Cornell University, USA

MBE of Group-III Nitrides

07.06.2023

Fauzia Jabeen, Würzburg University, Germany

III-V Semiconductors by Molecular Beam Epitaxy for Optoelectronic and Photonic Applications

06.06.2023

John Freeland, Argonne National Laboratory, USA

Exploring Emergent Electronic and Magnetic States with X-rays

24.05.2023

Steffen Breuer, Fraunhofer Heinrich Hertz Institute, Germany

Ultrafast THz and SESAM Devices on InP

12.05.2023

Hubert J. Krenner, Universität Münster, Germany

Acousto-optoelectronics – driving the motion of carriers in low-dimensional semiconductors

09.05.2023

Andre Mkhoyan, University of Minnesota, USA

New Kind of Crystalline Line Defects in Perovskites Explored by Electron Microscopy

08.05.2023

Bharat Jalan, University of Minnesota, USA

Navigating MBE Growth of Atomically Precise Complex Oxides using Source Chemistry

03.04.2023

Frank Peiris, Kenyon College, USA

Spectroscopic Ellipsometry as an In-situ Tool to Monitor Growth and Optimize Structures

06.03.2023

Joshua A. Robison, Pennsylvania State University, USA

Semiconductors and Metals at the Atomic Limit

30.1.2023

Kevin Silverman, Quantum Nanophotonics Group, National Institute of Standards and Technology, Boulder, USA

Surface Acoustic Waves and InAs Quantum Dots for Quantum Transduction

25.1.2023

Arka Bikash Dey, PETRA-III, Hamburg

Structure of epitaxially grown SiGe, InGaAs quantum dots & FeO thin films

Budget Summary

Fiscal year	2022	2023 (31.12.2023)
	k€	k€
Revenues		
Allocations	11,218.6	11,802.7
Earnings	31.3	80.4
Sum	11,249.9	11,883.1
Expenditures		
Staff	5,362.6	6,200.1
Administrative expenses	2,988.5	2,803.8
Equipment investment funds	2,192.7	2,110.9
Sum	10,543.8	11,114.8
External funding through projects		
Granted funds	2,489.5*	2,714.6*
Spent funds	1,032.2	1,309.7

* including residual funds from the previous year

Summary of External Funding

Agency	Period	Title	Project leader	FST
EFRE	01.01.2023 – 31.12.2025	ZALKAL – Applikationslabor für Zeitaufgelöste Kathodolumineszenzspektroskopie	Dr. Jonas Lähnemann	9225
DAAD	01.01.2023 – 31.12.2024	Large-area top-down processing of (In,Ga)N and (Al,Ga)N nanowires	Dr. Jonas Lähnemann	9227
DFG	01.12.2015– 31.12.2023	Quantum Hall based Aharonov-Bohm spectroscopy: electron-electron interaction in non-linear magnetotransport	Dr. Stefan Ludwig	9174
DFG	01.11.2018 – 31.08.2024	Controlling Electron-Phonon Interaction in Nanocircuits – Strong Coupling Regime	Dr. Stefan Ludwig	9195
DFG	01.06.2020 – 31.05.2023	Artificial quantum states on semiconductor surfaces created and probed by cryogenic scanning tunneling microscopy	Dr. Stefan Fölsch	9209
DFG	01.04.2021 – 28.02.2025	Nanoscale optomechanical interactions in semiconductor microcavities	Dr. Paulo V. Santos	9208
DFG	01.01.2021 – 31.12.2024	Charge carrier dynamics under the influence of extreme strain gradients realized in bent semiconductor nanowires	Dr. Lutz Geelhaar	9210
DFG	01.02.2021 – 31.12.2024	Photoelectrochemical CO ₂ conversion with tunable semiconductor nanostructures	Dr. Lutz Geelhaar	9213
DFG	01.03.2021 – 31.05.2025	Point defects control in Ga ₂ O ₃ thin films grown via molecular beam epitaxy	Dr. Oliver Bierwagen	9217
DFG	01.09.2021 – 31.08.2024	New strategies for dislocation density reduction in monolithic III/V epitaxy on Si	Dr. Achim Trampert	9218
DFG	01.02.2022 – 31.01.2025	Lead-free piezoelectric nanowire-nanocellulose hybrids for flexible energy harveste	Dr. Thomas Auzelle	9219
DFG	01.05.2022 – 30.04.2025	Coherent GHz electro-optomechanics with polarmechanical crystals	Dr. Alexander Kuznetsov	9223
DFG	01.05.2022 – 30.04.2025	Coherent GHz electro-optomechanics with polarmechanical crystals	Dr. Paulo V. Santos	9224
DFG	01.02.2024 – 31.01.2027	Artificial quantum states on semiconductor surfaces created and probed by cryogenic scanning tunneling microscopy	Dr. Stefan Fölsch	9231
DFG	01.03.2024 – 28.02.2027	"Magic Tune" - Enabling large tunnel magnetoresistance at room temperature in scalable epitaxial van der Waals magnet heterostructures	Dr. J. Marcelo J. Lopes	9232
DFG (SPP)	01.03.2023 – 28.02.2026	Priority Programme "INtegrated TERAhertz sySTems Enabling Novel Functionality (INTEREST)" (SPP 2314) Micro-integrated terahertz quantum-cascade laser for high-resolution spectroscopy (Micro-QCL)	Dr. Lutz Schrottke	9222
DFG (OAK)	01.01.2023 – 31.12.2025	Open-Access-Publikationskosten	Anne Timm	9226
EU	01.09.2023 – 31.08.2027	Understanding, Predicting and Enhancing the Stability of Organic Photovoltaics (OPVStability)	Prof. Dr. Safa Shoaee	9234
WGL (SAW)	01.07.2021 – 30.06.2025	Defect-engineering in graphene via focused ion beam for tailored van der Waals epitaxy of h-BN (ENGRAVE)	Dr. J. Marcelo J. Lopes	9216
WGL (SAW)	01.02.2022 – 31.01.2025	(Si,Ge,Sn)O ₂ -based ultra-wide bandgap semiconductors for power electronics (SiGOPE)	Dr. Oliver Bierwagen	9220
WGL (SAS)	01.07.2020 – 31.12.2024	Growth and fundamentals of oxides for electronic applications (GraFOx II)	Dr. Oliver Bierwagen	9211
WGL	01.01.2024 – 31.12.2028	Next generation SustaInable semicoNductors For Optoelectronic aNd spintronic Applications (SINFONIA)	Prof. Dr. Safa Shoaee	9228

Visiting scientists

Name	Institute	Period	Topic	Country
Afif Siddiki	T.C. Maltepe University	12.01.2022 – 11.01.2023	Utilizing electronic transport at two-dimensional systems considering organic materials	Turkey
Taseer Anjum	Universität Siegen	01.10.2021 – 30.04.2023	X-ray-based analysis of bent semiconductor nanowires	Germany
Jason Gerke	Technische Universität Berlin	01.10.2022 – 31.03.2023	Microanalysis of (Al,Ga)As semiconductor heterostructures using energy-dispersive X-ray spectroscopy in the scanning transmission electron microscope	Germany
Anna Sacchi	Univerity of Parma	16.01.2023 – 15.03.2023	Growth and characterization of Si-doped epsilon/kappa-Ga ₂ O ₃ single domain layers	Italy
Stefano Cecci	Università degli Studi di Milano-Bicocca	01.01.2023 – 31.12.2023	Conclusion of studies related to Ge-Sb-Te alloys	Italy
Georg Hoffmann	Humboldt Universität Berlin	15.01.2023 – 28.02.2023	Oxid-Epitaxie	Germany
Tuan Dau	Centre National de la Recherche Scientifique	16.01.2023 – 23.01.2023	Undercoating of Gd-doped MoS ₂ layers by optical spectroscopy and transport measurements.	France
Frank Peiris	Kenyon College	01.02.2023 – 30.06.2023	Exploring the Optical Properties of High-band gap Semiconductors	USA
Joshua A. Robinson	Pennsylvania State University	03.03.2023 – 11.03.2023	Future collaborations in the field of epitaxy	USA
Dimitri Chafatinos	Centro Atómico Bariloche (CNEA)	02.05.2023 – 26.06.2023	Coherent GHz electro-optomechanics with polaromechanical crystals	Argentina
Alessandro Pitanti	Consiglio Nazionale delle Richerche (CNR)	06.03.2023 – 30.04.2024	Acoustic chirality and polarization in solid-state systems	Italy
Behraz Vatankhahghadam	University of Toronto	15.05.2023 – 14.08.2023	Development of GHz acoustic transducers and mapping of acoustic fields in semiconductor structures	Canada
John Freeland	Argonne National Laboratory	29.05.2023 – 14.06.2023	Design of a synchrotron-based experimental setup for simultaneous measurement of spectroscopic and structural properties during film growth	USA
Bharat Jalan	University of Minnesota	08.05.2023 – 10.05.2023	Navigating MBE Growth of Atomically Precise Complex Oxides using Source Chemistry	USA
Madeleine Msall	Bowdoin College	24.07.2023 – 14.07.2024	Optimization of the design of interdigital transducers for the excitation of high frequency surface-acoustic-waves	USA
Atelkete Kassa	Technische Universität Darmstadt	01.08.2023 – 22.12.2023	Correlation between structural and magneto-transport properties of 2D Fe ₅ GeTe ₂ ferromagnetic films	Germany
Yi Pan	Center for Spintronics and Quantum Systems	14.08.2023 – 15.09.2023	Atomic manipulation on III-V semiconductor surfaces.	China
Aidan Campbell	University of Strathclyde	15.09.2023 – 30.04.2024	Cathodoluminescence of InGaN in thick planar layers and top-down nanowire arrays	United Kingdom
Anna Sacchi	University of Parma	01.11.2023 – 20.12.2023	Growth and Characterization of Si-doped epsilon/kappa-Ga ₂ O ₃ single domain layers	Italy

Martynas Skapas	Centre for Physical Sciences and Technology (NFTMC)	06.11.2023 – 20.11.2023	In-situ TEM measurements of Ga(As,Bi) and Heussler alloy structure	Lithuania
Edgar Cerda Mendez	Universidad Autonoma de San Luis Potosi (UASLP)	21.11.2023 – 18.12.2023	Hybride Mikrokavitaten fur Exziton-Polaritonen	Mexico
Audrey Gilbert	Université de Montpellier-IES	20.11.2023 – 01.12.2023	Transmission Electron Microscopy investigations of defect structures formed during the direct epitaxy of III-V-semiconductors on Si(001)	France

Staff

Scientific staff: including Ph. D. students (D) and externally funded personnel (P)

Aggarwal, Neha (P)	Defect-engineering in graphene for tailored van der Waals epitaxy of hexagonal BN
Ardenghi, Andrea (D, P)	Point defects control in Ga ₂ O ₃ thin films grown via molecular beam epitaxy
Ashurbekov, Nazim (D, P)	Radio-frequency phonon resonators for coherent electron-phonon coupling
Biermann, Klaus	Molecular beam epitaxy of GaAs-based advanced heterostructures
Bierwagen, Oliver	Molecular beam epitaxy of oxides
Brandt, Oliver	Group-III nitrides and semiconductor nanowires
Campbell; Aidan (P)	Chemical and optical nanoscale analysis of (In,Ga)N layers and ordered nanowire arrays
Chen, Wenshan (D, P)	Growth and doping of (Si,Ge,Sn)O ₂ -based materials
da Silva, Alessandra	Electron tomography and microscopy of semiconducting nanomaterials
de Pedro Embid, Ismael (D, P)	Optical spectroscopy on microcavity polaritons modulated by acoustic phonons
Dinh, Duc Van (P)	Growth of (Sc,Al)N thin films
Doustipour, Farshad	Student assistant: Atomic force microscopy
Engel-Herbert, Roman	Director
Flissikowski, Timur	Ultrafast dynamics of semiconductor structures
Fölsch, Stefan	Low-temperature scanning tunneling microscopy and spectroscopy
Geelhaar, Lutz	Molecular beam epitaxy and semiconductor nanowires
Gómez Ruiz, Mikel (D)	Cathodoluminescence spectroscopy and correlated chemical and structural analysis of core/shell nanowires
Graser, Karl (D, P)	Transmission electron microscopy on dislocation reduction in III-V on Si heterostructures
Hanke, Michael	Synchrotron x-ray diffraction
Hansemann, Moritz	Synthesis of FeGe ₂ layers
Herfort, Jens	Ferromagnet-semiconductor heterostructures Chairman Works Council
Hernández Mínguez, Alberto	Manipulation of optical and electronic properties of low-dimensional structures using surface acoustic waves
Hoffmann, Georg (D)	Growth and doping of BaSnO ₃ and LaInO ₃
Hucho, Carsten	Technology and transfer
John, Philipp	Epitaxy and materials science of (Al,Sc)N nanowires
Jordão Lopes, João Marcelo	Epitaxy of two-dimensional materials
Kaganer, Vladimir	Theories of molecular-beam-epitaxial growth and x-ray scattering
Kang, Jingxuan (D, P)	Top-down synthesis and optical properties of ordered (In,Ga)N nanowire arrays
Kumar, Hitesh	Cryogenic scanning tunneling microscopy of two-dimensional semiconductors

Kuznetsov, Alexander (P)	Coherent electro-optomechanics at GHz frequencies with confined microcavity exciton-polaritons
Lähnemann, Jonas	Spatially resolved optical spectroscopy and structural as well as compositional analysis of nanostructures
Leite Gomes, João Pedro	Acoustically-driven magnonics
Loeto, Kagiso (P)	time-resolved cathodoluminescence spectroscopy on various semiconductor materials
Lü, Xiang	Terahertz quantum-cascade lasers
Ludwig, Stefan	Quantum transport in nanoelectronic systems
Luna Garcia de la Infanta, Esperanza	Transmission electron microscopy of heterointerfaces
Lv, Hua	Spin-transport phenomena in layered and two-dimensional magnetic materials
Marín Largo, Francisca (D, P)	Growth and luminescence analysis of bent GaAs nanowires
Meißner, Moritz	Student assistant: Quantum efficiencies of micro LEDs
Nordlander, Johanna	PHARAO – Design of novel functional and quantum materials using in-situ synchrotron x-ray diffraction
Paysen, Ekaterina (D)	Multi-scale electron tomography of interfaces
Pham, Van Dong (P)	Two-dimensional metal intercalation studied by low-temperature scanning tunneling microscopy
Pistore, Valentino	Micro- integrated terahertz quantum cascade laser for ultrahigh-resolution spectroscopic
Ramsteiner, Manfred	Electronic, vibrational, and magnetic properties of semiconductors
Reis, Anna (D, P)	In-situ x-ray scattering study of surface and interface dynamics at growing crystalline layers
Richter, Steffen	Student assistant: BALET
Saeedi, Meysam (D)	Optomechanical exciton-polariton metamaterials
Santos, Paulo	Acoustic, optic, and magnetic properties of nanostructures
Schrottke, Lutz	Quantum-cascade lasers and optical properties of heterostructures
Shoaei, Safa	Heterogeneous Semiconductor Physics Disordered semiconductors and hybrid systems? (MRW)
Sirt, Serkan (D, P)	Interplay between the quantum Hall and Aharonov-Bohm effects in mesoscopic circuits
Spallek, Domenik (D)	Cathodoluminescence of ultrawide bandgap semiconductors
Sun, Doyoung (D)	Optoelectronic characterization of printed organic solar cells
Tahraoui, Abbas	Comprehensive semiconductor technology
Takagaki, Yukihiro	Electric properties of nanometer-scale materials
Tokmoldin, Nurlan (P)	organic and hybrid solar cells, doping and photo-indexed charges; Optoelectronics of disordered semiconductors
Tornatzky, Hans	Raman spectroscopy of binary and complex oxides
Trampert, Achim	Microstructure and electron microscopy
Wagner, Markus	Semiconductor Spectroscopy
Yuan, Mingyun (P)	GHz acoustic control in semiconductor nanostructures
Zhang, Huaide	(In,Ga)N nano-epitaxy for amber LEDs

Non-Scientific Staff

Anders, Walid	Technology
Arnhold, Kerstin	Finances/Purchasing
Baumann, René	Workshop
Behnke, Steffen	Technician
Bluhm, Anne-Kathrin	Technician
Bruen, Eimear	Communications
Ehrensack, Kerstin	Technician
Ferber, Thomas	Workshop
Garcia Gomez, Sokrates	IT
Heinitz, Sebastian	Electrician
Herrmann, Claudia	Technician
Kosikowski, Philipp	Technician
Litschauer, Maximilian	Technician
Matzeck, Christopher	Technician
Matzeck, Margarita	Technician
Morgenroth, Katrin	Technician
Pfeiffer, Astrid	Technician
Pfeiffer, Jörg	Head of Workshop
Prüfer, Even	HR
Rauwerdink, Sander	Technology
Schönherr, Hans-Peter	Technician
Sieg, Michael	Workshop
Steffen, Doreen	Technician
Stemmler, Carsten (P)	Technician
Suchilina, Ekaterina	Office Assistant and Travel Management
Szegedy, Erika	Administrative Coordinator (Project)
Timm, Anne Susanne	Library
Venohr, Thomas	Workshop
Volkmer, Nicole (P)	Technology
Wendt, Christian	Head of IT
Wirsig, Arno	Technology
Wirt-Brunnckow, Andreas	IT
Worthmann, Glen	IT (internship)
Yildirim, Altug Haydar	Technology